

Warsaw University of Technology
Faculty of Physics

Doctoral thesis

Two-particle correlations in $p+p$ and $Pb+Pb$ collisions at SPS energies

Korelacje dwucząstkowe w zderzeniach $p+p$ oraz $Pb+Pb$ przy
energiach akceleratora SPS

Bartosz Maksiak

Supervisor: dr hab. Katarzyna Grebieszko

Warsaw, November, 2016

Contents

| | |
|--|-----------|
| Contents | i |
| 1 Introduction | 3 |
| 1.1 Standard Model | 3 |
| 1.2 Universe and its link to Quark-Gluon Plasma | 5 |
| 1.3 Phase diagram of strongly interacting matter | 7 |
| 1.4 Looking for Quark-Gluon Plasma | 8 |
| 1.4.1 Signatures of QGP | 8 |
| 1.4.2 Energy threshold for deconfinement | 12 |
| 1.5 Critical point of strongly interacting matter | 13 |
| 2 Correlations in azimuthal angle and pseudorapidity | 15 |
| 2.1 Definitions | 15 |
| 2.1.1 Azimuthal angle, rapidity and pseudorapidity | 15 |
| 2.1.2 $C(\Delta\eta, \Delta\phi)$ correlation function | 16 |
| 2.2 Past studies | 17 |
| 2.3 Recent studies | 19 |
| 2.3.1 RHIC experiments: STAR and PHOBOS | 20 |
| 2.3.2 LHC experiments: CMS, ATLAS, ALICE, and LHCb | 24 |
| 3 The NA61/SHINE experiment | 37 |
| 3.1 NA61/SHINE in CERN accelerator complex | 37 |
| 3.2 NA61/SHINE detector | 38 |
| 3.2.1 Beam detectors, trigger system, Time Projection Chambers, and Time of Flight walls | 38 |
| 3.2.2 Upgrades of NA61 | 41 |
| 3.3 Software, data calibration, and reconstruction | 41 |
| 3.4 Simulation chain | 42 |
| 4 Correlations in p+p energy scan | 45 |
| 4.1 Event and track selection | 45 |
| 4.1.1 2009 p+p data set | 45 |
| 4.1.2 Model simulations | 47 |
| 4.2 Results of inclusive analysis | 50 |
| 4.2.1 Uncorrected results | 52 |

| | | |
|----------|---|------------|
| 4.2.2 | Detector effects | 54 |
| 4.2.3 | Corrected results | 57 |
| 4.3 | Uncertainties | 60 |
| 4.3.1 | Statistical uncertainties | 60 |
| 4.3.2 | Systematic uncertainties | 64 |
| 4.4 | Comparison with models | 66 |
| 4.4.1 | EPOS and UrQMD | 66 |
| 4.4.2 | Flux-tube fragmentation model | 75 |
| 4.5 | Contribution of jets | 77 |
| 4.5.1 | Analysis with p_T restrictions | 77 |
| 4.5.2 | UrQMD pseudo-jet structure | 84 |
| 4.6 | Results of semi-inclusive analysis in multiplicity bins | 85 |
| 4.7 | Comparison with other experiments | 89 |
| 5 | Correlations in Pb+Pb collisions | 91 |
| 5.1 | Data sets and cuts | 91 |
| 5.2 | Correlation results | 92 |
| 5.2.1 | Comparison with p+p | 92 |
| 5.2.2 | Two-track resolution cut analysis | 94 |
| 6 | Summary | 107 |
| | Bibliography | 109 |
| A | Correlation measures | 117 |
| B | Particle Population Matrix | 123 |
| C | Examples of distribution shapes | 125 |

Abstract

In this thesis two-particle correlations in pseudorapidity and azimuthal angle in p+p collisions at beam momenta: 20, 31, 40, 80, and 158 GeV/c are presented. Data were recorded in the NA61/SHINE experiment at the CERN Super Proton Synchrotron (SPS). The results are compared to the EPOS and the UrQMD models as well as to the results from various experiments at the Relativistic Heavy-Ion Collider (RHIC) and the Large Hadron Collider (LHC). Dedicated comparison analysis was done also on NA49 data of Pb+Pb collisions.

The inclusive results in p+p show correlation structures connected with resonance decays, Bose-Einstein statistics, momentum conservation, and strings fragmentation. No structures connected with hard processes were observed even at 158 GeV/c beam momentum. The EPOS model reproduces data fine except of Bose-Einstein enhancement; the UrQMD model shows many disagreements with data.

The results provide an insight into forgotten realm of soft physics where jet peaks do not cast shadows onto two-particle correlations landscape.

In the first chapter a general look at the domain of heavy-ion physics is presented. The Standard Model is briefly discussed as well as Quark-Gluon Plasma with its signatures and location in the phase diagram of strongly interacting matter.

The second chapter brings an overview of particle correlations. Firstly, two-particle correlation function $C(\Delta\eta, \Delta\phi)$ is defined. Then, historical and recent analyses on two-particle correlations are presented. Many results from experiments at RHIC and LHC are shown together with discussion on correlation structures appearing in the plots.

In the third chapter, the NA61/SHINE experiment is introduced. Firstly, the detector setup is described as well as current and future upgrades. Then, the software part of the experiment is mentioned with its methods of calibration, reconstruction and data simulation.

The fourth chapter contains the main part of the analysis of proton-proton interactions. After description of event and track selections, the main results from the inclusive analysis are presented together with detector effects correction method. Calculation of statistical and estimation of systematic uncertainties is depicted. Then, data results are compared to the EPOS and the UrQMD models. Next, two sub-analyses of correlations (with no transverse momentum restrictions and semi-inclusive analysis in multiplicity bins) are presented. The chapter ends with a comparison with results from similar analyses in experiments at RHIC and LHC.

In the fifth chapter two-particle correlations in Pb+Pb interactions at 20A and 158A GeV/c are presented. They are compared to the results from p+p collisions. The analysis of $C(\Delta\eta, \Delta\phi)$ with changing two-track distance is performed.

The thesis is closed with a summary in the sixth chapter.

Streszczenie

W rozprawie prezentowane są wyniki z dwucząstkowych korelacji w pseudopośpieszności i kącie azymutalnym przy pędach wiązki 20, 31, 40, 80 i 158 GeV/c w zderzeniach proton-proton przy energiach akceleratora *Super Proton Synchrotron* (SPS) w CERN. Analizowane dane zostały zebrane przez eksperyment NA61/SHINE. Wyniki porównano do przewidywań modeli EPOS i UrQMD, do wyników innych eksperymentów przy akceleratorach *Relativistic Heavy-Ion Collider* (RHIC) i Wielkiego Zderzacza Hadronów (*Large Hadron Collider*, LHC), a także do rezultatów uzyskanych z dedykowanej analizy przeprowadzonej na danych ze zderzeń ołów-ołów z eksperymentu NA49.

Wyniki z analizy inkluzywnej przedstawiają struktury związane z rozpadami rezonansów, statystyką Bosego-Einsteina, zasadą zachowania pędu oraz fragmentacją strun. Nie wykryto żadnych struktur związanych z procesami twardej fizyki. Model EPOS odtwarza rzeczywiste dane dobrze z wyjątkiem braku korelacji związanych ze statystyką Bosego-Einsteina; model UrQMD wykazuje wiele rozbieżności względem danych.

Wyniki zaprezentowane w tej pracy rzucają światło na zapomnianą już krainę miękkiej fizyki, gdzie szczyty dżetów nie rzucają cienia na nizinę dwucząstkowych korelacji.

W pierwszym rozdziale przedstawiono ogólnie dziedzinę fizyki zderzeń ciężkich jonów. Pokróćce omówiono Model Standardowy oraz plazmę kwarkowo-gluonową wraz z jej sygnaturami i umiejscowieniem na diagramie fazowym silnie oddziałującej materii.

Drugi rozdział opisuje korelacje dwucząstkowe. Najpierw przytoczono definicję funkcji korelacyjnej $C(\Delta\eta, \Delta\phi)$, a następnie opisano bardziej szczegółowo zarówno starsze, jak i nowsze wyniki badań nad tą wielkością. Pokazano wiele wyników analiz z eksperymentów przy akceleratorach RHIC i LHC, a także przeprowadzono dyskusję nad strukturami korelacyjnymi, które pojawiły się na wykresach z tymi wynikami.

Trzeci rozdział opisuje eksperyment NA61/SHINE począwszy od części sprzętowej samego detektora i jego podsystemów, a skończywszy na oprogramowaniu wraz z metodami kalibracji, rekonstrukcji i symulacji danych.

Rozdział czwarty zawiera właściwe wyniki analiz danych ze zderzeń proton-proton. Po opisanu cięć na zderzenia oraz ślady przedstawiono wyniki inkluzywnych analiz wraz z metodą poprawiania wyników na efekty detektorowe. Następnie pokazano obliczenia niepewności statystycznych oraz oszacowania niepewności systematycznych. Później, wyniki otrzymane z danych porównano do wyników przewidywań teoretycznych z modeli EPOS i UrQMD. Dodatkowo, pokazano wyniki z dwóch podanaliz: korelacji bez ograniczenia na pęd poprzeczny oraz analizę w binach krotności. Rozdział zakończony jest porównaniem otrzymanych wyników z analiz inkluzywnych do wyników podobnych analiz otrzymanych w innych eksperymentach przy RHIC i LHC.

W rozdziale piątym przedstawiono analizę dwucząstkowych korelacji w zderzeniach ołów-ołów przy pędach wiązki 20 oraz 158 GeV/c na nukleon. Wyniki porównano z wynikami z analiz inkluzywnych w zderzeniach proton-proton. Wykonano także analizę funkcji korelacyjnej w zależności od cięcia na odległość między dwoma śladami.

Rozprawa zakończona jest podsumowaniem w rozdziale szóstym.

Acknowledgments

I would like to thank Katarzyna Grebieszko for her enormous patience and an urge to investigate each detail of my results. Thanks to her, the number of essential and linguistic errors was significantly reduced.

Many thanks go to people from the NA61/SHINE Collaboration. Mostly to Marek Gaździcki for being a chief of the experiment. He is always full of ideas and believes that every problem is solvable. Thanks to him, I was given an opportunity to do many very different things in NA61/SHINE.

I also thank Peter Seyboth for being the most kind and warm-hearted person in the experiment. We had many interesting conversations about beginnings of CERN as well as about older experiments and accelerators there. His huge experience in particle and nuclear physics was very helpful during development of my two-particle correlations studies.

I am grateful to the DCS Master – Tobiasz Czopowicz for all software discussions and advices as well as for excellent supervision of me as a DCS expert. Further thanks go to Maja Maćkowiak-Pawłowska for fruitful discussions that were fundamental for the studies of detector effects, to Emil Kaptur for help with EPOS and its insides, and to Szymon Puławski for a lot of discussions on various topics during work breaks and for a discussion concerning his analysis of inclusive mean transverse momenta. Many thanks also to Grzegorz Stefanek and Dag Larsen for a great mutual work on the data production of all collision systems recorded by NA61. Finally, I would like to thank the rest of the Collaboration for shaping my communication abilities and for the opportunity to talk with people from the entire world.

I am thankful and respectful to Cheuk-Yin Wong for spotting my results, referring to them in his flux-tube fragmentation model as well as for many great and fruitful e-mail discussions.

Last but not least, I would like to thank Mieszko Bańczerowski, Patrycja Szubstarska, Rafał Sarnecki, Marcin Kryński, and all the members of the Music and Acoustics Science Club (Koło Naukowe Muzyka i Akustyka – KNMiA) at the Faculty of Physics WUT who seeded in me a passion of creating and producing music, for learning what is friendship, and for making me waste a year of my PhD studies for these not-exactly-scientific activities.

Chapter 1

Introduction

Since the beginning of the human history we have been curious about everything that surrounds us. This curiosity brought us to all of discoveries and inventions and made our species to be the most developed one on the Earth. It has been driving us to understand why eating raw meat causes sickness and how to prevent it, why putting a hand into an open fire makes the skin burned and why water kills fire? Further, we started to ask ourselves why do we have days and nights, seasons, and sun eclipses? What are thunders? Why does amber rod rubbed with cat's fur attract certain light objects or why does a lodestone attract iron pieces? Why does an uranium salt blacken a photographic plate?

There were many people trying to answer these questions. By successfully describing single phenomena they have developed our state of knowledge about the world – discovered another fragments of the laws of the Nature. In time, these fragments were gathered and generalized to create theories which were then merged into bigger theories. This happened to theories of electricity and magnetism forces when they were unified by James Maxwell in 1873 in his *Treatise on Electricity and Magnetism*. On the other hand, with our scientific and technological development, we discovered that some theories are not applicable in a specific conditions, so they needed to be reformulated. This was the case with classical mechanics formulated by Isaac Newton's laws of motion in 1687 which was successfully used until 20th century when it revealed some flaws. They were covered by Einstein's General (1907-1915) and Special Relativity (1905) theories as well as quantum mechanics by many famous physicists like Heisenberg, Schrödinger, Born, Dirac, Bohr, Einstein. All these efforts lead the humankind to formulate a “theory of everything” that describes all phenomena we can observe – to give us a set of laws and formulas that, hypothetically, would make us able to create our own universe.

At the beginning of 21st century we stand with few general theories but each of them has some aspects that were not yet confirmed by the current state of science. However, the most accurate and successful is the Standard Model.

1.1 Standard Model

At the moment, the Physics knows six quarks and six leptons (with their twelve anti-particles), as well as four interactions mediated by gauge bosons: electromagnetic, strong, weak, and gravitational. The Standard Model encloses all these particles and three interac-

tions – strong, electromagnetic, and weak. The last two are in an unified form of electroweak interactions (unified by Glashow, Weinberg and Salam in 1970's) [1]. The interactions are carried by bosons. The elementary particles, as described by the Standard Model [2, 3, 4], can be divided into three groups:

1. **Quarks.** There are three generations of them:

- *up* (u) and *down* (d) – the first generation,
- *charm* (c) and *strange* (s) – the second generation,
- *top* (t) and *bottom* (b), also known as *true* and *beauty* – the third generation.

The matter in normal conditions consists of only *up* and *down* quarks. In higher generations the quarks are heavier. Their charges are fractional ($\frac{2}{3}e$ for u, c, t and $-\frac{1}{3}e$ for d, s, b) and, since they are fermions, they have half-integer spin, thus obey the rule of Pauli exclusion. Quarks interact strongly by gluon exchange. Each quark has its own color charge (red, blue or green) and has its own anti-quark (with according anti-color). Every particle, that can be observed, consists of such combination of quarks that its color mix is neutral (white). So far, there were no direct observations of a single quark – they can be observed only in pairs and triplets which form particles called *hadrons*. Hadrons consisting of quark and anti-quark $q\bar{q}$ are called *mesons* and hadrons consisting of three quarks are called *baryons*. In some particular conditions it is expected that quarks and gluons can move freely without hadronic boundaries (more details in Sec. 1.2).

2. **Leptons.** They can be divided by electric charge:

- charged: electron (e^-), muon (μ^-), tau (τ^-) and their anti-particles – positron (e^+), positive muon (μ^+), and positive tau (τ^+);
- chargeless: electron neutrino (ν_e), muon neutrino (ν_μ), tau neutrino (ν_τ) and their anti-particles – electron anti-neutrino ($\bar{\nu}_e$), muon anti-neutrino ($\bar{\nu}_\mu$), and tau anti-neutrino ($\bar{\nu}_\tau$).

Leptons do not carry color charge, thus they do not interact strongly. Additionally, chargeless leptons do not interact electromagnetically also.

3. **Gauge bosons.** Every interaction in the Standard Model is described as an exchange of bosons which are the interaction carriers. These are:

- Photons (γ) — the carriers of electromagnetic interactions. The force coming from these interactions is important at the atomic level but in comparison with the force of strong interactions it is much weaker.
- Bosons W^+ , W^- , and Z^0 carry weak interactions. Important at subatomic level since they have small interaction range.
- Gluons carry force of the strong interactions. This is the strongest force but it has a very limited range ($\sim 10^{-15}$ m).
- The Higgs boson — a boson that carries interaction of the Higgs field which grants the particles their masses.

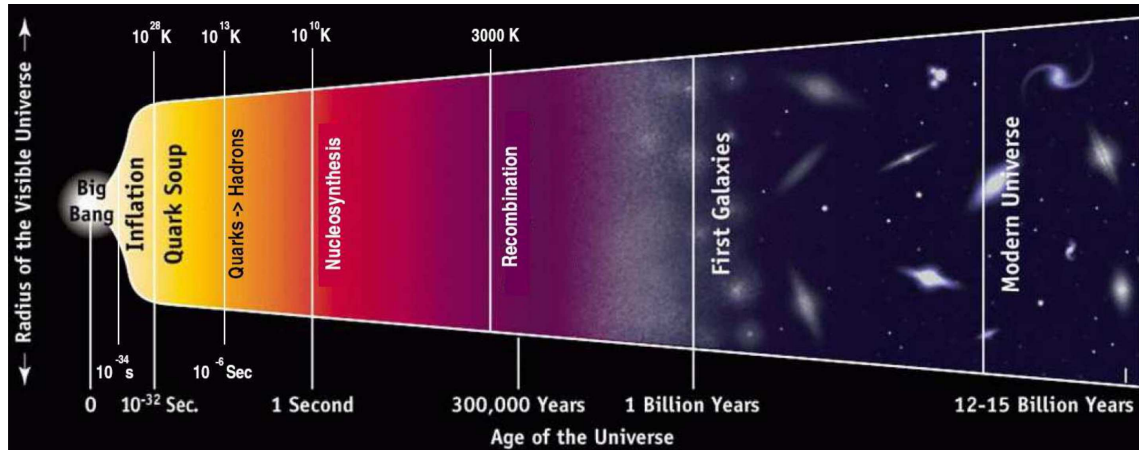


Figure 1.1: A probable evolution of the Universe. Picture taken from Ref. [5].

There is also a gravitational interaction (mediated by postulated graviton) – the weakest one but the most important in the astronomical scale. However, it is not included in the Standard Model. This is one of few flaws of this theory. The others are:

- It contains at least 19 free parameters (like particle masses) which should be taken from experimental data.
- It does not take into account neutrino masses — for the Standard Model neutrinos are massless (but there are some experimental proofs that they should have masses).
- No baryogenesis explanation — why nowadays there is such a huge imbalance between matter and anti-matter?

1.2 Universe and its link to Quark-Gluon Plasma

The ordinary hadronic matter, the current Universe is built from, is a result of an expansion. According to the Big Bang Theory, the Universe was created from an explosion of a very dense and hot object (*singularity*). Figure 1.1 shows the most probable scenario of the expansion of the Universe. It is believed that in the early stage of the Universe (order of few microseconds after the Big Bang) quarks and gluons formed the Quark-Gluon Plasma (QGP) – a state of strongly-interacting matter where quarks and gluons are free of their hadronic confinement. While expanding, the Universe became colder and reached the temperature and pressure allowing quarks to merge into hadrons (including protons and neutrons). Further cooling made hadrons to merge and form atoms and, finally, the Universe we know presently.

The Quark-Gluon Plasma is an important topic of studies these days. By creating and observing it, physicists want to take one step back to the early Universe and collect another argument for the Big Bang Theory.

It is expected that QGP can be created in sufficiently hot and dense systems [7, 8]. Such conditions allow quarks and gluons to move freely through the whole system. In our

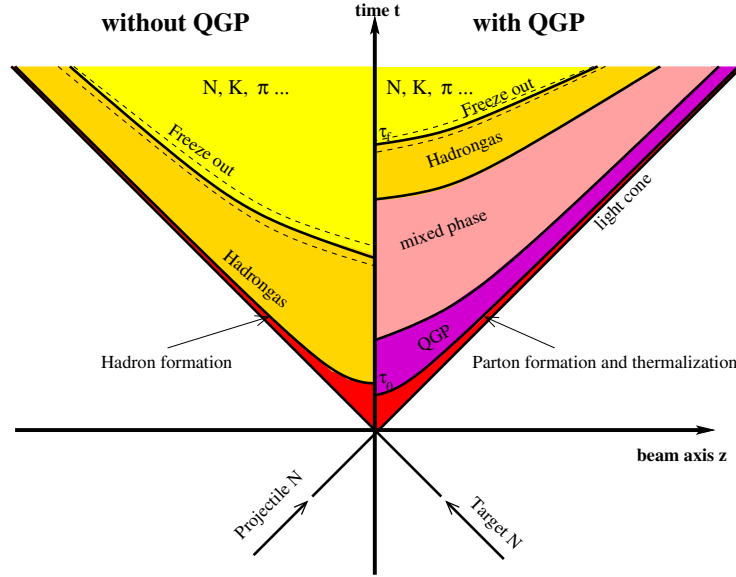


Figure 1.2: Space-time evolution of heavy-ion collision. Picture taken from Ref. [6].

world, QGP can be created only in laboratories by colliding heavy nuclei. Such collision squeezes and warms up the matter sufficiently to create QGP for a very short time.

Figure 1.2 shows two possible scenarios of space-time evolution of two heavy nucleus collisions: left side of the picture presents a scenario where the temperature and energy density are not sufficiently high to create Quark-Gluon Plasma after collision, right side of the picture shows a scenario with these conditions fulfilled. Let's consider the latter scenario on the example of central collision of two heavy ions (e.g. Au or Pb). In such a collision the number of nucleons colliding with themselves (*participants*) is about 400. During collision quarks from those nucleons have energies sufficient to deconfine from other quarks they were coupled within nucleons – the hadronic boundaries break and quarks, together with gluons, create a high-energy and dense volume called fireball. After the time¹ of $\tau_0 \approx 1 \text{ fm}/c$ (so-called *formation time*), due to high number of interactions, the system is thermalized and QGP is created.

The QGP state cools down and expands in an explosive way. During that time quarks and gluons start to merge and create hadrons. The process of such merging (changing from partonic to hadronic degrees of freedom) is called *hadronization*. The latest calculations based on lattice QCD claim that the hadronization takes place when the system has temperature² $T_c = (154 \pm 9) \text{ MeV}$ which corresponds to energy density $\epsilon_c \approx 340 \text{ MeV}/\text{fm}^3$ [9]. The time between QGP creation and hadronization is at the level of few fm/c. When hadronization stops, the system is in the state of *Hadron Gas* (HG) – there are no quarks moving freely; they are all confined with other quarks in hadrons. However, the hadrons have sufficient energy to still exchange their quarks with another hadrons. Due to further expansion of the system these interactions stop as well. A moment when hadrons stop exchanging quarks between each other (i.e. they settle their chemical composition) is called

¹This and the following numerical results are for Super Proton Synchrotron (SPS), unless stated otherwise.

²The calculations were done with an assumption of baryon chemical potential $\mu_B = 0$. Baryon chemical potential is defined in Sec. 1.3.

chemical freeze-out. After chemical freeze-out particles still interact and exchange their momenta. But it also stops in a moment called *kinetic freeze-out*. After the kinetic freeze-out particles do not collide with themselves and their momenta are fixed. The temperature of kinetic freeze-out is at the order of 90-140 MeV (from low-SPS to top-LHC energies).

Due to a very small time scale of the whole process from collision to kinetic freeze-out, only the particles after kinetic freeze-out can be observed in detectors. There are several laboratories with hardware capable of creating proper conditions for QGP creation. These are:

- Large Hadron Collider (LHC) located at CERN (The European Organization for Nuclear Research) near Geneva — so far the most powerful accelerator that will allow to collide lead ions with the energy³ 5.5 TeV per nucleon-pair and protons up to 14 TeV (currently, lead ions are collided with maximal energy 5.02 TeV per nucleon-pair and protons up to 13 TeV).
- Relativistic Heavy Ion Collider (RHIC) at BNL (Brookhaven National Laboratory), on Long Island with maximal gold ions collision energy of 200 GeV per nucleon-pair.
- Super Proton Synchrotron (SPS) at CERN — the last step of accelerating particles before injecting them to LHC (and the provider of protons, interactions of which were analyzed in this thesis) – allows to collide lead ions at the center-of-mass energy of 17.3 GeV and protons up to 29.1 GeV.
- Facility for Antiproton and Ion Research (FAIR) at GSI Helmholtz for Heavy Ion Research Darmstadt is under construction. Planned center-of-mass energies are up to approximately 7.5 GeV per nucleon pair [10].
- Nuclotron-based Ion Collider Facility (NICA) at JINR (The Joint Institute for Nuclear Research) near Dubna is also under construction. Center-of-mass energies for ions will be from 4 to 11 GeV per nucleon pair [11].

1.3 Phase diagram of strongly interacting matter

By changing the temperature and baryon chemical potential of strongly interacting matter (SIM) one can obtain its another state. The phase diagram of SIM is usually presented in $T - \mu_B$ plane. The μ_B variable is the *baryon chemical potential* which is the energy needed to add or remove one baryon from the system. In an ordinary nuclear matter the baryon chemical potential is approximately equal to the mass of the nucleon $\mu_B \approx m_N = 940$ MeV.

The phase diagram of strongly interacting matter is presented in Fig. 1.3. Its two main phases are Hadron Gas and Quark-Gluon Plasma. For lower values of temperature and baryon chemical potential the main phase is HG. With higher temperature the system is in a state of QGP. Lower temperatures and high values of μ_B exist in neutron stars (so-called *Cold QGP*).

Between QGP and HG states a boundary (phase transition) exists. The first-order phase transition is marked in Fig. 1.3 as the gray strip and it ends with a second-order phase transition (Critical Point, CP). Numerical calculations on 4-dimensional space-time

³This and further information about energy of the accelerators is given in the center-of-mass energy $\sqrt{s_{NN}}$ per nucleon pair.

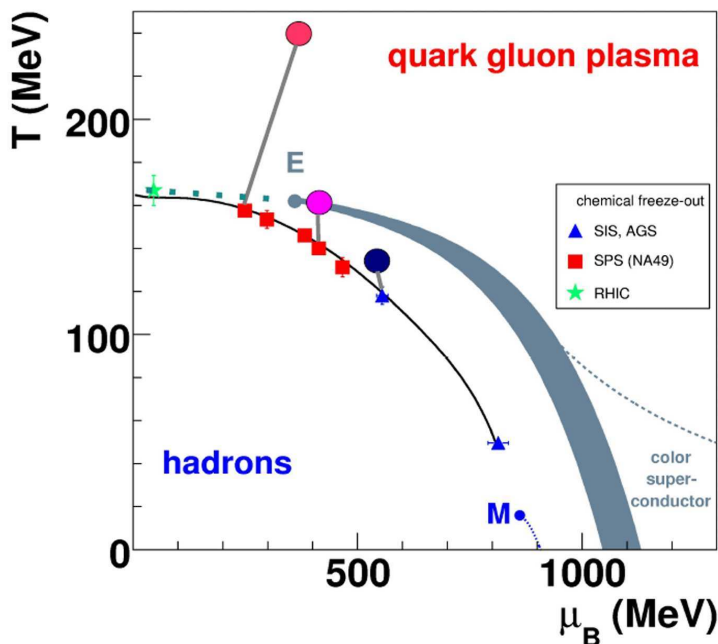


Figure 1.3: Phase diagram of strongly interacting matter. Points with error bars indicate positions of chemical freeze-out of the systems collided at various energies in various accelerators – RHIC, SPS, AGS (Alternating Gradient Synchrotron), SIS (Schwerionen-Synchrotron). Large circles represent hypothetical positions of the early stages. Picture taken from Ref. [12].

lattice, based on QCD, narrowed the region of CP existence to $T \approx 150 \div 170$ MeV and $\mu_B \approx 290 \div 440$ MeV [13, 14, 15]. Above this range of temperature and in direction of $\mu_B = 0$ the phase transition becomes cross-over (rapid but continuous evolution of the physical parameters of the system). However, it should be stressed that there are also predictions which conclude the absence of CP [16, 17].

The phase diagram of strongly interacting matter can be explored by colliding heavy-ions. In particular, by changing the energy of colliding ions as well as their size (number of nucleons).

1.4 Looking for Quark-Gluon Plasma

Proving the existence of QGP is the main goal of many experiments. The ways and tools for searching for QGP are described in this section.

1.4.1 Signatures of QGP

As mentioned earlier, a direct observation of QGP state is not possible. Conditions of such a state of matter, like extreme temperature or short life time, are immeasurable by the actual hardware. One can observe only particles that went through hadronization process. Nevertheless, by measuring produced particles, one can analyze some observables which are almost insensitive to hadronization process. Those observables are so-called signatures of QGP. The most popular of them are:

- **Strangeness enhancement** [18]. Production of strange quarks in QGP is energetically easier than in hadron gas. Moreover, strangeness can disappear only in weak decays. Because weak decay is a longer process than hadronization, strange hadrons can survive hadronization. Thus, strangeness enhancement is considered as one of the signatures of QGP. Such an effect was observed in SPS experiments [19, 20, 21]. The strangeness production yield, in comparison with the production of all non-strange particles, is higher in A+A interactions (where QGP can form) than in p+A or p+p collisions.
- **Charmonium suppression** [22]. Charm quark pairs ($c\bar{c}$), which can form charmonium states (e.g. J/ψ), are produced at the initial stage of the collision. In QGP, open color charges in medium can screen the color charge potential⁴ of c and \bar{c} quarks preventing them from binding to J/ψ . Thus, its production is suppressed when QGP state appears after collision. This effect was indeed observed at SPS, RHIC, and LHC experiments [23, 24, 25, 26].
- **Electromagnetic probes.** Photons do not interact strongly, therefore they can escape the collision region without distortions. Photons are produced during entire life of the fireball: prompt photons are produced in hard processes before the equilibrium (QGP) state, thermal photons are produced during QGP phase, mixed phase, and Hadron Gas phase as products of binding and/or scattering of quarks and gluons, and finally decay photons are products of electromagnetic decays of hadrons. The decay photons are the majority of all photons observed after the collision, therefore an observation of direct photons (prompt and thermal) is not a trivial problem. However, it can be done and after subtracting huge background signal coming from decay photons, one can eventually estimate the temperature of the early stage (QGP). The studies on direct photons emission were performed at SPS, RHIC, and LHC [27, 28, 29].
- **Jet quenching** [30]. Jet is a high-energy direction-correlated group of particles. It is also described as a spray of hadrons. It is a result of fragmentation of a parton⁵ escaping from collision region. Jets have high transverse momenta as the partons are produced in hard processes (with large momentum transfer). A specific type of jet is a di-jet, which is a pair of jets moving in opposite directions (see Fig. 1.4). If a di-jet is produced near the surface of QGP, one of jets (near-side) will be propagated normally, whereas the opposite one (away-side) will be smeared. The smearing is caused by a fact that the parton, that will fragment to produce the away-side jet, has to travel through hot and dense medium. Due to many interactions with quarks and gluons in QGP, the momentum of that parton will be lowered. Hence, the momenta of particles of the away-side jet, produced by fragmentation of that parton, will be lowered as well. Such a process is called jet quenching. This effect was firstly observed in Au+Au collisions at RHIC for example by studying distributions of two-particle correlations in azimuthal angle⁶ [31] and is shown in Fig. 1.4. The results shown that for central

⁴The mechanism is called Debye screening.

⁵It is quite contrainuitive name since partons (quarks and gluons) are the basic objects that build the matter, so strictly speaking, they cannot fragment.

⁶The study of two-particle correlations in azimuthal angle was performed by calculating the difference in azimuthal angles between trigger particle with $4 < p_T < 6$ GeV/c and associated particles (with smaller transverse momenta but still with $p_T > 2$ GeV/c). Transverse momentum is defined as $p_T = \sqrt{p_x^2 + p_y^2}$.

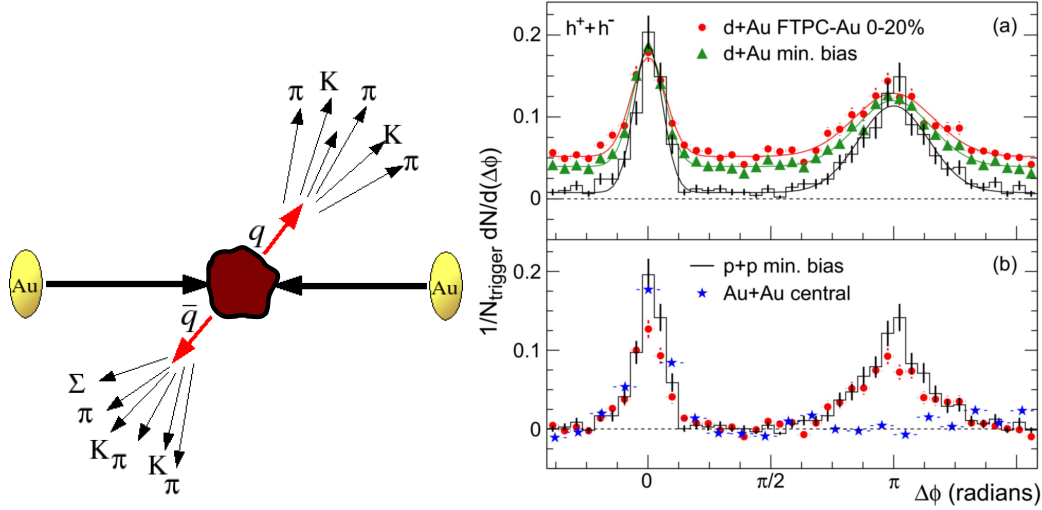


Figure 1.4: Left panel: Di-jet creation scheme. Right panel: Azimuthal angle difference ($\Delta\phi$) between trigger particle and associated particles. STAR results from d+Au, p+p, and central Au+Au collisions at top RHIC energy [31].

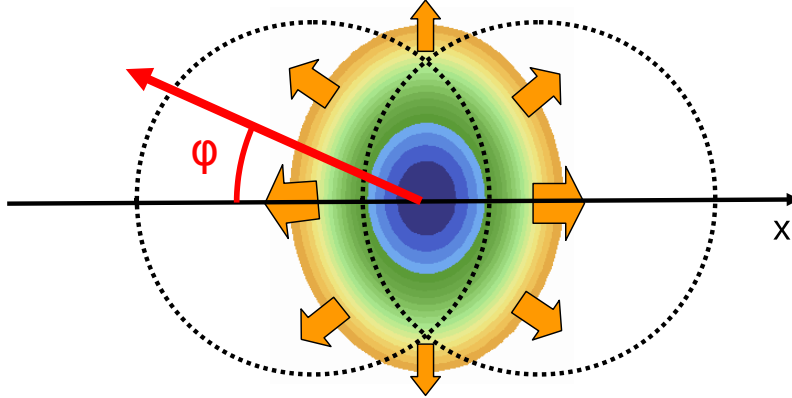


Figure 1.5: A graphical example of an almond-shape created in non-central heavy-ion collision. The x -axis in laboratory (LAB) system lays on the reaction plane (Φ_R). The reaction plane here is parallel to the beam axis orientated in such a way that the vector connecting centers of colliding ions defines the direction of the x -axis. The size of the arrows symbolizes flow magnitude. Picture created by F. Retiere.

Au+Au collisions the contribution of away-side ($\Delta\phi \approx \pi$)⁷ jet disappeared while it was still visible for p+p and d+Au collisions. Those results were interpreted as an existence of high-density medium.

- **Collective flow.** After heavy-ion collision, nucleons from collided ions form a system of high energy density which thermalize to create QGP (see Fig. 1.2). During QGP phase many interactions between deconfined quarks and gluons occur. Due to expansion, the system is cooling down and reaches chemical freeze-out and then kinematic freeze-out.

The magnitude and type of flow depend on the energy of the colliding system and its size. Apart from the type of colliding ions, the size depends on the impact parameter

⁷ $\Delta\phi$ is the difference in azimuthal angle between two particles: $\Delta\phi = |\phi_1 - \phi_2|$, where $\phi = \arctan(p_y/p_x)$. More details in Sec. 2.1.1.

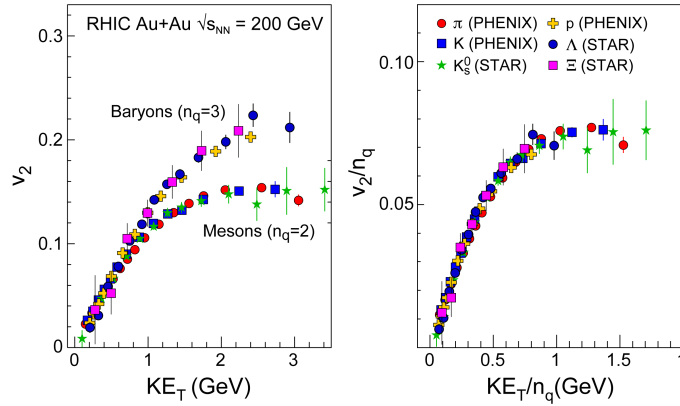


Figure 1.6: A comparison of v_2 magnitudes for data from Au+Au collisions at top RHIC energy. Left panel: v_2 versus transverse kinetic energy of mesons and baryons. Right panel: v_2 scaled by the number of constituent quarks. KE_T is the mean transverse kinetic energy⁸. Figure taken from Ref. [32].

of the collision (b). The parameter b is defined as the distance between centers of colliding ions in the collision plane. Low values of impact parameters mean (almost) central collisions. The more central collision was, the more azimuthally symmetric system is produced as well as the flow. Symmetric flow is called *radial flow*. When going to higher b parameter values the collision system shape starts looking like an almond and this results in *anisotropic flow*. The physical meaning of anisotropic flow is explained as the transformation of initial spatial anisotropy into final anisotropy in momentum space. In Fig. 1.5 an example of system created in non-central collision is presented. The initial (before thermalization) spatial anisotropy is transformed via rescatterings to pressure gradients. The pressure gradients are higher towards x -axis than towards the perpendicular axis, therefore more particles and with higher velocities (so with higher momenta) are produced in x direction. As a result, the momentum distribution of particles after non-central heavy-ion collision is azimuthally asymmetric. This type of flow is called an *elliptic flow*.

The patterns of anisotropic flow are analyzed in terms of Fourier expansion:

$$E \frac{d^3N}{dp^3} = \frac{1}{2\pi} \frac{d^2N}{p_T dp_T dy} (2\nu_1 \cos(\phi - \Phi_R) + 2\nu_2 \cos(2\phi - \Phi_R) + \dots), \quad (1.1)$$

where $p = \sqrt{p_x^2 + p_y^2 + p_z^2}$ is the total momentum, y is the rapidity (details in Sec. 2.1.1), and Φ_R is the reaction plane angle defined as an angle between the x -axis of the LAB coordinate system and the reaction plane. Fourier coefficients ν_n of Eq. 1.1 are subsequent anisotropic flow orders: ν_1 is *directed flow*, ν_2 – *elliptic flow* mentioned above, ν_3 is *triangular flow*, etc.

It is worth to mention here about ν_2 scaling with the number of constituent quarks. Studies were performed to check if the observed collective flow is in fact a flow of mesons and baryons or is inherited from the flow of partons [32]. The results are presented in Fig. 1.6. On the left panel the difference between elliptic flow magnitude for mesons and baryons is clearly seen and the results fall on one of two trends

⁸ $KE_T = m_T - m = \sqrt{m^2 + p_T^2} - m$, where m is a mass of a given particle.

depending of how many quarks the particle contains. Such a difference disappears (both trends overlap) when v_2 is scaled by the number of constituent quarks giving the v_2/n_q variable. The results of such a scaling are presented on right panel of Fig. 1.6. It was concluded that at the early stage the matter “flows” at the level of quarks and gluons and this scaling is treated as an evidence of so-called partonic collectivity at RHIC.

1.4.2 Energy threshold for deconfinement

Apart from looking for Quark-Gluon Plasma signatures, one can try to determine at which collision energy QGP can be created and at which energy cannot. The Statistical Model of the Early Stage (SMES) [33] suggests that the energy threshold for deconfinement (an energy region overlapping phase transition between QGP and HG; the minimal energy needed to create partonic system) is located between the top AGS beam energy ($11.7A$ GeV⁹) and the top SPS energy ($158A$ GeV). The energy, above which QGP forms, is to be approximately $30A$ GeV ($\sqrt{s_{NN}} \approx 7$ GeV). The big red circle to the right from the “E” point in Fig. 1.3 shows the situation when the early stage (circle) hits the transition line. The corresponding collision energy ($\sqrt{s_{NN}}$) is therefore called *onset of deconfinement energy*.

The main assumptions of the SMES model are:

- The first-order phase transition in the whole μ_B region (no critical point and no cross-over transition between phases). This assumption is due to use of “bag model” in the SMES.
- Quarks and gluons are in equilibrium at the early stage.
- There are three phases: confinement, mixed phase, and deconfinement. The temperature of the mixed phase is $T_c = 200$ MeV.
- The number of degrees of freedom g increases after QGP creation because the activation of partonic degrees of freedom.
- The entropy in the final state is proportional to the number of produced pions (entropy is carried mainly by pions in high energy heavy-ion collisions).
- The total number of strange quarks and total entropy are the same before and after hadronization.

The last assumption leads to the conclusion that the particle production analysis can give information about the early stage of the collision. As a result, the SMES model predicts the particle production yields.

The predictions of the SMES model are some structures of hadron production properties. The three most popular of them are the “kink”, the “horn”, and the “step”. The structures are related to the change of the number of degrees of freedom during transition between Hadron Gas and QGP. They can be seen in the dependencies on the energy in the center-of-mass or Fermi energy:

$$F \equiv \left[\frac{(\sqrt{s_{NN}} - 2m_N)^3}{\sqrt{s_{NN}}} \right]^{1/4} \approx \sqrt{\sqrt{s_{NN}}}, \quad (1.2)$$

⁹The symbol A after the value of energy means “per nucleon”.

where $\sqrt{s_{NN}}$ is the center-of-mass energy per nucleon pair and m_N is the mass of nucleon.

The “kink” structure can appear in the Fermi energy dependence of the ratio of total entropy (related to multiplicity of pions) to the number of wounded nucleons (nucleons which participated in at least one inelastic collision). The ratio increases linearly with F and is proportional to $g^{1/4}$ (g , as defined before, is the number of degrees of freedom). In hadron gas g is smaller than in QGP. As a result, in the region of the phase transition the slope changes (see Fig. 1.7, upper left) and is steeper in the QGP phase. This concerns only A+A collisions; p+p data does not change its slope.

The “horn” structure (see Fig. 1.7, upper right) is expected to appear in strangeness to entropy ratio with a sharp maximum for the region of phase transition. The ratio should rise with increasing Fermi energy in the hadron gas phase, then reaches the maximum at the beginning of the mixed phase. In the mixed phase, with increasing QGP contribution, the ratio decreases, and it is almost independent of energy in the QGP phase.

The “step” structure (see Fig. 1.7, lower panel) was expected in the dependence of temperature on the Fermi energy. A *plateau* is expected in the region of the mixed phase. This behavior is analogical to the one of water. The temperature rises with energy in pure hadron gas and QGP phases and is independent of it in the mixed phase. Here, the inverse slope parameter (T) of transverse mass spectra¹⁰ of produced hadrons is used instead of early stage temperature. Transverse mass spectra follow the formula:

$$\frac{dn}{m_T dm_T} = C \exp\left(\frac{-m_T}{T}\right) \quad (1.3)$$

The NA49 [36] experiment was testing the predictions of the SMES model in Pb+Pb energy scan from 20A GeV up to 158A GeV. The tests successfully confirmed [37, 38] the model predictions – all three structures have been observed in NA49. Recently, the NA61/SHINE experiment surprisingly showed that the rapid changes are also seen in p+p interactions (see Fig. 1.7).

1.5 Critical point of strongly interacting matter

In contrary to the SMES model, there are other predictions that, in the phase diagram of strongly interacting matter, the first-order phase transition ends with a second-order phase transition – the critical point (“E” in Fig. 1.3, see Sec. 1.3 for details). The critical point (CP) can be possibly seen in fluctuations analyses. The CP signal is expected at energies higher than the energy of the onset of deconfinement, because, in order to observe CP, the system has to freeze out near CP.

Theoretical predictions of multiplicity and transverse momentum fluctuations, which are increasing near the critical point, were done for example in Ref. [39] and the possible signal was then studied experimentally in NA49 [40, 41, 42, 43, 44, 45] as well as in NA61/SHINE [46, 47, 34].

¹⁰Transverse mass is defined as $m_T = \sqrt{m^2 + p_T^2}$.

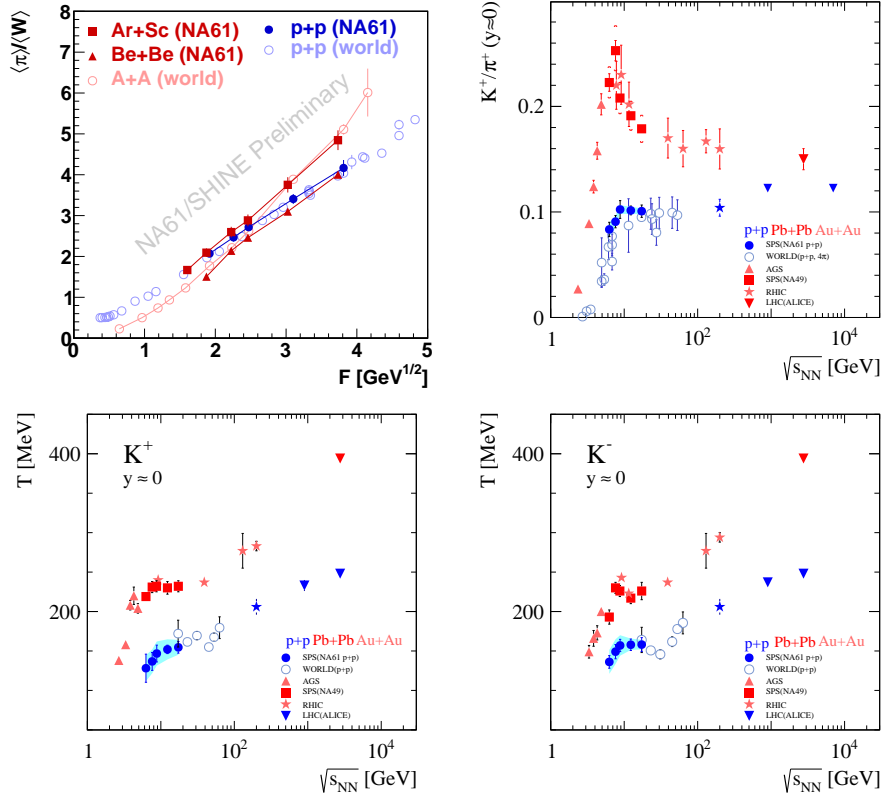


Figure 1.7: Top left: the “kink” structure – the dependence of the total pion multiplicity per wounded nucleon versus Fermi energy (definition in the text). Top right: the “horn” structure – energy dependence of K^+/π^+ ratio at mid-rapidity for central Pb+Pb and Au+Au collisions (red symbols) compared to results from p+p collisions (blue symbols). Bottom panels: the “step” structures – energy dependencies of the inverse slope parameter T of the transverse mass spectra of K^+ mesons (bottom left) and K^- mesons (bottom right). Pictures taken from [34, 35].

Chapter 2

Correlations in azimuthal angle and pseudorapidity

2.1 Definitions

2.1.1 Azimuthal angle, rapidity and pseudorapidity

Azimuthal angle is defined as the angle of particle production in the $x - y$ plane (see Fig. 2.1):

$$\phi = \arctan\left(\frac{p_y}{p_x}\right). \quad (2.1)$$

Rapidity y is a relativistic equivalent of velocity.

$$y = \frac{1}{2} \ln\left(\frac{E + p_L}{E - p_L}\right), \quad (2.2)$$

where $p_L = p_z$ is the momentum of the particle measured along the beam axis and $E = \sqrt{m^2 + p^2}$ is the total energy of the particle. The particles produced with longitudinal momentum higher than transverse momentum have higher values of rapidity, whereas particles produced with higher transverse momentum than longitudinal one have rapidity closer to 0.

To be calculated, rapidity variable needs mass of a particle. However, particle identification in many experiments is difficult. Thus, another quantity is often used – pseudorapidity η :

$$\eta = -\ln\left(\tan\left(\frac{\theta}{2}\right)\right), \quad (2.3)$$

where $\theta = \arctan\left(\frac{p_T}{p_L}\right)$ is the polar angle of a produced particle (see Fig. 2.1). The pseudorapidity does not need information about mass, but only about production angle of a particle. The pseudorapidity formula 2.3 can be rewritten in terms of momenta as:

$$\eta = \frac{1}{2} \ln\left(\frac{p + p_L}{p - p_L}\right). \quad (2.4)$$

Assuming that the particle is relativistic ($p \gg m$), the formula 2.4 can be approximated to the formula of the rapidity 2.2.

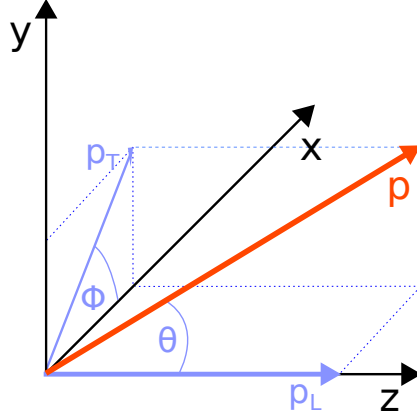


Figure 2.1: The azimuthal (ϕ) and polar (θ) angles definitions. p is the vector of total momentum.

2.1.2 $C(\Delta\eta, \Delta\phi)$ correlation function

Correlations are calculated as a function of the difference in the pseudorapidity (η) and azimuthal angle (ϕ) between two particles in the same event.

$$\Delta\eta = |\eta_1 - \eta_2|; \quad \Delta\phi = |\phi_1 - \phi_2|. \quad (2.5)$$

The correlation function C is calculated as following:

$$C(\Delta\eta, \Delta\phi) = \frac{N_{\text{background}}^{\text{pairs}}}{N_{\text{signal}}^{\text{pairs}}} \frac{S(\Delta\eta, \Delta\phi)}{B(\Delta\eta, \Delta\phi)}, \quad (2.6)$$

where $S(\Delta\eta, \Delta\phi) = \frac{d^2 N^{\text{signal}}}{d\Delta\eta d\Delta\phi}$ is the distribution of the signal which contains background also. The background needs to be removed from the signal. Hence, $S(\Delta\eta, \Delta\phi)$ is divided by an uncorrelated background $B(\Delta\eta, \Delta\phi) = \frac{d^2 N^{\text{background}}}{d\Delta\eta d\Delta\phi}$. Both distributions are normalized to the number of pairs: $N_{\text{pairs}}^{\text{signal}}$ and $N_{\text{pairs}}^{\text{background}}$.

The background distribution $B(\Delta\eta, \Delta\phi)$ is constructed by mixing events. The mixing algorithm reproduces event multiplicities, but particles in mixed events cannot originate from the same original event, i.e. there are no two particles from the same original event inside a mixed event. The example plots of $S(\Delta\eta, \Delta\phi)$ and $B(\Delta\eta, \Delta\phi)$ are shown in Appendix C.

Correlations in azimuthal angle and pseudorapidity were studied extensively in the experiments at LHC and RHIC in order to disentangle different sources of hadron correlations, such as:

- jets,
- collective flow,
- resonance decays,
- quantum statistics effects,
- Coulomb effects,

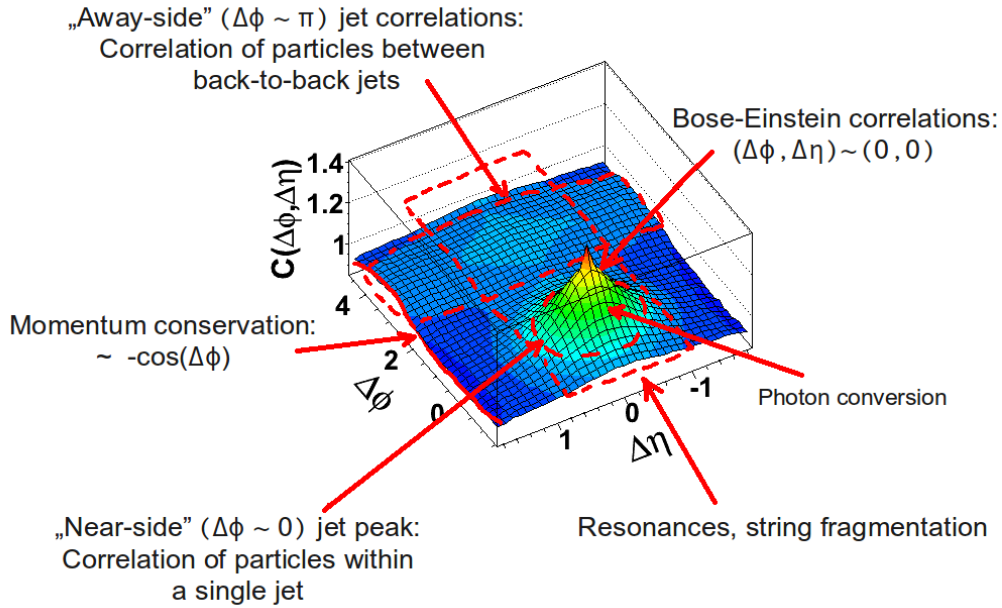


Figure 2.2: Sources of correlations on the example of ALICE 7 TeV p+p data. Figure taken from Ref. [48].

- conservation laws.

An example of the correlations landscape is shown in Fig. 2.2.

The next two sections describe historical background of the studies and show results with explanations of appearing structures, as well as their physical sources.

2.2 Past studies

First studies on correlations in rapidity

The first correlation studies began at early 70's as an attempt to understand the nature of strong interactions. Kenneth G. Wilson proposed [49] to study the correlation length – the maximal separation in rapidity, above which the particle production is independent. The first analyses of rapidity correlations in $K^+ + p$ interactions [50] discovered the strong correlations between negatively charged pions at small rapidity differences (short-range correlations). Shortly after, several other experiments put their interest onto this part of studies. In next years, first results on inclusive two-particle correlations were published by Argonne National Laboratory (ANL) and National Accelerator Laboratory (NAL) [51, 52], Fermilab [53] (all from United States) and by the Intersecting Storage Rings (ISR) experiments [54, 55] at CERN. All the results from aforementioned experiments showed an enhancement (a positive correlation) for produced particles at small rapidity differences.

Moreover, ANL/NAL experiment with 30-inch bubble chamber showed first results for charge-dependent¹ correlations. The results in p+p interactions at beam momenta 102 GeV/c [52] and 205 GeV/c [51] showed that the correlations for pairs of pions with opposite charges are stronger than correlations of same-charged pions. The ANL/NAL

¹All results so far were independent of charge combination of two particles in a pair.

published also results of semi-inclusive correlation analysis (for several final-state multiplicity bins) [53] in $\pi^+ + p$ and $p+p$ interactions. There were no correlations between negative pions observed for fixed pion multiplicity. Additionally, the inclusive analysis showed agreement with other results (i.e. strong correlations at $\Delta y \approx 0$). At the other side of the Atlantic Ocean, ISR published results [55] from inclusive two-particle correlations in reaction $p + p \rightarrow \gamma + \text{charged} + \dots$ at several energies ($\sqrt{s_{NN}} = 23, 30.5, 45, \text{ and } 53 \text{ GeV}$). Charged particles were considered to be pions while γ -rays were assumed to be produced entirely in π^0 decays. Here, a weak enhancement of short-range correlations of charged particles was observed.

Early theoretical predictions

After the first bunch of experimental results, physicists started to build models that would describe the data. The most successful theoretical predictions of observed correlations in rapidity and pseudorapidity were described by the two-component model [56, 57] developed later into the independent cluster emission model (ICM) [58]. The model assumes creation of clusters before the formation of final-state hadrons. These clusters are emitted independently and decay isotropically in their own rest frame into final-state hadrons. Data results can be parametrized by the ICM model in terms of the cluster multiplicity (also called “size” – the average number of particles in one cluster) and the decay “width” (the separation of particles in pseudorapidity).

Merging (pseudo)rapidity with azimuthal angle

The first and very detailed study on two-particle correlations in pseudorapidity and azimuthal angle (for the first time two-dimensional) of charged particles produced in $p+p$ interactions at $\sqrt{s} = 23$ and 53 GeV was published by the ACM Collaboration² [59]. They showed a complex structure with short-range correlations in pseudorapidity at about $\Delta\eta = 0$ (see Fig. 2.3, top panel). It was observed that correlations towards $\Delta\phi \approx \pi$ are stronger than towards $\Delta\phi \approx 0$ ³. ISR could not identify particles, thus pseudorapidity variable was used. Polar angles were measured in the laboratory frame and transformed to the c.m.s. frame with zero-mass assumption. A simple model was also used to theoretically describe the results: namely, the correlations were described by resonance decays: $\eta \rightarrow \pi^+ + \pi^- + \pi^0$, $\omega \rightarrow \pi^+ + \pi^- + \pi^0$ and $\rho^0 \rightarrow \pi^+ + \pi^-$. The results of the predictions are shown in bottom panel in Fig. 2.3. It was concluded that pseudorapidity correlations towards $\Delta\phi = \pi$ are induced by ρ meson (two-body) decays while η and ω meson (three-body) decays produce correlations over the full $\Delta\phi$ range. The main conclusion was that all correlations can be connected and reproduced qualitatively by combining production of η , ω , and ρ mesons.

The ACM Collaboration results were followed by the AFIMM Collaboration⁴. They presented results of two-particle correlations in $p+p$ and $\pi^- + p$ interactions at beam momenta 100-300 GeV/c in Fermilab’s 30-inch bubble chamber [60]. Since the AFIMM detector was able to identify particles, the rapidity variable, instead of pseudorapidity, was used in calculations. An innovation, comparing to previous results, was splitting the data into charge combinations: CC (charged-charged), ++, --, and +-. All negatively

²ACM stands for: Aachen-CERN-Munich.

³From now on, correlations in the region $\Delta\phi \approx 0$ will be referred as “near-side” while correlations in the region $\Delta\phi \approx \pi$ as “away-side”.

⁴AFIMM stands for: Argonne National Laboratory, Fermi National Accelerator Laboratory, Iowa State University and Ames Laboratory, Michigan State University, University of Maryland.

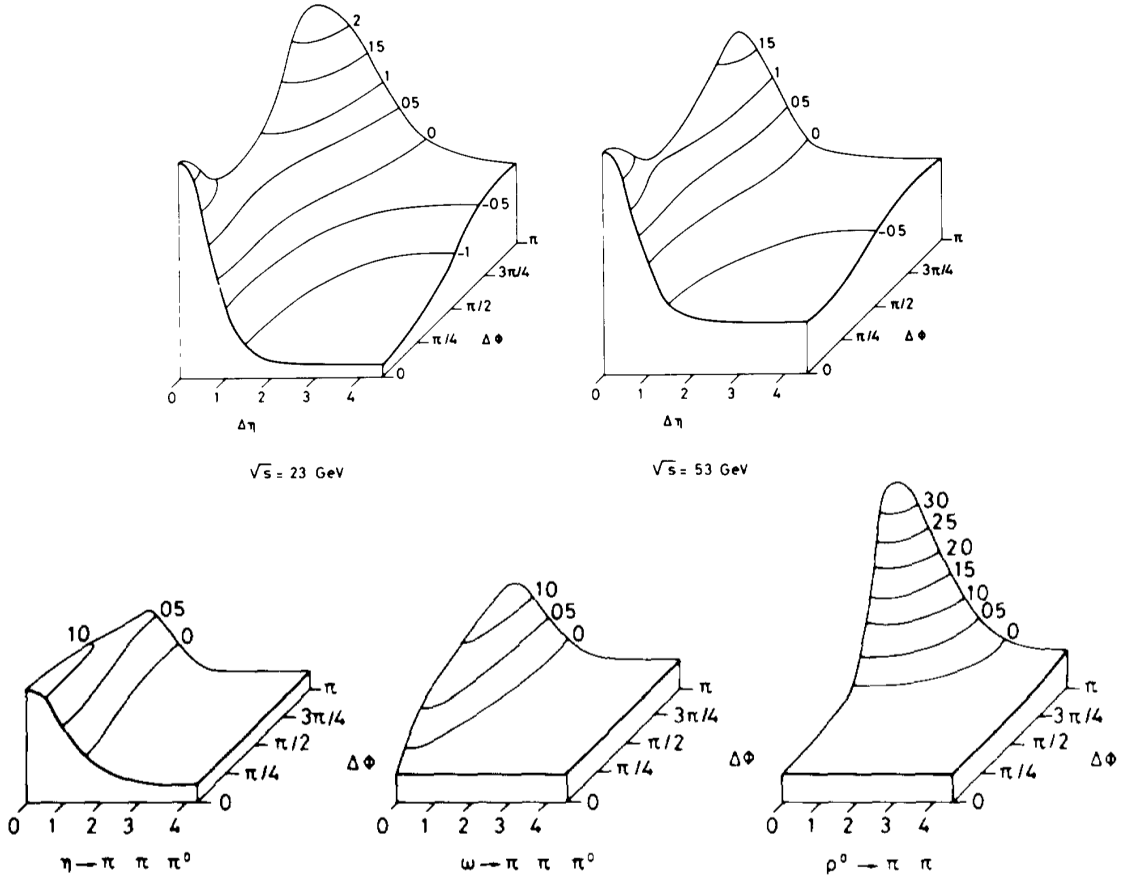


Figure 2.3: Top panel: Measured correlation functions $C^{II}(\Delta\eta, \Delta\phi)$ (see Appendix A for definition) of charged particles in p+p interactions at $\sqrt{s_{NN}} = 23$ and 53 GeV. Bottom panel: Calculated correlation functions for decays of mesons: $\rho^0 \rightarrow \pi^+\pi^-$, η and $\omega \rightarrow \pi^+\pi^-\pi^0$. Plots taken from Ref. [59].

charged particles were assumed to be π^- while all positively charged particles, which were not identified as protons using their ionization energy loss, were considered as π^+ . The analysis was performed in multiplicity bins, thus correlations $\langle J_n \cdot C_n(\Delta y, \Delta\phi) \rangle$ were calculated by combining all multiplicity ranges with J_n being a weight of a given C_n in a given multiplicity bin (see Ref. [60] or Appendix A for details). It was shown (see Fig. 2.4) that for like-sign charge particles the most visible structure was a strong correlation at $\Delta y \approx 0$ and $\Delta\phi \approx 0$ and for unlike-sign charged at small Δy and $\Delta\phi \approx \pi$. The correlations for CC pairs qualitatively agreed with ISR's results [59] and proved that the complex structure observed at ISR is a result of combination of structures for like- and unlike-sign charged particles. The authors of Ref. [60] suggested also that the near-side correlations include the effects of Bose-Einstein statistics.

2.3 Recent studies

The studies on $\Delta\eta\Delta\phi$ two-particle correlations became popular recently when the experiments at RHIC and LHC started taking data. This section presents an overview of $\Delta\eta\Delta\phi$ correlation studies in several experiments which published results in last fifteen years.

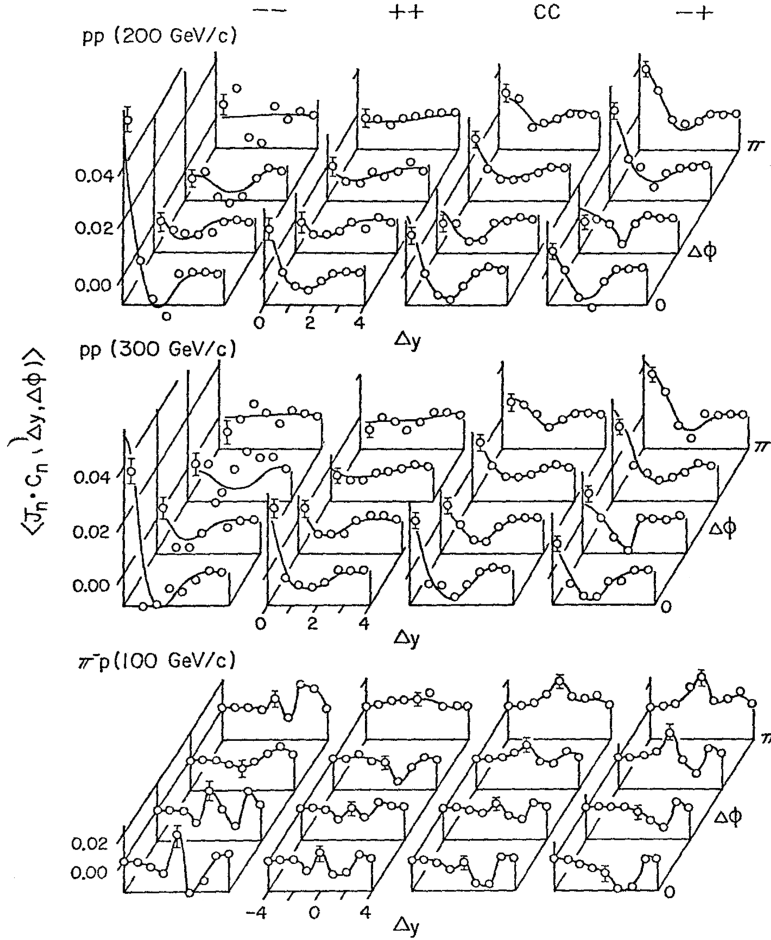


Figure 2.4: $\langle J_n \cdot C_n(\Delta y, \Delta\phi) \rangle$ versus Δy and $\Delta\phi$ (see Appendix A for details) correlation function (combined over multiplicity bins) for charged particles in p+p and π^-+p interactions at beam momenta: 100, 200, and 300 GeV/c. The results are presented in four charge combinations: both particles negatively charged (—), both particles positively charged (++), both particles charged without restriction on the charge (CC), and unlike-sign charged (-+). Four $\Delta\phi$ regions ($0 < \Delta\phi < \pi/4$, etc.) are plotted for each charge combination. Figure taken from Ref. [60].

2.3.1 RHIC experiments: STAR and PHOBOS

The STAR experiment started its correlations analyses from the studies of p+p interactions at $\sqrt{s_{NN}} = 200$ GeV [61]. The analysis was divided into correlations from the soft component and the hard component. The soft component in like-sign pairs (Fig. 2.5, most right) shows a gaussian peak at $(\eta_\Delta, \phi_\Delta) \equiv (\Delta\phi, \Delta\eta) = (0, 0)$. This enhancement was explained by a contribution of **Bose-Einstein** (HBT) correlations. Such peak is not present in unlike-sign soft component (Fig. 2.5, second from the left). Instead, a high and narrow peak was observed in unlike-sign correlations being a result of the photon conversion into e^-e^+ pairs. Another structure observed in unlike-sign soft component was a one-dimensional gaussian structure around $\eta_\Delta \approx 0$ which is a result of local charge conservation of longitudinally **fragmented strings**. The one-dimensional gaussian structure is suppressed at near-side ($\phi_\Delta \approx 0$) due to charge conservation constraining the correlations in low-multiplicity events. Such a suppression was not observed in high multiplicity collisions.

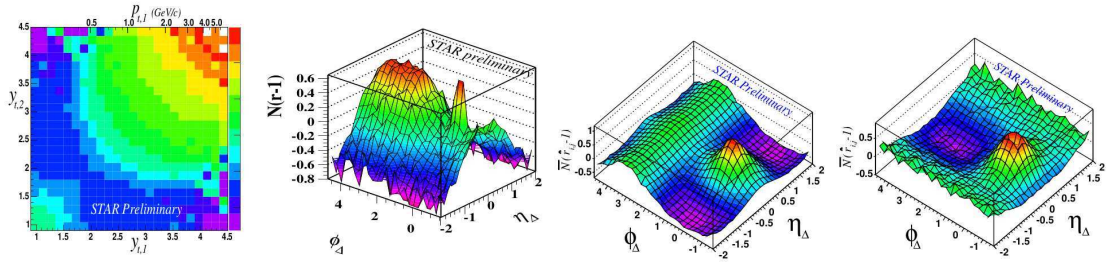


Figure 2.5: STAR results for p+p at 200 GeV. Most left: Distribution of transverse rapidity space y_t^6 . One can notice two regions with higher (warmer than blue) values which contribute to soft component ($y_t < 2$ corresponding to $p_t < 0.5$ GeV/c) and hard component ($y_t > 2$ corresponding to $0.5 > p_t > 6$ GeV/c). Second from left: Two-particle correlations in soft component for the unlike-sign charged pairs. Second from right: charge-independent (all charged pairs) correlations for the hard component. Most right: correlations in like-sign soft component. See Appendix A for precise definition of vertical scale in the plots. Figure taken from Ref. [61].

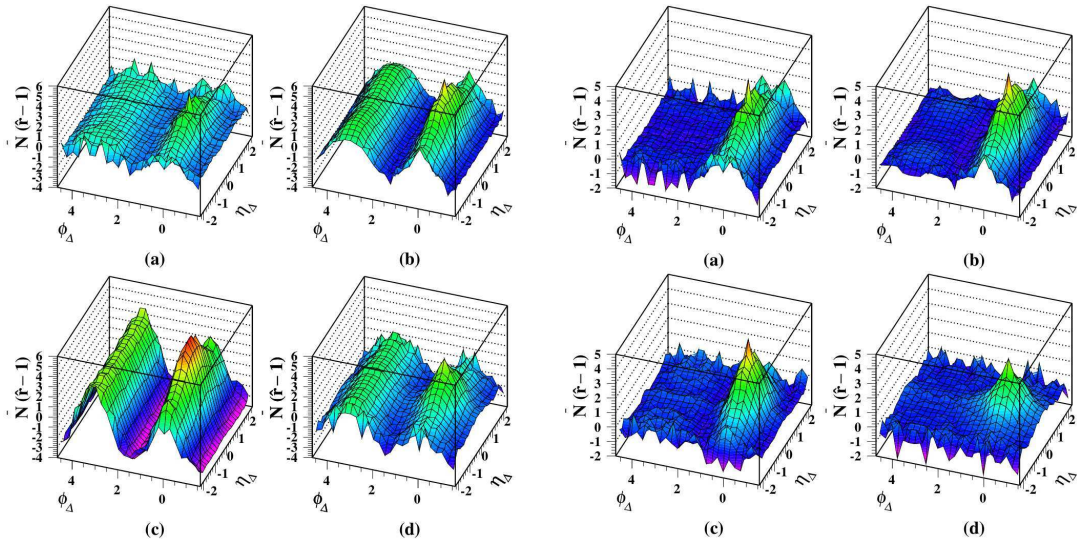


Figure 2.6: STAR results on Au+Au collisions at 130 GeV. Four left plots: two-particle charge-independent (all charged) correlations for central (a) to peripheral (d) collisions. Four right plots: the same data but with the results with subtraction of dipole and quadrupole components (more details in the text). See Appendix A for detailed definition of vertical scale in the plots. Figure taken from Ref. [62].

The hard component of all charged pairs (Fig. 2.5, second from the right) shows near-side peak being a result of correlations rising from **minijets**⁵ and a broad away-side ($\phi_\Delta \approx \pi$) enhancement explained as correlations between particles from one of back-to-back jet of a di-jet with members of the opposite back-to-back jet.

Similar analyses of Au+Au collisions, firstly at $\sqrt{s_{NN}} = 130$ [62] and later at 62 and

⁵R.J. Porter and T. Trainor define the term *minijet* as a jet appearing in minimum-bias parton fragmentation [61].

⁶ $y_t \equiv \ln(m_t + p_t)/m_\pi$ where $m_t \equiv \sqrt{p_t^2 + m_\pi^2}$. Transverse rapidity subspace served in Ref. [61] as a cut space to separate soft and hard component subspaces. Here, some variables were denoted unconventionally, but their meanings are the same, namely: $m_t \equiv m_T$, $p_t \equiv p_T$, $y_t \equiv y_T$, $\eta_\Delta \equiv \Delta\eta$, and $\phi_\Delta \equiv \Delta\phi$.

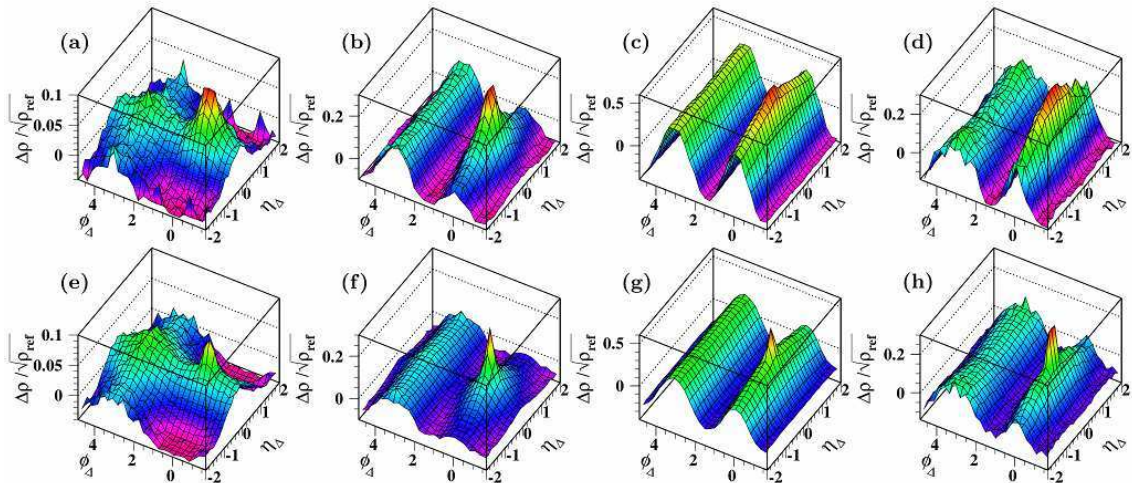


Figure 2.7: Perspective views of two-dimensional charge-independent angular correlations $\Delta\rho/\sqrt{\rho_{\text{ref}}}$ (Appendix A for the detailed description of $\Delta\rho/\sqrt{\rho_{\text{ref}}}$ variable) on $(\eta_\Delta, \phi_\Delta)$ in the STAR experiment for Au+Au collisions at $\sqrt{s_{NN}} = 200$ and 62 GeV (upper and lower rows, respectively). Centrality changes from left to right from most-peripheral to most-central events. Figure taken from Ref. [63].

200 GeV [63], were performed. The results⁷ from $\sqrt{s_{NN}} = 130$ GeV (see Fig. 2.6, four left plots) presented the following structures: a sinusoidal-shape $\propto \cos(2\phi_\Delta)$ (referred as quadruple component) – a structure connected with **elliptic flow**, additional enhancement $\propto \cos(\phi_\Delta)$ called a dipole component being a result of **transverse momentum conservation** in a thermal system, and a near-side peak interpreted as an effect of minijets. The away-side enhancement (coming from back-to-back jet originating from a parton scattering through medium and losing energy) was not observed. After subtraction of dipole and quadruple components (see Fig. 2.6, four right plots), the distributions showed an absence of longitudinal one-dimensional gaussian structure which was visible in p+p collisions (see Fig. 2.5, second from the left). The absence was explained as a strong suppression of longitudinal string degrees of freedom even in peripheral Au+Au collisions. The first appearance of **the ridge** structure was also observed there as a broad long-range (wide in $\eta_\Delta \equiv \Delta\eta$) enhancement at the near-side for more central collisions. It was explained as a result of strong coupling of energetic partons, which would create high jet peak in vacuum during p+p collisions, with a longitudinally-expanding colored medium, developed in central collisions, causing them to dissipate in that medium and making the peak “melted”. More information about the ridge will be provided in the next section.

The latter analyses (presented in Fig. 2.7) at 62 and 200 GeV discovered a significant evolution of the structures with centrality [63]. The results from the most peripheral Au+Au collisions (see Fig. 2.7, top left for 200 GeV and bottom left for 62 GeV) are qualitatively similar to the results from p+p (e.g. Fig. 2.5) with a near-side peak, away-side one-dimensional enhancement (away-side ridge) and longitudinal, one-dimensional enhancement along ϕ_Δ . However, when going to more central collisions, the latter enhancement disappears, while the away-side ridge increases together with a similar ridge appearing at the near-side.

⁷Primary charged hadrons with $0.15 \leq p_T \leq 2$ GeV/c and $|\eta| \leq 1.3$ were taken to the analysis.

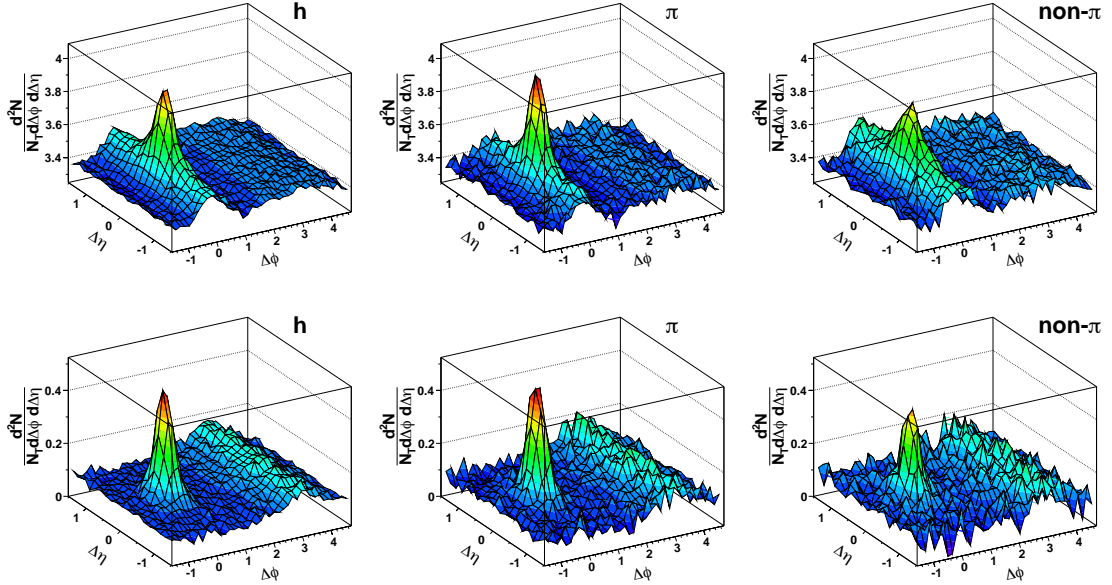


Figure 2.8: STAR results on two-dimensional $\Delta\phi$ vs. $\Delta\eta$ triggered correlations for charged hadrons (left), pions (middle) and non-pions (right). Results from 0-10% most-central Au+Au (top row) and minimum bias d+Au (bottom row) collisions at 200 GeV. Trigger particle momenta were in range $4 < p_T^{\text{trig}} < 5$ GeV/c while their associated particles were in range $1.5 < p_T^{\text{assoc}} < 4$ GeV/c. N_T is the number of trigger particles. Figure taken from Ref. [64].

Recently, STAR published results on $\Delta\eta\Delta\phi$ triggered correlations⁸ of identified particles in Au+Au and d+Au interactions [64]. Results are presented in Fig. 2.8. In central Au+Au collisions slightly stronger near-side ridge was observed in non-pion particles while jet-peak ($\Delta\eta, \Delta\phi \approx (0, 0)$) was stronger for pions. In minimum bias⁹ d+Au interactions, the near-side ridge was not observed, but the conclusion concerning jet-peak was similar to the one from Au+Au. STAR presented also $\Delta\eta\Delta\phi$ results from the Beam Energy Scan where more detailed studies of the ridge were performed [65].

The PHOBOS experiment at RHIC performed an analysis of two-particle angular correlations in p+p collisions at $\sqrt{s_{NN}} = 200$ and 410 GeV as well as in Cu+Cu and Au+Au collisions at $\sqrt{s_{NN}} = 200$ GeV. The results of the system-size dependence are presented in Fig. 2.9. In p+p collisions [66] two main structures were observed: a longitudinal gaussian hill along full $\Delta\phi$ range broadening towards larger $\Delta\phi$ (interpreted as strings fragmentation) and the near-side peak at $\Delta\eta \approx 0$ and $\Delta\phi \approx 0$ (Bose-Einstein correlations and contribution of minijets). The results were compared to ISR theoretical predictions (discussed in the previous section) and concluded to be consistent with the low-mass resonance model [59].

The analysis of Cu+Cu and Au+Au collisions at $\sqrt{s_{NN}} = 200$ GeV [67] showed different structures than those in p+p collisions. The resulting structures are qualitatively similar to those presented by the STAR experiment. The one-dimensional gaussian structure (along

⁸In triggered analysis a “trigger” particle with high transverse momentum is correlated with the “associated” particles with high (but lower than the trigger particle) momenta. In this analysis trigger particle was selected in $4 < p_T^{\text{trig}} < 5$ GeV/c range and associated particles in $1.5 < p_T^{\text{assoc}} < 4$ GeV/c.

⁹Minimum bias collisions refer to interactions without any additional centrality selection.

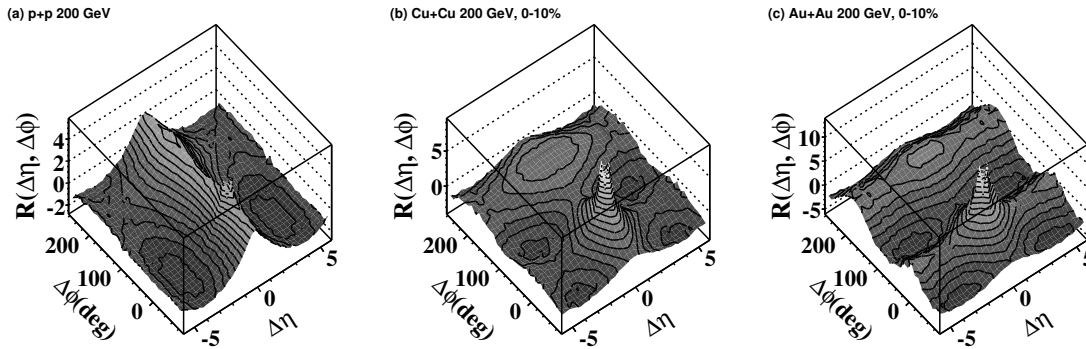


Figure 2.9: PHOBOS results on two-particle correlations (for all charged pairs) in $\Delta\eta$ and $\Delta\phi$ for p+p (a), 0-10% central Cu+Cu (b), and 0-10% central Au+Au (c) collisions at \sqrt{s} or $\sqrt{s_{NN}} = 200$ GeV. See Appendix A for definition of $R(\Delta\eta, \Delta\phi)$. Figure taken from Ref. [67].

$\Delta\phi$ is not visible (in contrary to its presence in p+p results). The near-side peak of minijets is visible in all systems and is the highest in Au+Au collisions. A $\cos(2\Delta\phi)$ modulation, due to elliptic flow, is visible only for Au+Au collisions.

Both analyses [66, 67] were studied in the context of the independent cluster emission model. The cluster properties were studied by an extraction of effective cluster size (the number of particles in a cluster) and cluster decay width (the spread of particles in pseudorapidity).

2.3.2 LHC experiments: CMS, ATLAS, ALICE, and LHCb

This section presents an overview of LHC results ordered in subsections by the system size. The observed structures of one of the experiments are firstly described, then the structures origins are discussed, and at the end, the results from other experiments are compared.

Correlations in Pb+Pb interactions

The CMS experiment analyzed two-particle correlations in Pb+Pb collisions at $\sqrt{s_{NN}} = 2.76$ TeV [68]. Figure 2.10 shows the results on per-trigger-particle associated yield distributions of charged hadrons for different centrality bins. An evolution of structures with changing centrality is visible. The most central events (0-5% of the total cross-section) show flat away-side structure and the near-side ridge. In more peripheral events, $\cos(2\Delta\phi)$ modulation emerges. For the most peripheral collisions (70-80%), the near-side ridge and the modulation vanish leaving only high near-side peak and away-side ridge.

The structures presented above need an explanation. The most noticeable in each figure is the $\cos(2\Delta\phi)$ modulation (or, as STAR called it, the quadruple component) connected with the elliptic flow (see details in Sec. 1.4.1). This effect is less visible in bins of lower and higher centrality. Lack of flow modulation in more central collisions is due to higher isotropy of the system which causes the produced particles covering the full range of azimuthal angle. For mid-peripheral collisions the elliptic flow magnitude is higher, thus the two $\Delta\eta$ -wide structures are visible. In the most peripheral collisions correlations originated from elliptic flow disappear (due to small system size) leaving mainly the structures characteristic for jets, Bose-Einstein correlations, and conservation laws.

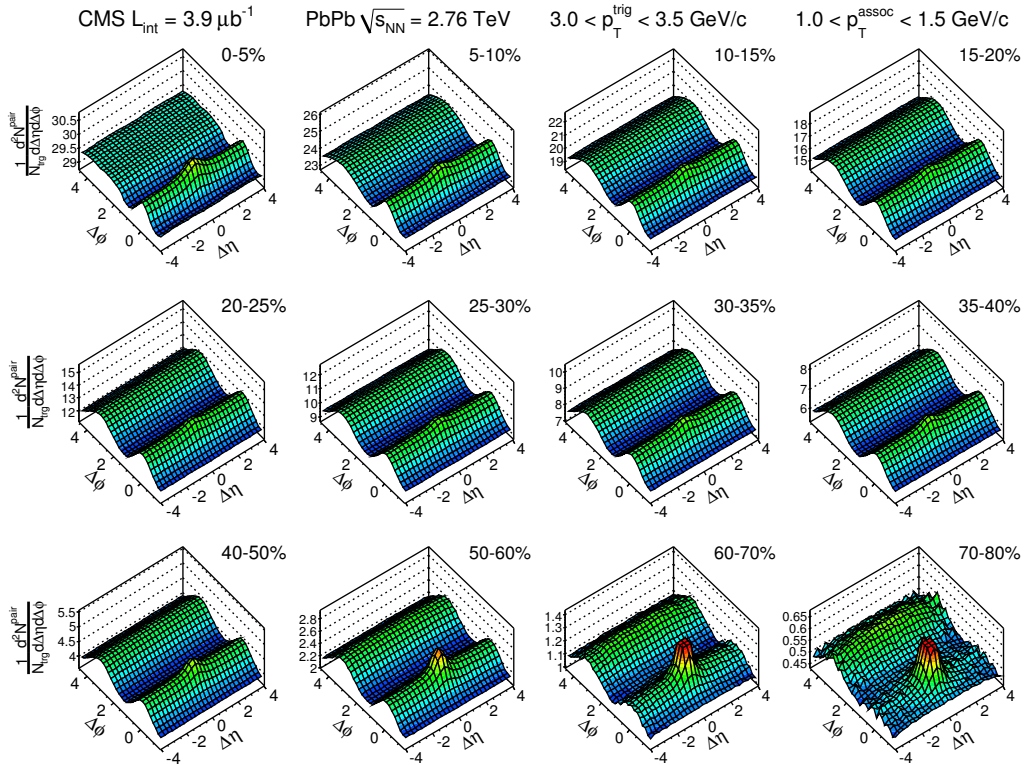


Figure 2.10: CMS results on two-dimensional per-trigger-particle associated yield of charged hadrons as a function of $\Delta\eta$ and $\Delta\phi$ for $3 < p_T^{trig} < 3.5$ GeV/c and $1 < p_T^{assoc} < 1.5$ GeV/c, for twelve centrality ranges of Pb+Pb collisions at $\sqrt{s_{NN}} = 2.76$ TeV. Figure taken from Ref. [68].

The phenomenon of jets was described in Sec. 1.4.1. It appears as a high peak at $(\Delta\eta, \Delta\phi) \approx (0, 0)$. Its excessive height comes from contribution of many particles traveling inside the same jet. The second, widely distributed in $\Delta\eta$, away-side structure (away-side ridge) is due to contribution of particle pairs from the opposite jets of a di-jet. In the most peripheral Pb+Pb collisions only the away-side ridge is visible and there are almost no elliptic flow modulation structures.

In a larger system, as Pb+Pb, the near-side ridge structure was interpreted as an effect of hydrodynamic collective flow which appears in a locally thermalized medium.

The reader may be confused by such an intensive usage of the word “ridge” describing several structures. This word has been used many times through all analyses done in experiments at RHIC and LHC, but it was always referred to one of three following structures:

- **Longitudinal ridge** — a one-dimensional gaussian enhancement (with maximum at $\Delta\eta \approx 0$) which spreads along the full $\Delta\phi$ domain. Visible in p+p collisions and interpreted as a result of longitudinal strings fragmentation.
- **Away-side ridge** — an away-side ($\Delta\phi \approx \pi$) enhancement widely distributed in $\Delta\eta$. Visible in the collisions of different systems (e.g. A+A, high-multiplicity p+p events). It can be interpreted as a result of correlations of particles from one back-to-back jet from a di-jet with particles from the opposite back-to-back jet (note that this

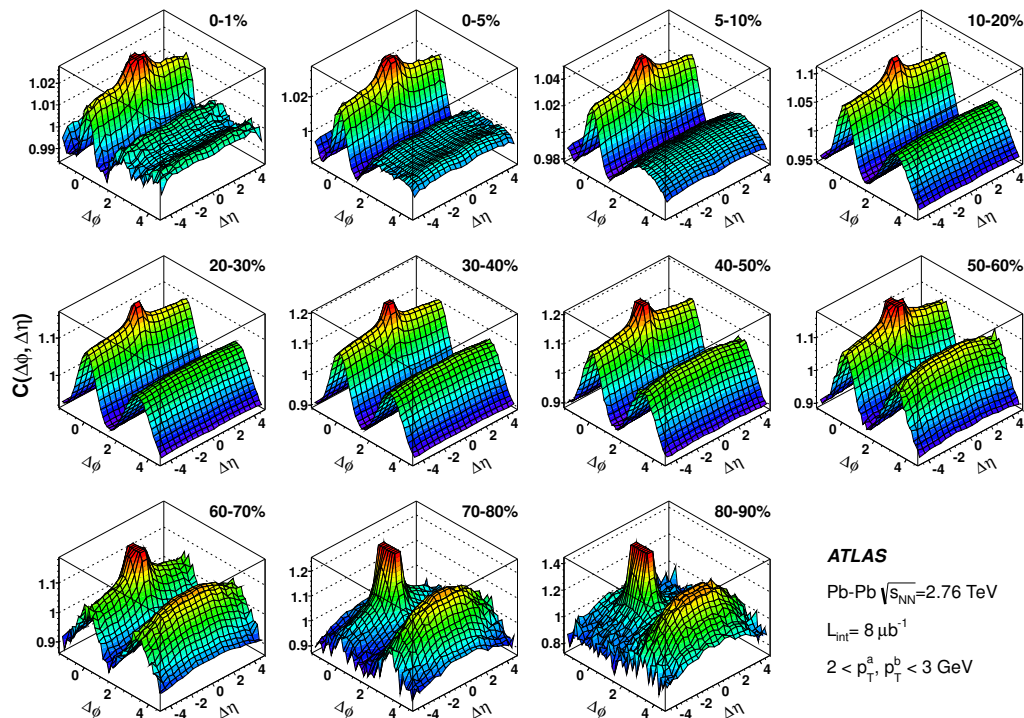


Figure 2.11: ATLAS results on two-dimensional correlations in Pb+Pb collisions at $\sqrt{s_{NN}} = 2.76$ TeV for $2 < p_T^a, p_T^b < 3$ GeV/c in several centrality intervals. Results for all charged particles. Figure taken from Ref. [69].

structure may be not strictly independent of $\Delta\eta$ but it can be more like a very wide gaussian enhancement with maximum at $\Delta\eta = 0$). In the results of correlations at larger systems it is dependent on centrality: more peripheral collisions show structures similar to p+p, while the results from more central events present the enhancement which is more $\Delta\eta$ -independent. Such a structure in mid-peripheral and mid-central Pb+Pb collisions, when accompanied by near-side ridge, is interpreted as a result of collective flow (as said earlier, STAR refers to it as a “quadruple component”).

- **Near-side ridge** — a near-side ($\Delta\phi \approx 0$) enhancement widely distributed in $\Delta\eta$. In heavier systems interpreted as a result of collective hydrodynamic flow (STAR refers to it as an additional “dipole component” to the existing quadruple one). It does not exist in RHIC p+p results, but emerges in high-multiplicity p+p and p+Pb collisions at LHC energies (see below), as well as in Au+Au and Pb+Pb collisions at RHIC and LHC. This is the ridge that troubles the scientists so much nowadays.

The ATLAS results [69] on Pb+Pb collisions at $\sqrt{s_{NN}} = 2.76$ TeV are presented in Fig. 2.11, similarly to CMS, in centrality bins. The particles were chosen in transverse momentum range $2 < p_T^a, p_T^b < 3$ GeV/c. ATLAS results are in a good agreement with CMS. The evolution of structures with changing centrality is visible. In mid-peripheral collisions a strong elliptic flow modulation appears. The most central collisions show near-side enhancement which is higher than the away-side plateau. ATLAS, in very central collisions (0 – 1%) at the region of plateau, shows even a valley which was called “double-hump”. This structure disappears when going to more peripheral collisions, which are

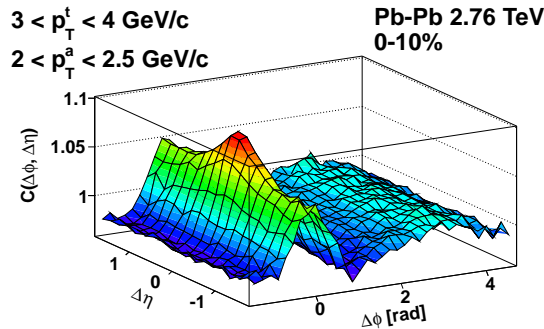


Figure 2.12: Two-particle correlations obtained by ALICE in 10% most central Pb+Pb collisions for all charged particles at $\sqrt{s_{NN}} = 2.76$ TeV. Triggered two-particle correlation function $C(\Delta\eta, \Delta\phi)$ was calculated for trigger particles with $3 < p_T^t < 4$ GeV/c and associated particles with $2 < p_T^a < 2.5$ GeV/c. Figure taken from Ref. [71].

dominated by the structures of jet peak at $(\Delta\eta, \Delta\phi) = (0, 0)$ as well as away-side ridge interplaying with elliptic flow modulation. Both flow and di-jet effects are not visible for very central bins (isotropy of the system and jet quenching), while in the most peripheral collisions flow disappears and away-side ridge can be seen as a longitudinally wide gaussian hill.

There is a limited availability of public ALICE results on Pb+Pb collisions. One of the few publications are Ref. [70] with results on per-trigger associated yield in Pb+Pb interactions at $\sqrt{s_{NN}} = 2.76$ TeV (not shown) and Ref. [71] with the results of two-particle correlation function $C(\Delta\eta, \Delta\phi)$ ¹⁰ at the same energy. The results from Ref. [71] are presented in Fig. 2.12. They agree with results from the most central collisions in CMS and ATLAS. They show jet peak at $(\Delta\eta, \Delta\phi) \approx (0, 0)$ with the ridge at the near-side region and away-side ridge/plateau. No strong $\cos(2\Delta\phi)$ modulation can be observed due to selection of very central events with low anisotropy.

Correlations in p+Pb interactions

Correlations in p+Pb are studied as an intermediate system between large sizes of heavy nuclei collisions and proton-proton interactions, serving as a baseline system. It was expected that QGP created in collisions of A+A systems will not appear in the smaller ones. On the other hand, the phenomena appearing in the most peripheral collisions of heavier nuclei were predicted to be similar as in proton-nucleus system.

Both CMS and ATLAS did the analysis of p+Pb system at $\sqrt{s_{NN}} = 5.02$ TeV [72, 73, 74, 75]. The CMS results for low and high multiplicity events are presented in Fig. 2.13. The ATLAS results for peripheral and central events are shown in Fig. 2.14.

Qualitatively, the results in Figs. 2.13 and 2.14 are almost identical. Results for low multiplicity (more peripheral) events show near-side peak and away-side enhancement over $\Delta\eta$, while the results for high multiplicity (more central) events show the same structures with additional near-side ridge as seen in Pb+Pb. A new structure emerges in peripheral collisions – one-dimensional enhancement along $\Delta\phi$ that connects the near-side peak with the away-side ridge. It is visible in the results of both ATLAS and CMS and is not present

¹⁰The definition of the two-particle correlation function $C(\Delta\eta, \Delta\phi)$ can be found in Ref. [71] or in Sec. 2.1.2.

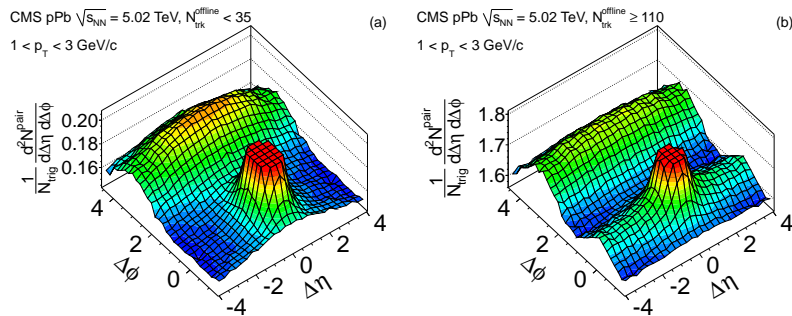


Figure 2.13: Two-particle correlations obtained by CMS for 5.02 TeV p+Pb collisions. Presented for pairs of charged particles with $1 < p_T < 3$ GeV/c in (a) low multiplicity ($N_{trk}^{offline} < 35$) and (b) high multiplicity ($N_{trk}^{offline} \geq 110$) events (see Ref. [72] for details). Figure taken from Ref. [72].

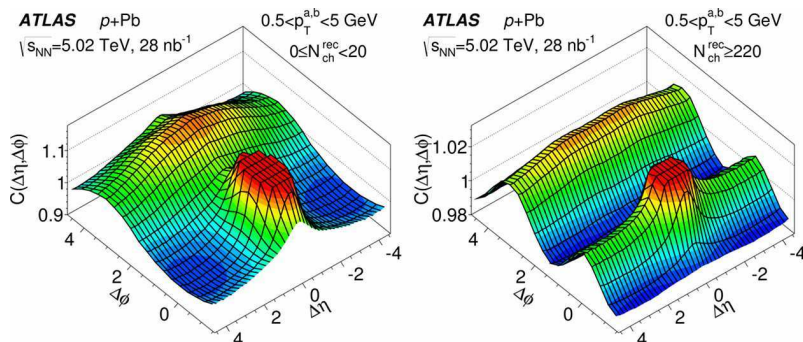


Figure 2.14: Two-dimensional correlation functions for charged particles for (a) peripheral and (b) central events of ATLAS p+Pb collisions at $\sqrt{s_{NN}} = 5.02$ TeV. Results for particles with transverse momentum $0.5 < p_T^{a,b} < 5$ GeV/c. Figure taken from Ref. [73]. See Ref. [74] for previous results.

in high multiplicity (more central) events. The “longitudinal ridge”, as it was called, was already seen in p+p results shown by STAR (see Fig. 2.5, second and third panel or Fig. 2.7, leftmost column) and PHOBOS (see Fig. 2.9, left panel).

In general, the structures visible in low multiplicity (peripheral) p+Pb collisions are qualitatively similar to those from peripheral Pb+Pb (described in the previous subsection). The structures which originate from hard-processes (jets) are the most prominent. The near-side peak comes from the correlations of particles from one jet, while the away-side ridge is a result of combinations of particles from opposite jets. Moreover, the near-side peak is produced also by Bose-Einstein correlations and high- p_T resonance decays while to the away-side ridge the momentum conservation also contributes. The longitudinal ridge may be an effect of low- p_T resonance decays.

For high multiplicity collisions (or central) p+Pb collisions, the near-side ridge appears unexpectedly. This structure caused a lot of discussions in results of p+p system (described in the next subsection). But for the intermediate proton-nucleus system it is still quite probable that a small, hot, and dense medium appears which produces collective flow that may give such a near-side long-range structure.

The LHCb experiment performed the analysis of correlations in p+Pb, only in the

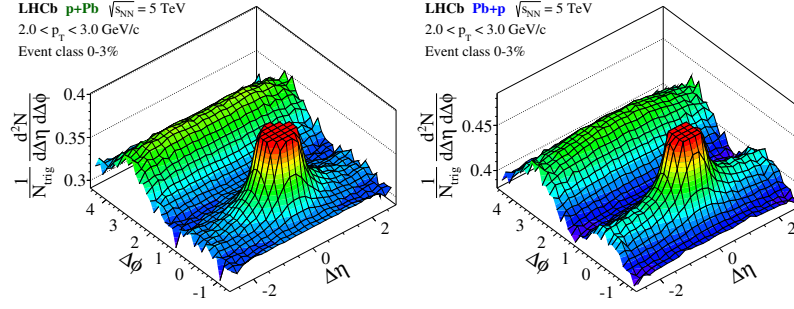


Figure 2.15: LHCb results on two-particle correlations for central events (0-3%) recorded in p+Pb (left) and Pb+p (right) configurations. The (charged) particles are selected in a range $2 < p_T < 3$ GeV/c. Figure taken from Ref. [76].

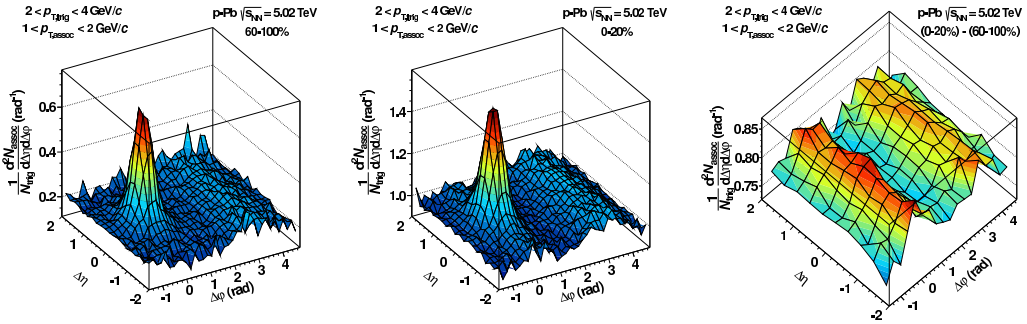


Figure 2.16: The associated yield per trigger particle in $\Delta\phi$ and $\Delta\eta$ for pairs of charged particles with $2 < p_{T,trig} < 4$ GeV/c and $1 < p_{T,assoc} < 2$ GeV/c. ALICE results on p+Pb collisions at $\sqrt{s_{NN}} = 5.02$ TeV for peripheral (left panel) and central (middle panel) collisions (60-100% and 0-20% event classes, respectively). Right panel: results for central collisions with subtracted results for peripheral collisions revealing double ridge structure. Figures taken from Ref. [77].

forward region ($2.0 < \eta < 4.9$). They analyzed data in two beam configurations: towards direction of proton beam and towards direction of lead beam [76]. The results from central events for charged particles selected in transverse momentum range $2 < p_T < 3$ GeV/c are presented in Fig. 2.15. The results agree with high-multiplicity (or central) results from CMS and ATLAS. Correlations in both directions show jet-like structures: a near-side peak and away-side longitudinally-wide enhancement. However, the near-side ridge is more prominent towards lead direction (Fig. 2.15, right) while only slightly visible towards proton direction (Fig. 2.15, left).

The analysis of two-particle correlations in p+Pb collisions at $\sqrt{s_{NN}} = 5.02$ TeV were done also by ALICE [77]. Figure 2.16 presents the results on the analysis of associated yield per trigger particle for charged particles with trigger particle transverse momentum $2 < p_{T,trig} < 4$ GeV/c and particles associated to it with transverse momenta $1 < p_{T,assoc} < 2$ GeV/c. Results are shown for two centrality classes. Namely, Fig. 2.16, left if for peripheral events (60-100%) and Fig. 2.16, middle for central events (0-20%). For both centralities correlations from jets are visible: high peak at $(\Delta\eta, \Delta\phi) \approx (0, 0)$ and elongated structure (away-side ridge) at $\Delta\phi \approx \pi$. Although the structures are similar, those from central collisions are much higher. To quantify the differences, the distribution of peripheral collisions (Fig. 2.16, left) was subtracted from the distribu-

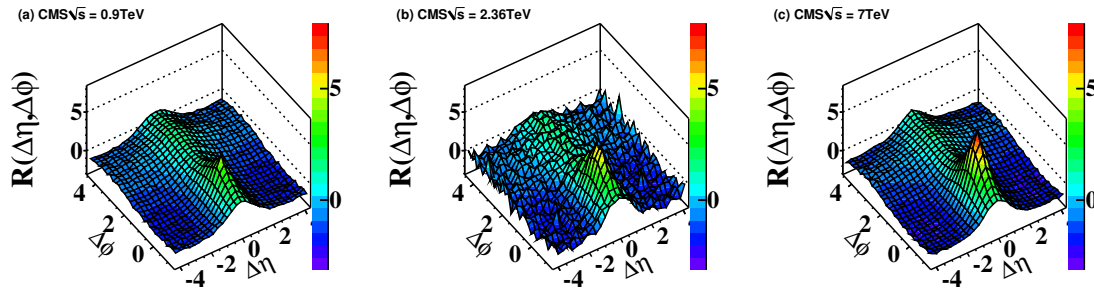


Figure 2.17: CMS two-particle correlation functions measured for charged particles in p+p collisions at $\sqrt{s} = 0.9, 2.36,$ and 7 TeV. Figure taken from Ref. [80].

tral ones (Fig. 2.16, middle). The result presented in the right panel of Fig. 2.16 shows a distinct double ridge structure. The structure of double ridge is similar to the structure generated by elliptic flow, but an explanation in terms of the Color Glass Condensate is also possible [78, 79].

Correlations in p+p interactions

Results from proton-proton interactions were originally meant to serve as a base system (without QGP) and no interesting structures, except of jets, were expected. However, the reality appeared to be different.

CMS studied the two-particle correlations in p+p at various energies. Minimum bias p+p collisions were studied at $\sqrt{s} = 0.9, 2.36,$ and 7 TeV [80, 81] in the context of the Independent Cluster Model (ICM, see Sec. 2.2 for details). The results are presented in Fig. 2.17 and show a gaussian structure along $\Delta\eta$ becoming broader towards larger $\Delta\phi$ and visible for all energies. CMS interpretation of these structures in the context of ICM was that the narrow near-side peak is a contribution from higher p_T clusters (like jets), while the longitudinal enhancement, broadening towards away-side, originates from decays of low p_T clusters (string fragmentation) [81]. Additional contribution of HBT effect (Bose-Einstein correlations) is also probable in the near-side peak region. The results are qualitatively similar to PHOBOS results presented in the left panel of Fig. 2.9.

A shocking result was shown by CMS in 2010 [80] presenting a ridge-like structure in the two-particle correlations at higher transverse momenta ($1 < p_T < 3$ GeV/c) in high multiplicity p+p collisions at 7 TeV (Fig. 2.18, bottom right). A recent analysis for p+p collisions at $\sqrt{s} = 13$ TeV [82] confirms such observation (Fig. 2.19, right). The near-side ridge structure was not expected in p+p system, where Quark-Gluon Plasma was not expected to appear, therefore it emerged many discussions and theories of its origin. The obvious conclusion on the appearance of this structure is that correlations in such a big rapidity separation should have their source in a very early stage of the collision or even before the collision [83]. The Color Glass Condensate theory tries to describe it as a gluon saturation in CGC-Glasma approach [84]. However, many studies were done also in explaining the ridge in terms of collective hydrodynamic flow [85, 86].

The ATLAS experiment studied two-particle correlations in p+p collisions at $\sqrt{s} = 900$ GeV and 7 TeV [87]. Minimum bias results are presented in Fig. 2.20. As in CMS, the most visible structures are the sharp peak around $(\Delta\eta, \Delta\phi) = (0, 0)$ and away-side elongated structure at $\Delta\phi \approx \pi$. They are produced by correlations inside di-jets. The

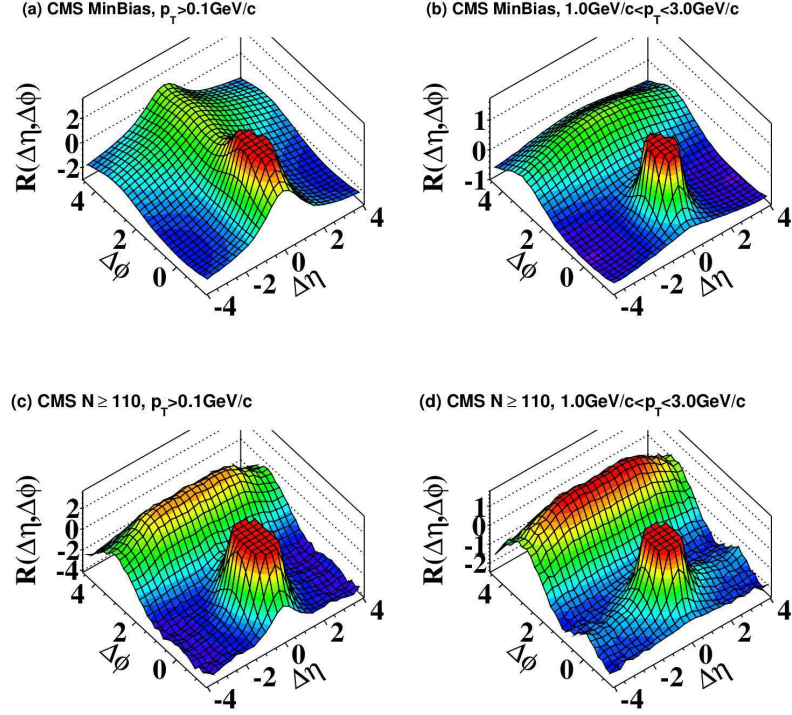


Figure 2.18: Two-particle correlation functions for 7 TeV p+p collisions obtained for charged particles by CMS in (a) minimum bias events with $p_T > 0.1$ GeV/c, (b) minimum bias events with $1 < p_T < 3$ GeV/c, (c) high multiplicity ($N_{\text{trk}}^{\text{offline}} \geq 110$) events with $p_T > 0.1$ GeV/c and (d) high multiplicity ($N_{\text{trk}}^{\text{offline}} \geq 110$) events with $1 < p_T < 3$ GeV/c. Figure taken from Ref. [80].

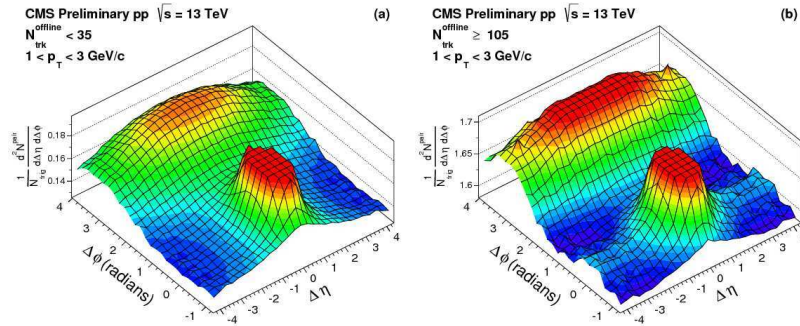


Figure 2.19: CMS two-particle correlations for charged particles in p+p collisions at $\sqrt{s} = 13$ TeV. Results for particles with transverse momentum range $1 < p_T < 3$ GeV/c and in low (left panel) and high (right panel) multiplicity bins. Figure taken from Ref. [82].

gaussian structure along $\Delta\phi$ at $\Delta\eta = 0$ (longitudinal ridge) is better visible than in larger systems. The near-side peak increases with increasing energy of the colliding system. The recent results at $\sqrt{s} = 5.02$ and 13 TeV [88, 73], presented in Fig. 2.21, show correlations for bins with lower (left column) and higher (right column) multiplicities. Only particles with $0.5 < p_T^{a,b} < 5.0$ GeV/c were chosen to the analysis. The distributions show prominent away-side ridge, and additionally, low multiplicity events show enhancement along $\Delta\phi$ centered at $\Delta\eta = 0$ (which may be due to string fragmentation). Results from high multiplicity collisions present near-side ridge similar to that observed by CMS (see Fig. 2.18,

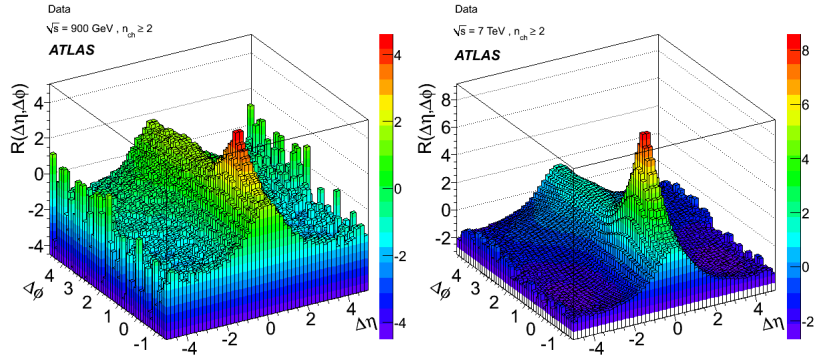


Figure 2.20: ATLAS results on two-particle correlation functions for charged particles in p+p collisions. Minimum bias results at $\sqrt{s} = 900$ GeV (left) and 7 TeV (right). Figure taken from Ref. [87].

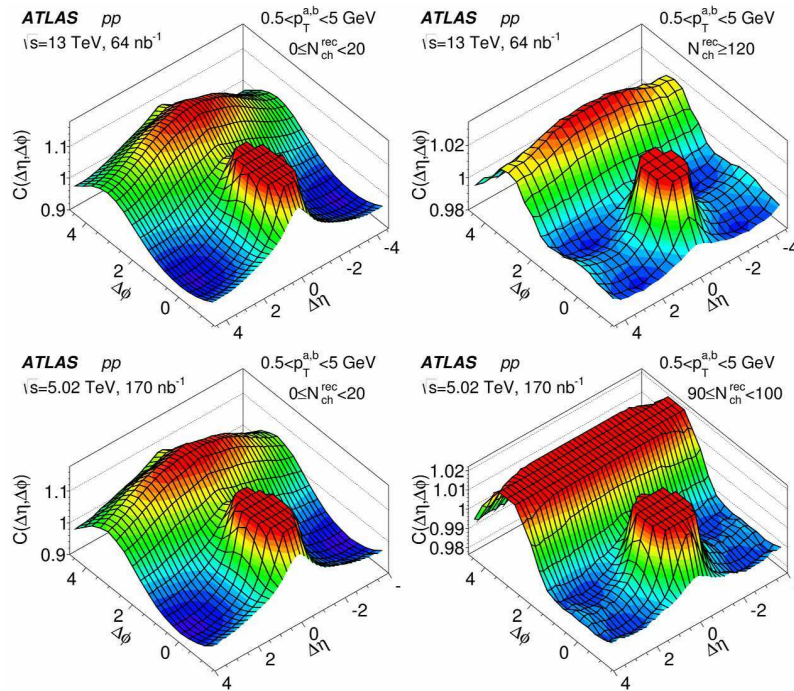


Figure 2.21: ATLAS results on two-particle correlations in p+p collisions at $\sqrt{s} = 5.02$ (lower row) and 13 TeV (upper row). Results for charged particles with transverse momentum range $0.5 < p_T^{a,b} < 5.0$ GeV/c and for lower (left column) and higher (right column) multiplicity bin. Figure taken from Ref. [73]. See Ref. [88] for previous ATLAS results.

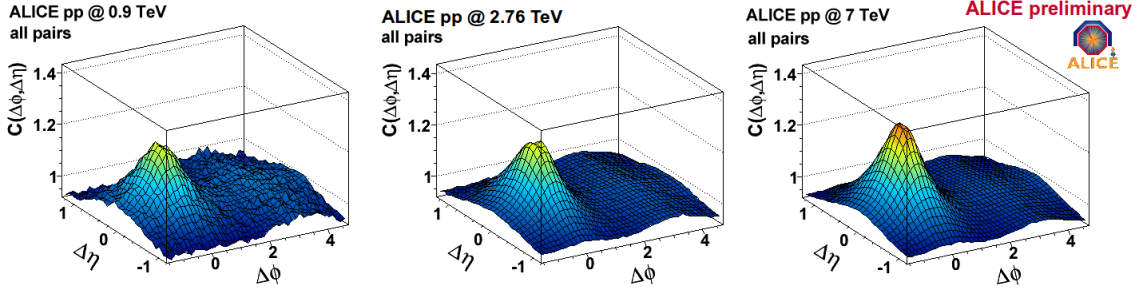


Figure 2.22: ALICE results on two-particle correlation function for charged particles in minimum bias p+p collisions at $\sqrt{s} = 0.9$ (left), 2.76 (middle), and 7 TeV (right). Figure taken from Ref. [89].

bottom right).

The ALICE experiment performed two-particle correlation analysis in p+p collisions at $\sqrt{s} = 0.9, 2.76,$ and 7 TeV [89]. The results from the analysis are presented in Figs. 2.22 and 2.23. The near-side peak becomes stronger with increasing collision energy (see Fig. 2.22), which is explained by higher contribution of hard-scattering processes. In the analysis of dependencies on charge combination and multiplicity (see Fig. 2.23) one can see a near-side peak at $(\Delta\eta, \Delta\phi) = (0, 0)$, corresponding to (mini)jets¹¹ and Bose-Einstein correlations, and an away-side enhancement corresponding to particles coming from opposite jets. Apart from the near-side peak there is also a longitudinal ridge (along $\Delta\phi$) in low multiplicity events which does not appear in high multiplicity events.

A similar analysis of p+p collisions at $\sqrt{s} = 7$ TeV was done but for identified particles [48]: protons, kaons, and pions (see Fig. 2.24). The analysis was performed to check whether two-particle correlations obey global or local conservation laws. Namely, if the correlations obey only global conservation laws, the correlation structures should be independent of the particle species (i.e. momentum, charge, baryon number and strangeness would be conserved only in the scale of the whole event). However, if the correlations obey also local conservation laws (i.e. within every parton fragmentation process), the correlation structures should be different for different particles. Figure 2.24 shows that local conservation laws play a significant role in particle correlations. The near-side peak is the strongest for kaons and significantly lower for protons and pions. The suppression in like-sign proton pairs is observed (called “anti-correlation dip”) at $(\Delta\eta, \Delta\phi) \approx (0, 0)$.

The authors of Ref. [48] proposed a hypothesis that connects the strength of the near-side enhancement for unlike-sign correlations with energetic costs of alternative production mechanisms. Namely, in production of unlike-sign pairs the easiest and the “cheapest” production mechanism is to produce a particle with its anti-particle (π^+ and π^- in case of unlike-sign pions, K^+ and K^- in case of kaons, p and \bar{p} in case of protons). However, other mechanisms of the production are considered which must obey conservation laws. The more difficult is to produce such a configuration, the stronger near-side peak emerges.

- **Pions.** Another solution to produce a particle obeying momentum and charge conservation laws for a produced pion is to produce any other oppositely charged particle. Such alternative solution is “cheap”, therefore the near-side enhancement in unlike-

¹¹The ALICE experiment defines the term “minijet” as a jet created from low momentum-transfer scattering. However, the strict boundary value is not given.

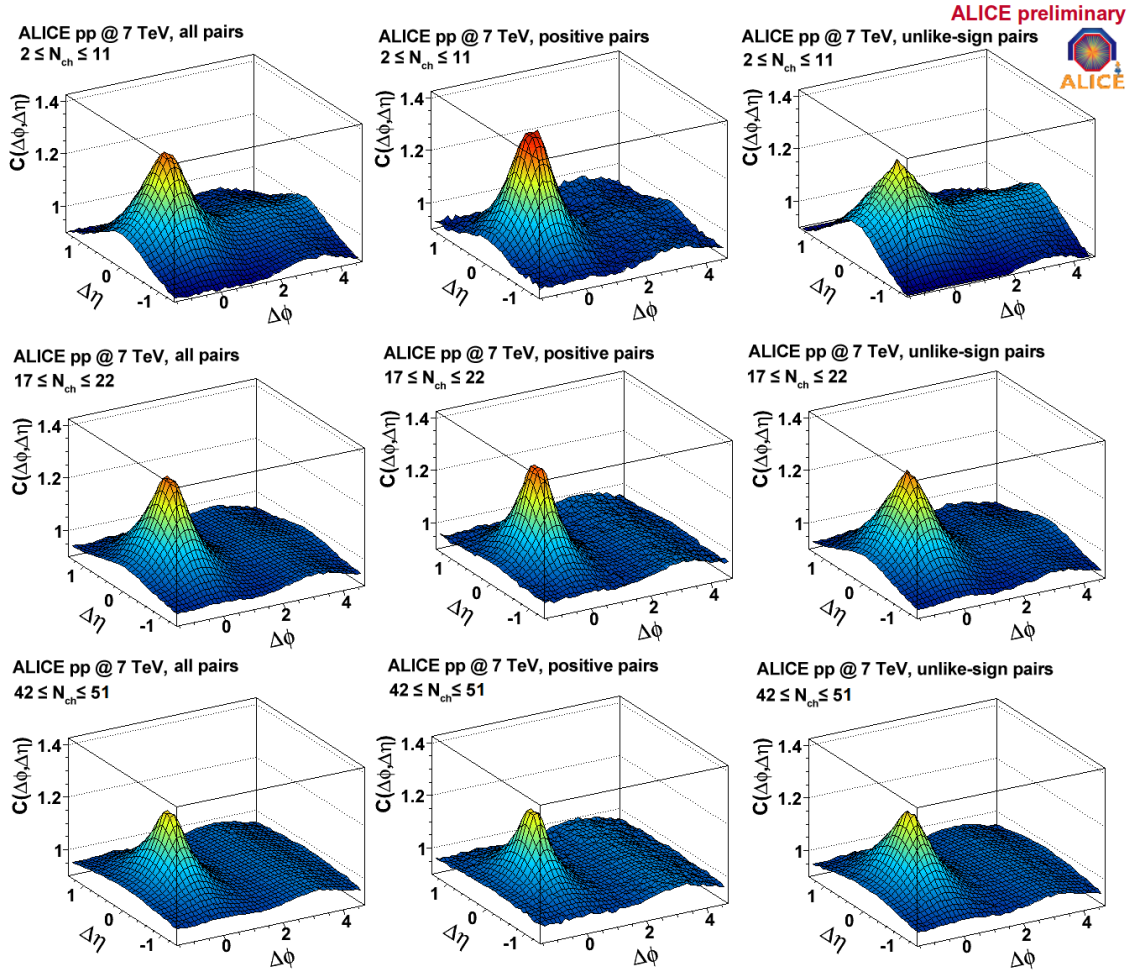


Figure 2.23: ALICE results on two-particle correlation function in p+p collisions at $\sqrt{s} = 7$ TeV. Separate columns present different charge combinations: left – all charged pairs, middle – positively charged pairs and right – unlike-sign pairs. Separate rows present different multiplicity bins. Figure taken from Ref. [89].

sign pion correlations is very low (see Fig. 2.24, bottom right).

- **Protons.** Alternative solution to obey momentum, charge, and baryon number conservation laws of the produced proton would be to produce anti-baryon (i.e. charged anti-baryon or neutral anti-baryon but with additional charged particle; both particles would have to compensate the momentum of the proton). Such alternative solution is rather “expensive”, therefore it produces an enhancement in the two-particle correlation function for unlike-sign protons (see Fig. 2.24, bottom left).
- **Kaons.** Here, the alternative solution to produce kaon (but not anti-kaon) is, for example, producing a Λ particle (to obey strangeness conservation law) which is a baryon, thus it needs to be compensated by an anti-baryon and, additionally, charge must be conserved. Thus, it may require to produce additional charged particle (for example positively charged particle if the anti-baryon was $\bar{\Lambda}$). This solution is extremely “expensive”, therefore it produces a high peak in unlike-sign kaon pairs (see Fig. 2.24, bottom middle).

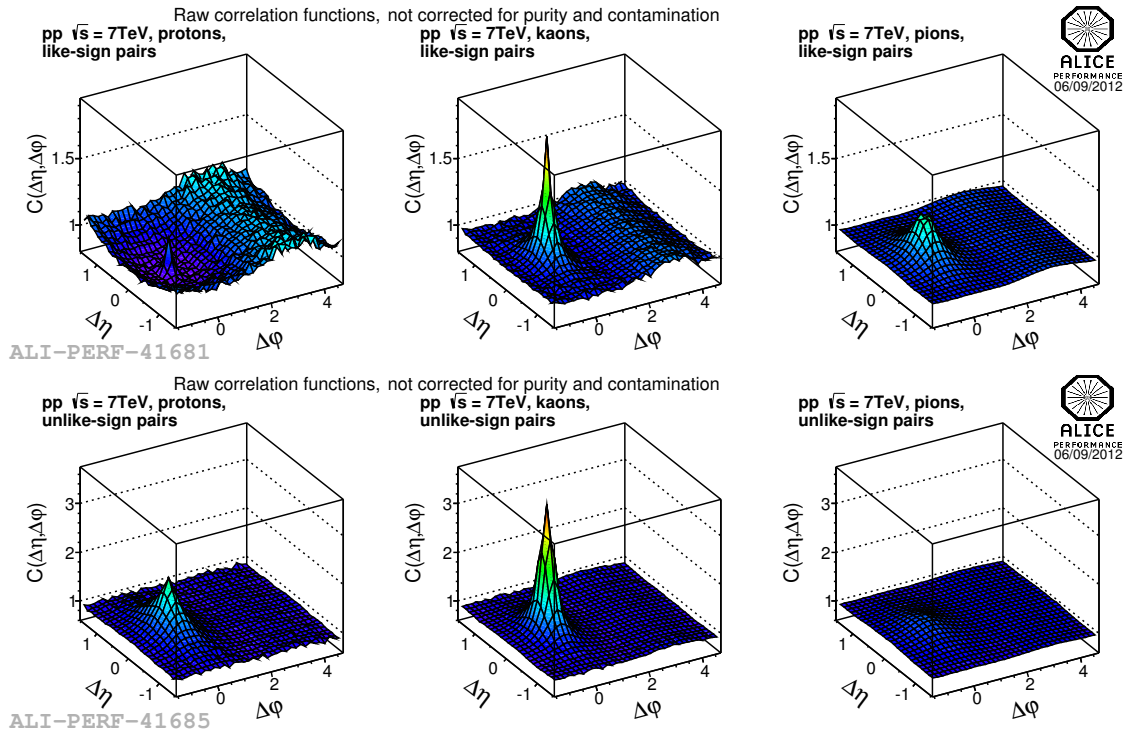


Figure 2.24: ALICE results on two-particle correlation function in p+p collisions at $\sqrt{s} = 7$ TeV for identified particles: protons (left column), kaons (middle column) and pions (right column). Presented for like- and unlike-sign pairs. Results are not corrected for detector efficiency, purity and contamination. Figure taken from Ref. [48].

For like-sign protons the effect is, however, different. Namely, a very distinctive “anti-correlation dip” structure can be noticed (see Fig. 2.24, upper left). The authors of Ref. [48] use the following explanation for this particle species. If the production of protons in one event obeyed only global conservation laws, then the energetic solution would not be very expensive because those protons would be compensated by any two anti-baryons (for example, anti-protons) produced also in the same collision. However, if such production obeyed also local conservation laws, in addition to two protons (which travel close to each other), two anti-protons with similar direction should be created (to compensate baryon number). Moreover, other particles, which travel in the opposite direction, should be also produced to compensate momentum. The rareness of such scenario may produce the dip which is visible in the upper left panel of Fig. 2.24.

It should be however stressed, that Monte Carlo simulations (PYTHIA and PHOJET), which have both conservation laws and string hadronization implemented, do not reproduce the anti-correlation structure [48]. Thus, it is suggested [90] that another phenomenon may be responsible for such structure. One of the interpretations is connected with historical studies of the properties of jets [91], where the mechanism of string hadronization inhibits a creation of two baryons close to each other in rapidity. The phenomenon of “anti-correlation dip” is still under investigation [90]. It should be also added, that the anti-correlation was also observed in the results of correlations in e^+e^- annihilation [92, 93].

Chapter 3

The NA61/SHINE experiment

The NA61/SHINE experiment [94] is a fixed target large acceptance hadron spectrometer located at the Super Proton Synchrotron (SPS) in the north area of the European Organization for Nuclear Research (CERN) near Geneva, Switzerland. It is a successor of the NA49 experiment [36] and uses its detector with an upgraded setup. The acronym SHINE stands for *SPS Heavy Ion and Neutrino Experiment*.

The major goal of NA61/SHINE is to study hadron production in hadron-hadron, hadron-nucleus, and nucleus-nucleus interactions within three programs: the strong interactions program, the neutrino program, and the cosmic rays program.

Within the strong interactions program the experiment studies the properties of the onset of deconfinement and searches for the signatures of the critical point of strongly interacting matter. This is achieved by performing a comprehensive two-dimensional scan of the phase diagram of strongly interacting matter by varying the beam momenta from $13A$ to $158A$ GeV/c ($\sqrt{s_{NN}} = 5.1 - 17.3$ GeV/c) and the system size by colliding the following systems: p+p, Be+Be, Ar+Sc, Xe+La, and Pb+Pb. Figure 3.1 presents estimated (NA49) and expected (NA61/SHINE) chemical freeze-out points of the systems already registered in NA49 (blue points) and NA61/SHINE (green points) or planned to be taken in NA61/SHINE (gray points).

The goal of the neutrino program is to collect data on spectra in p+C interactions, as the reference for the T2K experiment, while the goal of cosmic rays program is to collect data on spectra in p+C, p+p, π +K and K+C interactions as the reference for the cosmic-ray experiments (Pierre-Auger and KASCADE) [96]. Recently, the program of NA61/SHINE was extended by Fermilab neutrino program to collect high-precision hadron production data to improve beam modeling for future experiments at Fermilab [97].

3.1 NA61/SHINE in CERN accelerator complex

Figure 3.2 presents the CERN accelerator complex. The NA61/SHINE experiment is located at one of the branches of SPS (inside region “North Area” in the picture). SPS obtains accelerated protons which originate from linear accelerator Linac2. The Linac2 delivers the particles to PS Booster and, after acceleration, they are sent to the Proton Synchrotron (PS). The protons injected to SPS from PS have the energy of 25 GeV. SPS

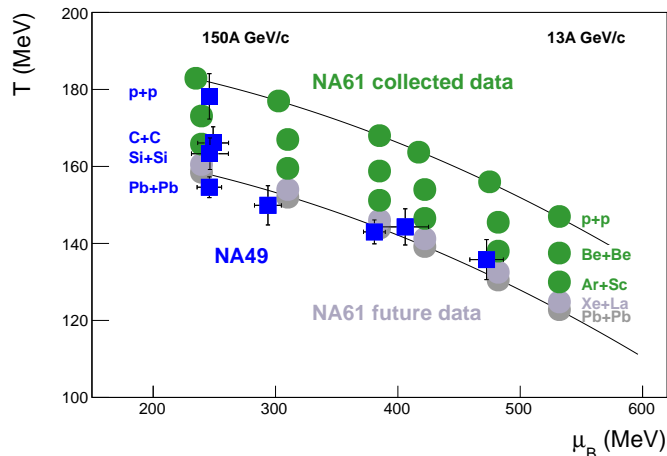


Figure 3.1: Estimated and expected chemical freeze-out points taken in the NA49 and the NA61/SHINE experiments. The points positions are according to Ref. [95].

accelerates them further and delivers to projects such as NA61/SHINE, COMPASS, and CERN Neutrinos to Gran Sasso (CNGS). Protons, accelerated in SPS to the maximal energy of 450 GeV, are also sent further to the Large Hadron Collider.

The complex accelerates ions also. The starting point for ions such as lead, argon, and xenon is Linear accelerator 3 – Linac3. After acceleration in the Low Energy Ion Ring (LEIR) the ions are injected into PS and then to SPS.

3.2 NA61/SHINE detector

As mentioned above, NA61/SHINE is a fixed target experiment. Its setup is presented in Fig. 3.3. The main components of the detector setup are four large volume Time Projection Chambers (TPCs). Going down with the beam, the first two – Vertex TPC 1 and Vertex TPC 2 (VTPC1, VTPC2) – are located inside superconducting magnets. The latter two – Main TPC Left and Main TPC Right (MTPC-L, MTPC-R) – are located on both sides of the beam. There is also smaller TPC – GAP TPC – mounted between VTPCs and measuring particles with the smallest production angles. Behind the Main TPCs, Time-of-Flight (ToF) detector walls are located. Together with TPCs, Time-of-Flight detectors are responsible for particle identification. At the end of the setup the Projectile Spectator Detector – PSD – is located (since 2011, the successor of NA49 VETO calorimeter) which measures the energy deposited by the projectile spectators¹ and in that way determines the centrality of the collision. During 2009 p+p data collection, used in this thesis, the ToF walls and the VETO calorimeter were not used.

3.2.1 Beam detectors, trigger system, Time Projection Chambers, and Time of Flight walls

In order to precisely measure the position of incoming beam particles and establish timing reference, a set of beam position detectors (BPDs) as well as scintillation and

¹Projectile spectators are nucleons from the beam nucleus which do not participate in the collision.

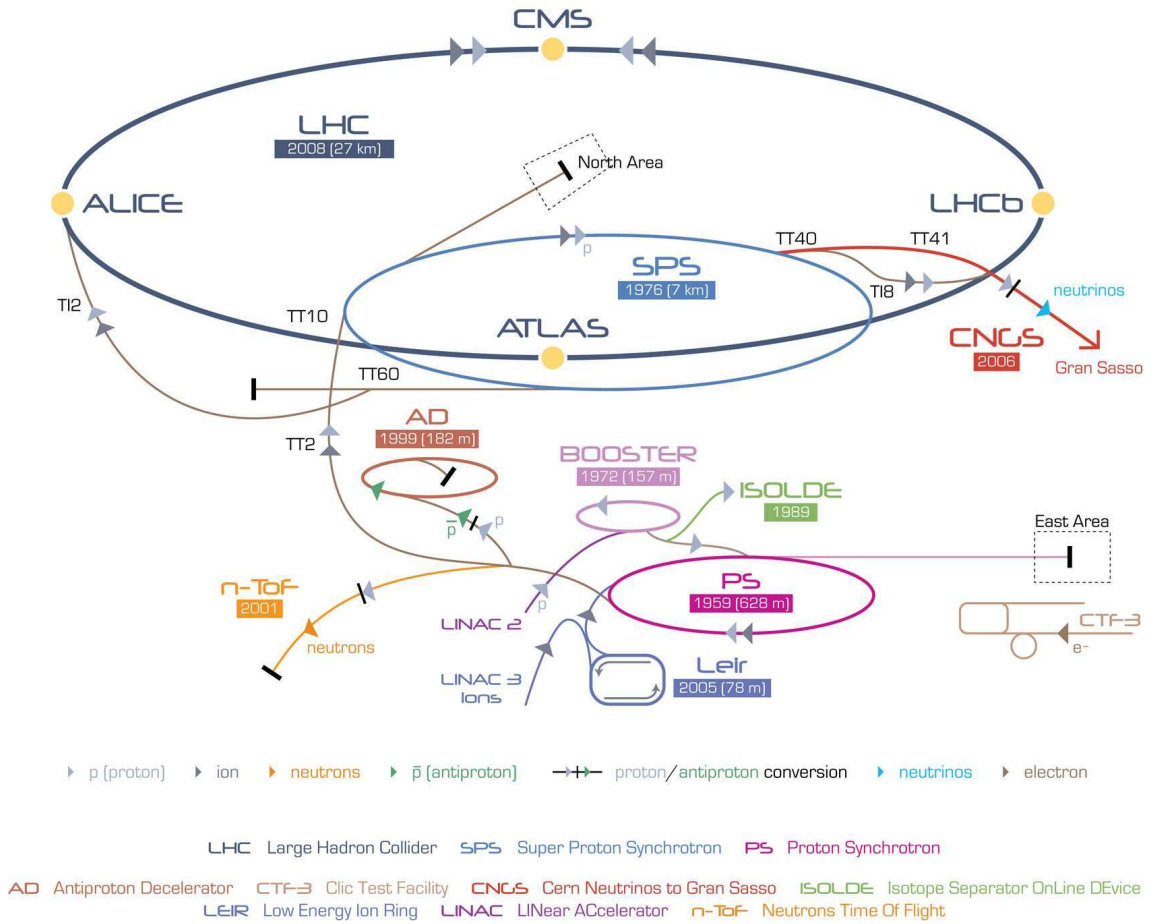


Figure 3.2: The CERN accelerator complex. Figure taken from Ref. [98].

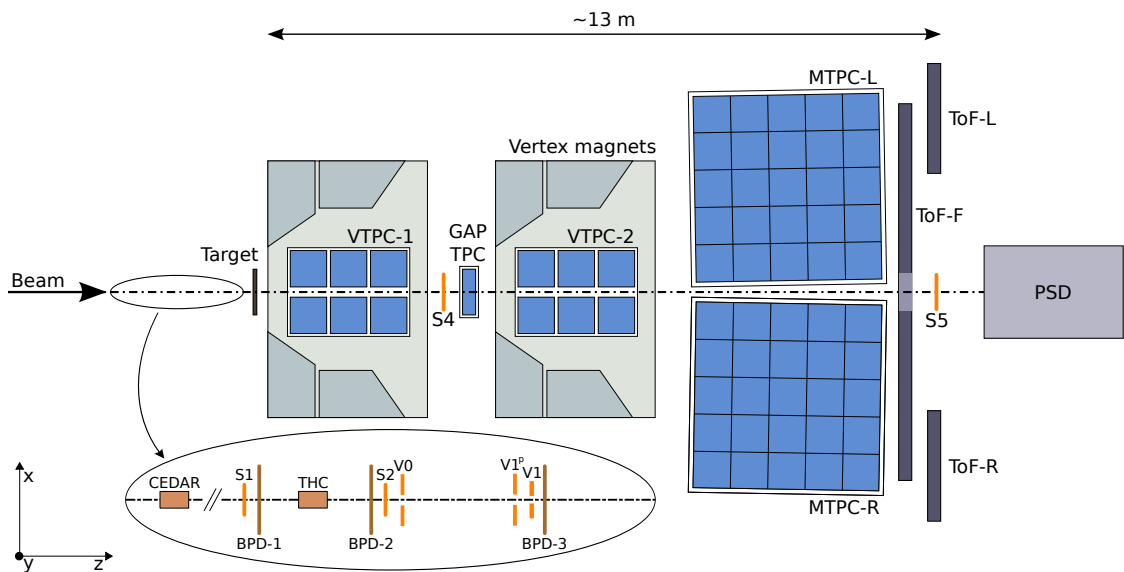


Figure 3.3: Schematic layout of the NA61/SHINE experiment at the CERN SPS. Figure taken from Ref. [94].

| Trigger | Configuration |
|---------|--|
| T1 | $S1 \wedge S2 \wedge \overline{V0} \wedge \overline{V1} \wedge \overline{V1^p} \wedge \overline{THC} \wedge CEDAR$ |
| T2 | $T1 \wedge \overline{S4}$ |

Table 3.1: Trigger configuration during p+p run in 2009. Bars over the counter symbols denote the anti-coincidence.

Cerenkov counters are installed upstream of the target on the beam line. The enlarged region in Fig. 3.3 presents the set of BPDs and triggers used during 2009 data taking.

Incoming protons are identified by so-called T1 trigger which consists of:

- CEDAR (coincidence in the trigger logic) and threshold counter (THC, anti-coincidence in the trigger logic);
- Two scintillation counters – S1 and S2. Both counters detect the beam, while S1 fires also the trigger;
- Three veto counters – V0, V1 and V1^p used in the anti-coincidence in order to reduce unwanted upstream interactions along the beam line.

Together with T1 trigger which selects beam protons, another one – T2 trigger – is used to select interactions in the target. The T2 trigger needs a presence of beam protons (T1 trigger in the coincidence) together with their absence behind the target (anticoincidence of the S4 counter). Both T1 and T2 trigger definitions are summarized in Tab. 3.1.

The positions in the transverse plane of particles with respect to the beam are measured by a set of beam position detectors (BPD-1/2/3 in Fig. 3.3), which are small proportional chambers. Each BPD measures the position of particles selected by the trigger using two planes of orthogonal strips (see Ref. [94] for details).

Time Projection Chambers are the main tracking devices of the NA61/SHINE experiment. The architecture of TPCs allows to reconstruct and precisely measure energy loss of particles (dE/dx). They consist of large gas volumes which are ionized by the particles. The electrons produced in the ionization drift with constant velocity in the electric field towards the top plate of a TPC. The number of electrons, their positions, and arrival times are measured there with proportional wire chambers.

Two VTPCs are located inside super-conducting dipole magnets (VTX-1 and VTX-2). Its maximal total bending power of 9 Tm is used during runs with beam momentum of 158A GeV/c and scaled down proportionally when beams with lower momenta are delivered to the detector. Magnetic field produced by the magnets bends particles with Lorentz force. This serves two purposes: to distribute bent tracks more uniformly within MTPC volumes (lower track density makes its further reconstruction easier) and to make determination of momentum and charge possible.

In case of the NA61/SHINE experiment, the coordinate system is a right-handed Cartesian one. The z -axis overlaps with beam axis, y -axis is the drift direction of electrons in the TPCs, and x -axis is the direction towards Jura mountains (see Fig. 3.3). The magnetic field bends positive particles towards positive x values. The (0, 0, 0) point of the coordinate system is in the center of VTPC2 magnet.

Time of Flight walls (see: ToF-L, ToF-R, ToF-F in Fig. 3.3), installed behind MTPCs, are a large set of rectangular scintillation detectors serving as an independent particle

identification method. The time resolution of the detectors was measured to be below 100 ps. However, ToFs were not used in the analysis presented in this thesis.

3.2.2 Upgrades of NA61

The NA61/SHINE experiment developed several upgrades of the old NA49 detector. The most important are:

- The Projectile Spectator Detector — a calorimeter which measures projectile spectators energy in nucleus-nucleus collisions. Its two main purposes are: selection of the interaction event at the trigger level and a possibility to select the centrality of the collision during offline analysis. Precise event-by-event spectators energy measurement allows to determine the number of interacting nucleons with the resolution of one nucleon (in the studied energy range), which is very important for the study of fluctuations (see Sec. 1.5) sensitive to the number of interacting nucleons.
- The Low Momentum Particle Detector — a detector which consists of two small size TPC chambers placed on the two sides of the target. It serves to select the centrality in hadron-nucleus collisions by measuring low momentum protons emitted by the target during interaction (so-called “gray protons”).
- The Helium Beam Pipes — installed behind the target in the gas volume of the VTTPCs in order to decrease the number of δ -electrons and off-target interactions.
- The A and Z detectors — installed to be used during Be+Be runs serving to precisely determine the composition of the secondary ion beam and verify if it consists only of ${}^7\text{Be}$ isotope.
- Forward TPCs (FTPCs) — two small TPC chambers which will be installed right before and after MTPC to cover forward rapidity region. The two main goals of these two chambers will be the measurement of secondary protons for the neutrino program and the measurement of high-momentum part of π^+ production.
- Vertex Detector (VD) — will be used to measure open charm in A+A collisions. It will be located between target and VTTPC1 and will consist of four silicon chips of high time resolution and high efficiency of track registration. Short life-time of charmed D mesons ($c\tau$ about few hundreds of micrometers) implies a small distance between primary vertex and D mesons decay vertices, thus the four walls of silicon chips of VD will be located only 5, 10, 15, and 20 cm away of the target.

3.3 Software, data calibration, and reconstruction

The NA61/SHINE experiment has been developing its own software framework – *SHINE Offline Framework* – to make every step of data processing (calibration, reconstruction, simulation, physics analysis) consistent with each other and to create an uniform processing environment for the data [99]. However, for 2009 data an old calibration and reconstruction methods were used [100] which involved DSPACK package [101] and an older processing environment – ROOT61 [102].

The calibration consists of two stages: making direct measurements during data taking and extraction and multiple processing of directly measured data to optimize calibration constants connected with the detector. The parameters of the detector to be adjusted are:

- detector geometry, TPC drift velocities and residual corrections,
- magnetic field settings,
- time-of-flight measurements,
- specific energy loss measurements.

After every step of calibration, a reconstruction of data with new calibration constants is needed to verify whether the constants are optimized. The reconstruction of data consists of the following steps:

1. Information from hits in BPDs are used to reconstruct beam track.
2. Raw data from all TPCs clusters² is used and then, center-of-gravity of each cluster as well as total deposited charge are calculated.
3. Track segments (tracklets) are formed in each TPC separately.
4. Tracklets are matched to form a global track.
5. The global track is fitted with the existence of magnetic field; fit parameters are determined at the first measured TPC cluster.
6. The interaction vertex is determined using information from BPDs and multiple global tracks trajectories.
7. Using determined position of the interaction vertex, the global track trajectory is fitted once again and its momentum is calculated.
8. The global track is matched with points left by particles detected in ToF detectors.

3.4 Simulation chain

Data collected from simulation process serve for two purposes: to make a possibility of comparison to the results obtained from real data and to correct the registered and reconstructed data for the NA61/SHINE detector response (i.e. reconstruction efficiency, trigger-bias, etc.). In the analysis reported in this thesis, the EPOS model (EPOS1.99) was used [103]. The simulation chain, including processing through the NA61/SHINE detector response and geometry, is as follows:

1. The EPOS model is used to generate inelastic p+p interactions.
2. Tracks generated in EPOS are propagated virtually through the geometry of the NA61/SHINE detector using GEANT 3.21 package [104]. This includes interactions with detector material, magnetic field and other physics processes such as decays and particle interactions.

²Cluster is a group of TPC pads with signal amplitudes above a threshold value i.e. a group of pads which registered a charge created by a particle that traveled through the TPC volume.

3. Propagated tracks are digitized and virtually affected by the NA61 detector hardware simulation. The interaction trigger simulation is also applied.
4. Tracks processed in such a way are then stored in a file of the same format as data registered during physics runs.
5. Simulated data are then processed through the reconstruction process as described in Sec. 3.3.
6. Finally, the cluster positions information are used to match the reconstructed tracks to the simulated ones.

The simulated data processed this way imitate real data as close as possible.

Chapter 4

Correlations in p+p energy scan

Proton-proton interactions were taken by the NA61/SHINE experiment in year 2009. They were produced by hitting secondary proton beam¹ accelerated in the SPS (see Sec. 3.1) onto 20 cm long liquid hydrogen target (LHT) and recorded using the NA61/SHINE detector (see Sec. 3.2). The reconstruction process was described in Sec. 3.3. Two target configurations were used during data taking: with LHT reservoir filled with liquid hydrogen (so-called “full-target”, $\approx 90\%$ of full statistics) and LHT emptied (so-called “empty-target”, $\approx 10\%$ of full statistics). The latter configuration serves as a base of correction for off-target interactions contribution, however in this thesis only “full-target” events were used. The number of recorded events for each beam momentum are presented in Tab. 4.1.

| p_{beam} [GeV/c] | $\sqrt{s_{NN}}$ [GeV] | Events read |
|---------------------------|-----------------------|-------------|
| 20 | 6.3 | 1320141 |
| 31 | 7.6 | 3134122 |
| 40 | 8.7 | 5237600 |
| 80 | 12.3 | 4500114 |
| 158 | 17.3 | 3536838 |

Table 4.1: Number of events used in the analysis. p_{beam} denotes beam momentum. Only “full-target” events are put into the table.

Monte Carlo simulations (EPOS [103] and UrQMD [105, 106] models) were used as a comparison with real data results (see Sec. 4.4). The EPOS model was also used for corrections for detector effects (described in Sec. 4.2.2).

4.1 Event and track selection

4.1.1 2009 p+p data set

The results presented in this thesis come from production *13C018*. To ensure the reconstructed events have the highest quality and contain only on-target inelastic interactions, a set of cuts on events and tracks was applied. Below the list of such cuts is presented.

¹Secondary proton beams of momenta 20-158 GeV/c are obtained from primary proton beam at 400 GeV/c delivered by SPS. See Ref. [94] for details of obtaining secondary proton beam.

| p_{beam} | No cuts | T2 trigger | BPD | WFA |
|-------------------|---------------|-----------------|---------------|---------------|
| 20 GeV/c | 1320141 | 1094031 (83%) | 626877 (47%) | 532463 (40%) |
| 31 GeV/c | 3134122 | 2828336 (90%) | 2075637 (66%) | 1779110 (57%) |
| 40 GeV/c | 5237600 | 4682621 (89%) | 3699268 (71%) | 3146747 (60%) |
| 80 GeV/c | 4500114 | 3774050 (84%) | 2531969 (56%) | 2388541 (53%) |
| 158 GeV/c | 3536838 | 2855877 (81%) | 2146452 (61%) | 2081029 (59%) |
| p_{beam} | Vertex fit | Vertex z pos. | No elastic | |
| 20 GeV/c | 263567 (20%) | 189455 (14%) | 176188 (13%) | |
| 31 GeV/c | 1070935 (34%) | 781055 (25%) | 756267 (24%) | |
| 40 GeV/c | 2014087 (38%) | 1474387 (28%) | 1444288 (28%) | |
| 80 GeV/c | 1810465 (40%) | 1358294 (30%) | 1343367 (30%) | |
| 158 GeV/c | 1812872 (51%) | 1384526 (39%) | 1373807 (39%) | |

Table 4.2: Event cuts statistics for 2009 p+p data.

Event cuts

All events had to pass the following conditions:

- T2 trigger cut — the incoming beam had to interact with the target².
- BPD cut — the beam had to leave signals on at least two of three Beam Position Detectors and, additionally, signal on BPD3 was required.
- WFA cut — elimination of off-time interactions by rejecting all beam particles that passed the S1 counter within $|t| < 1 \mu\text{s}$ of the interaction that defined the event.
- Vertex fit — the main vertex was well fitted in the reconstruction process.
- Vertex z position — the fit of the main vertex position on z -axis (along the beam) was defined between $-590 < z_{\text{vtx}} < -570$ cm.
- Inelastic interaction — ensures that event originated from non-elastic interaction. Event was rejected when it contained a positively charged particle with $p > p_{\text{beam}} - 3$ GeV/c.

The statistics for event cuts are presented in Tab. 4.2.

Track cuts

All analyzed tracks had to pass the following conditions:

- Charged cut — ensured that the particle had non-zero electric charge.
- TPC NPoint cut — the track had to leave at least 30 points in all TPCs.
- VTPC or GTPC NPoint cut — regardless of the previous cut, the track had to leave at least 15 points in both Vertex TPCs or 5 points in GAP TPC.

²Due to temporal trigger setting problem, about 10% of runs had wrongly defined T2 trigger. In such part of data, events with T1 trigger only (beam presence) were taken. See Sec. 3.2.1 and Tab. 3.1 for T1 and T2 trigger definitions.

| p_{beam} | No cuts | Charged | TPC NPoints | VTPC or GTPC NPoints |
|-------------------|-----------------|---------------|------------------|----------------------|
| 20 GeV/c | 1576777 | 550803 (35%) | 390091 (25%) | 382368 (24%) |
| 31 GeV/c | 7055321 | 2660784 (38%) | 1960270 (28%) | 1919014 (27%) |
| 40 GeV/c | 14491280 | 5605231 (39%) | 4173451 (29%) | 4083586 (28%) |
| 80 GeV/c | 10650018 | 6863831 (64%) | 5252528 (49%) | 5127942 (48%) |
| 158 GeV/c | 11802661 | 9450510 (80%) | 7239908 (61%) | 7024153 (60%) |
| p_{beam} | B_x and B_y | p_T | $dE/dx e^-, e^+$ | |
| 20 GeV/c | 363381 (23%) | 362777 (23%) | 334711 (21%) | |
| 31 GeV/c | 1855132 (26%) | 1852450 (26%) | 1747699 (25%) | |
| 40 GeV/c | 3972769 (27%) | 3966893 (27%) | 3790782 (26%) | |
| 80 GeV/c | 5044241 (47%) | 5035509 (47%) | 4877862 (46%) | |
| 158 GeV/c | 6943587 (59%) | 6928632 (59%) | 6722539 (57%) | |

Table 4.3: Track cuts statistics for 2009 p+p interactions.

- B_x and B_y cuts — the distance between the main vertex (interaction point) and an extrapolated track fit to the interaction plane had to satisfy the conditions: $|B_x| \leq 4$ cm and $|B_y| \leq 2$ cm.
- Transverse momentum cut — the analysis presented in this thesis rejected all high transverse momentum particles (possible contribution of jets), thus a cut $p_T < 1.5$ GeV/c was applied. However, a short analysis was done with this cut disabled (see Sec. 4.5).
- $dE/dx e^-$ and e^+ cut — δ electrons³ as well as possible products of gamma decays ($\gamma \rightarrow e^- + e^+$) were rejected. To achieve this a graphical cut on dE/dx vs. p plane was applied. An example effect of such a cut is presented in Fig. 4.1. The effect of the cut can be observed as disappearance of the bins around $(\Delta\eta, \Delta\phi) = (0, 0)$.

The statistics for track cuts are presented in Tab. 4.3.

4.1.2 Model simulations

Two kinds of the EPOS1.99 [103] model results were used:

- **Pure MC** — pure events generated by EPOS, not processed by the NA61 reconstruction chain, but only converted to be readable by the ROOT61 software framework. They serve as a theoretical reference.
- **Rec MC** — the same events generated in EPOS and processed by the NA61 reconstruction chain (thus, “contaminated” by the NA61 detector effects, trigger biases, reconstruction software issues, etc.). They imitate real data. See Sec. 3.4 for details.

EPOS [103] simulations were done for the same beam momenta as those in real data. Its results were used as model predictions and also to calculate corrections for detector effects. In order to make model results as similar to data as possible, selections for events and tracks were applied on its output also (see the following subsections).

³Atomic electrons ejected from atoms in matter by the passage of charged particles. These electrons have energy sufficient to ionize electrons from other atoms along their trajectories.

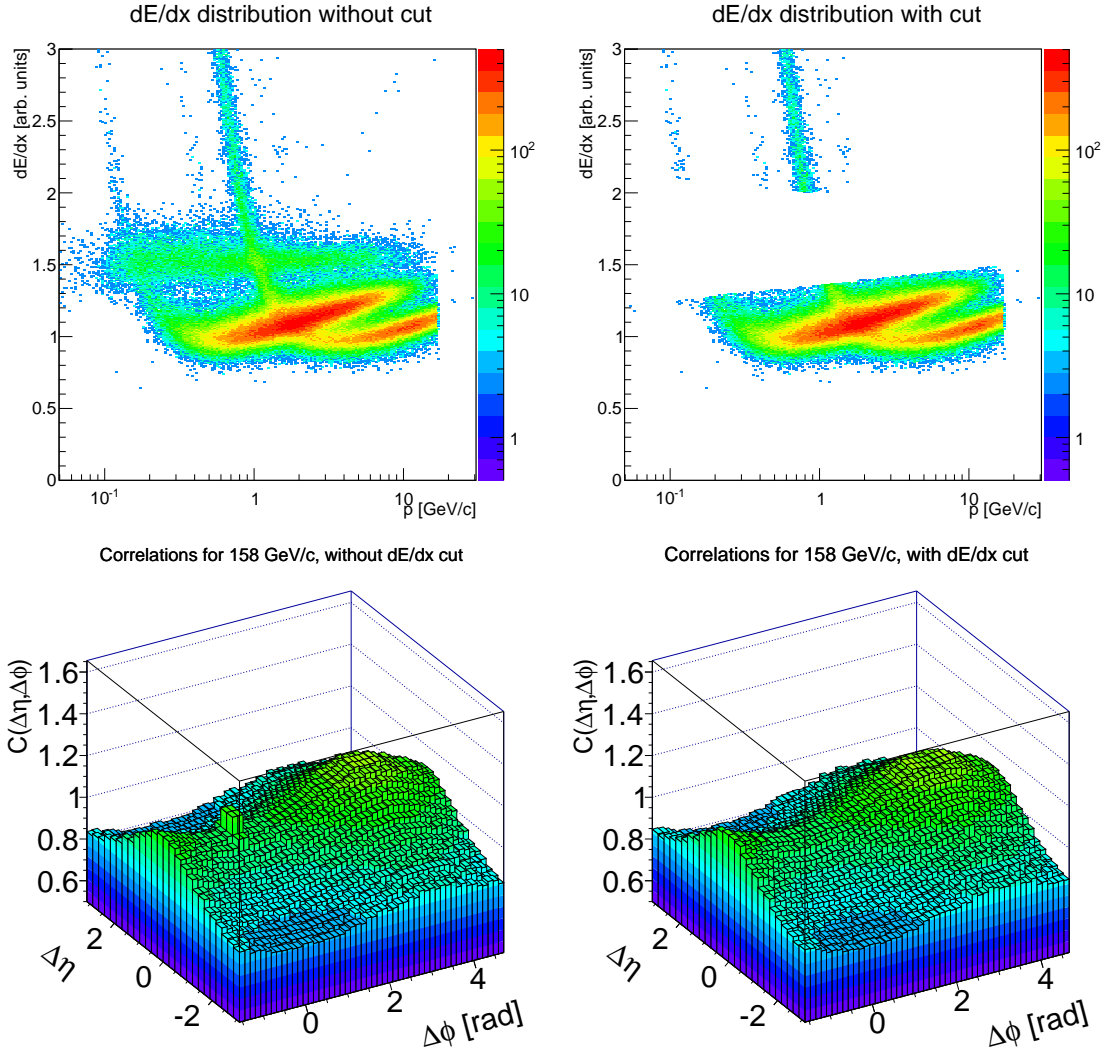


Figure 4.1: Example effect of applying electrons and positrons dE/dx cut on two-particle correlations in p+p interactions at 158 GeV/c. Comparison of dE/dx distributions before and after cut is presented in the top row. $C(\Delta\eta, \Delta\phi)$ correlation functions are presented in the bottom row. Correlation functions in this figure are not corrected for detector effects.

The UrQMD model [105, 106] was used in this thesis only for a theoretical comparison with the NA61 data. All cuts and results of the analysis for beam momenta equal to the ones used in the real data are described in Sec. 4.4.

Pure MC

Monte Carlo events, generated by the EPOS model, are supposed to be theoretical reference and are treated as “ideal”. They do not contain off-target and off-time events, therefore event cuts are not applied to this dataset. A minor set of track selection cuts was applied to ensure that the same kind of particles are analyzed both in Monte Carlo and in real data. The list of track selection cuts is described below:

- StartVertex cut — only primary particles were analyzed.
- Charged cut — only particles with non-zero electric charge were taken into account.

| p_{beam} | No cuts | Start vertex | Charged |
|-------------------|----------------|----------------|------------------|
| 20 GeV/c | 85052425 | 35680145 (42%) | 21691124 (26%) |
| 31 GeV/c | 101075422 | 40514484 (40%) | 24634448 (24%) |
| 40 GeV/c | 110806520 | 43558683 (39%) | 26459404 (24%) |
| 80 GeV/c | 135138286 | 51622224 (38%) | 31222420 (23%) |
| 158 GeV/c | 155861138 | 59798173 (38%) | 35997064 (23%) |
| p_{beam} | p_T | Acceptance | No e^- , e^+ |
| 20 GeV/c | 21685170 (25%) | 13328182 (16%) | 13322191 (16%) |
| 31 GeV/c | 24621331 (24%) | 16132420 (16%) | 16123941 (16%) |
| 40 GeV/c | 26441403 (24%) | 18041012 (16%) | 18031174 (16%) |
| 80 GeV/c | 31187015 (23%) | 22748654 (17%) | 22735220 (17%) |
| 158 GeV/c | 35938321 (23%) | 26807231 (17%) | 26790709 (17%) |

Table 4.4: Track selection statistics for p+p interactions generated in EPOS (pure MC). Number of read pure MC events is given in column “No cuts” of Tab.4.5.

| p_{beam} | No cuts | Beam inter. | Vertex fit | Vertex z pos. |
|-------------------|---------|---------------|---------------|-----------------|
| 20 GeV/c | 4974818 | 4938822 (99%) | 4253812 (86%) | 3839846 (77%) |
| 31 GeV/c | 4979906 | 4904572 (98%) | 4336447 (87%) | 3901071 (78%) |
| 40 GeV/c | 4992151 | 4873970 (98%) | 4391504 (88%) | 3938236 (79%) |
| 80 GeV/c | 4989832 | 4632208 (93%) | 4332518 (87%) | 3861766 (77%) |
| 158 GeV/c | 4984453 | 4192919 (84%) | 4034564 (81%) | 3564212 (72%) |

Table 4.5: Statistics for event cuts for reconstructed Monte Carlo (rec MC) p+p collisions.

- Transverse momentum cut — particles with transverse momentum higher than $p_T = 1.5$ GeV/c were rejected.
- Acceptance cut — EPOS generates data in full (4π) acceptance. The NA61/SHINE detector acceptance was applied to imitate phase-space of real data. In order to do this, a so-called Particle Population Matrix (PPM) was produced which is based on the real data (the procedure is described in the Appendix B).
- e^-e^+ cut — all electrons and positrons, including products of γ decays, were rejected. The cut applied in Monte Carlo data is easier since the exact species (PID) of generated particle is known. Thus, all generated particles, being an electron or a positron, were rejected.

The track selection statistics for pure Monte Carlo are presented in Tab. 4.4.

Reconstructed MC

The purpose of producing reconstructed Monte Carlo, which is pure MC after processing through NA61 reconstruction chain, is to have events and tracks in a quality similar to the quality of the data from real interactions. A set of software applications are used⁴ to simulate NA61 detector hardware. However, not all detectors have their virtual equivalents (e.g. there is no BPD simulation). Because reconstructed MC, with its “contamination”, is more similar to real data, in this dataset event cuts were also applied.

⁴An example is a digitizer which converts generated track (mathematical, continuous object) to the form as it would be registered by TPC pads (a set of discrete points).

| p_{beam} | No cuts | No matched e^-, e^+ | Charged | TPC NPoints |
|-------------------|----------------------|-----------------------|----------------|----------------|
| 20 GeV/c | 10948736 | 10526072 (96%) | 10526072 (96%) | 7871798 (72%) |
| 31 GeV/c | 13359638 | 12783985 (96%) | 12783985 (96%) | 9785090 (73%) |
| 40 GeV/c | 15052226 | 14394791 (96%) | 14394791 (96%) | 11155271 (74%) |
| 80 GeV/c | 19844769 | 19023456 (96%) | 19023456 (96%) | 14947932 (75%) |
| 158 GeV/c | 24332717 | 23451380 (96%) | 23451380 (96%) | 18179568 (75%) |
| p_{beam} | VTPC or GTPC NPoints | B_x and B_y | p_T | Acceptance |
| 20 GeV/c | 7905820 (72%) | 7807048 (71%) | 7800038 (71%) | 7695087 (70%) |
| 31 GeV/c | 9831239 (74%) | 9700449 (73%) | 9692090 (73%) | 9652643 (72%) |
| 40 GeV/c | 11210915 (74%) | 11060081 (73%) | 11050344 (73%) | 11024790 (73%) |
| 80 GeV/c | 15033623 (76%) | 14834453 (75%) | 14817471 (75%) | 14788365 (75%) |
| 158 GeV/c | 18301686 (75%) | 18064134 (74%) | 18038214 (74%) | 17979905 (74%) |

Table 4.6: Track cuts statistics for reconstructed Monte Carlo (rec MC) p+p collisions.

- Beam interaction (S4) cut — beam interaction equivalent to the T2 trigger. Only events with no counts in the S4 counter were accepted.
- Vertex fit — events with well-fitted main vertex were accepted.
- Vertex z position — events with z -axis position of main vertex in a proper range ($-590 < z_{\text{vtx}} < -570$ cm) were accepted.

The event cuts statistics are presented in Tab. 4.5.

The track cuts list for reconstructed Monte Carlo is similar to those for real data, but with some modifications. All cuts given below were applied:

- Charged cut.
- TPC Npoint cut.
- VTPC or GTPC NPoint cut.
- B_x and B_y cuts.
- Transverse momentum cut.
- Acceptance cut — applied additionally to ensure the track phase-space coordinates lays in the NA61 detector acceptance.
- e^-e^+ cut — the identification of the particle is lost during the reconstruction chain, thus matching procedure was performed on reconstructed particles to find their corresponding electrons and positrons from dataset before the reconstruction. The matching efficiency was calculated to be $98 \pm 1\%$.

The track cuts statistics for reconstructed Monte Carlo are presented in Tab. 4.6.

4.2 Results of inclusive analysis

In this section the results from inclusive analysis of two-particle correlations in pseudo-rapidity and azimuthal angle in inelastic p+p collisions at beam momenta 20, 31, 40, 80, and 158 GeV/c, from data taken in 2009 year, are presented. The events and particles were

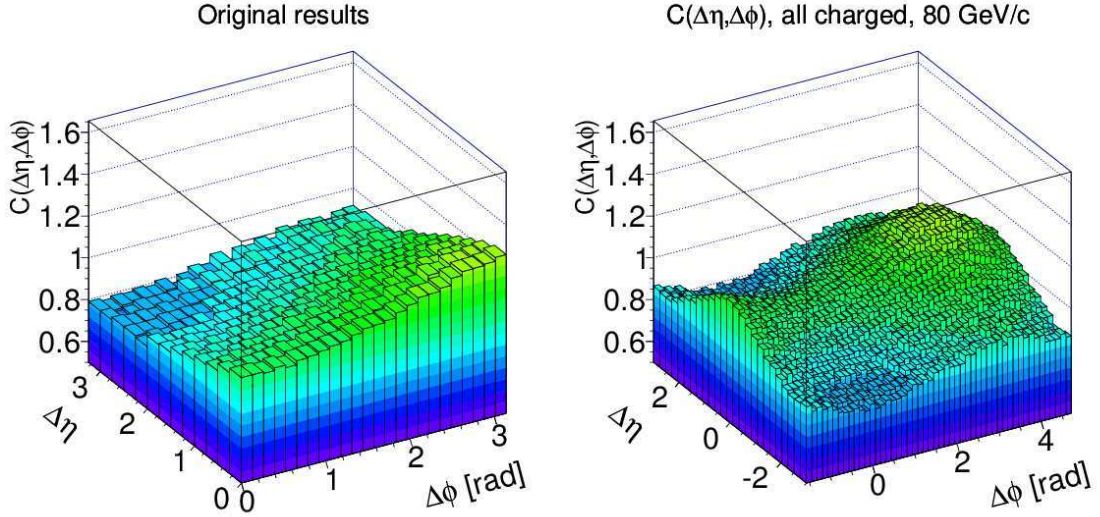


Figure 4.2: Example of mirror reflection of final correlation function. Left panel: original histogram after correlation function calculation. Right panel: effect of mirroring against $(\Delta\eta, \Delta\phi) = (0, 0)$ point and plotting in asymmetrical $\Delta\phi$ range: $[-\frac{\pi}{2}, \frac{3}{2}\pi)$. Example for uncorrected correlation function in p+p collisions at beam momentum 80 GeV/c.

chosen according to the selection cuts described in Sec. 4.1. The definition of correlation function $C(\Delta\eta, \Delta\phi)$ was described in Sec. 2.1.2.

Due to limited statistics, three procedures were applied to make the results easier to read:

- During calculation of $\Delta\phi$ difference (see formula 2.5, right) folding was applied: in case the difference was $\Delta\phi > \pi$, it was reflected: $\Delta\phi = 2\pi - \Delta\phi$.
- Originally, the range of pseudorapidity difference was $\Delta\eta \in [0, 6)$. However, the statistics above $\Delta\eta > 3$ was too low to distinguish particular physical structures from bin-by-bin statistical fluctuations (especially at low beam momenta). Thus, $\Delta\eta$ range of interest was limited to $\Delta\eta \in [0, 3)$. Note, that normalization factors of signal and mixed distributions ($N_{\text{pairs}}^{\text{signal}}$ and $N_{\text{pairs}}^{\text{background}}$ in Eq. 2.6) were calculated inside this narrowed range.
- To minimize statistical fluctuations between bins at the two lowest beam momenta – 20 GeV/c and 31 GeV/c – the wider binning was used for these cases. A net of 12x12 bins was used there, instead of 24x24 as for higher beam momenta.
- All correlation function histograms are presented in the ranges $\Delta\eta \in (-3, 3)$ and $\Delta\phi \in [-\frac{\pi}{2}, \frac{3}{2}\pi)$. The original results are mirrored against $(\Delta\eta, \Delta\phi) = (0, 0)$ point to make the structures more readable and comparable with the results from other experiments. The example of mirror reflection is presented in Fig. 4.2.

The next section presents the results on two-particle correlations not corrected for the detector effects. The correction method is presented in Sec. 4.2.2. Then, the corrected results are shown in Sec. 4.2.3.

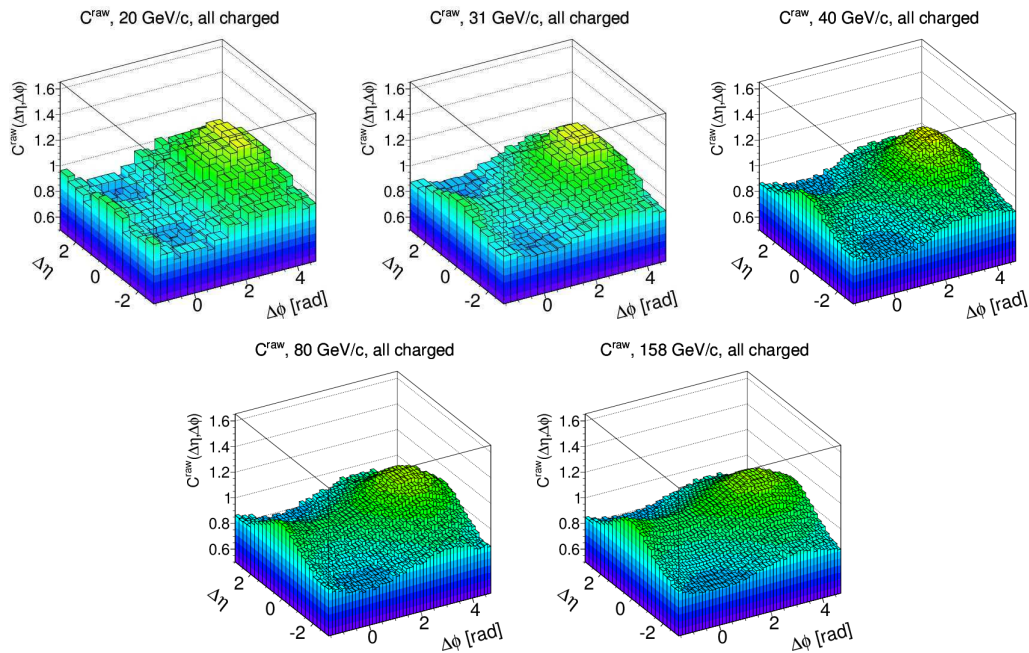


Figure 4.3: Uncorrected results on $\Delta\eta\Delta\phi$ correlations for all charged particle pairs.

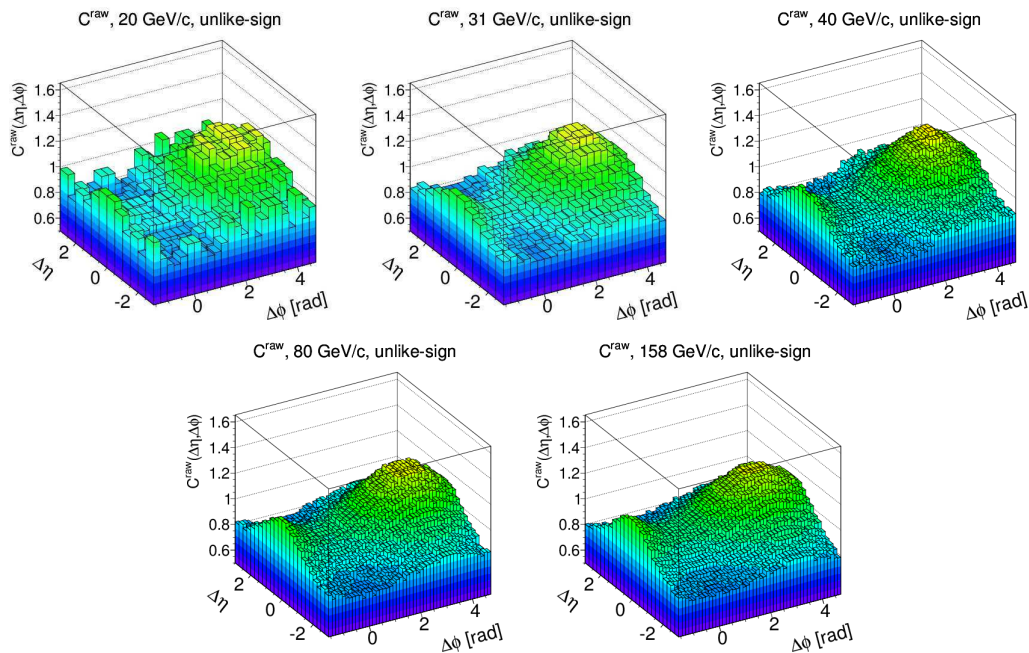
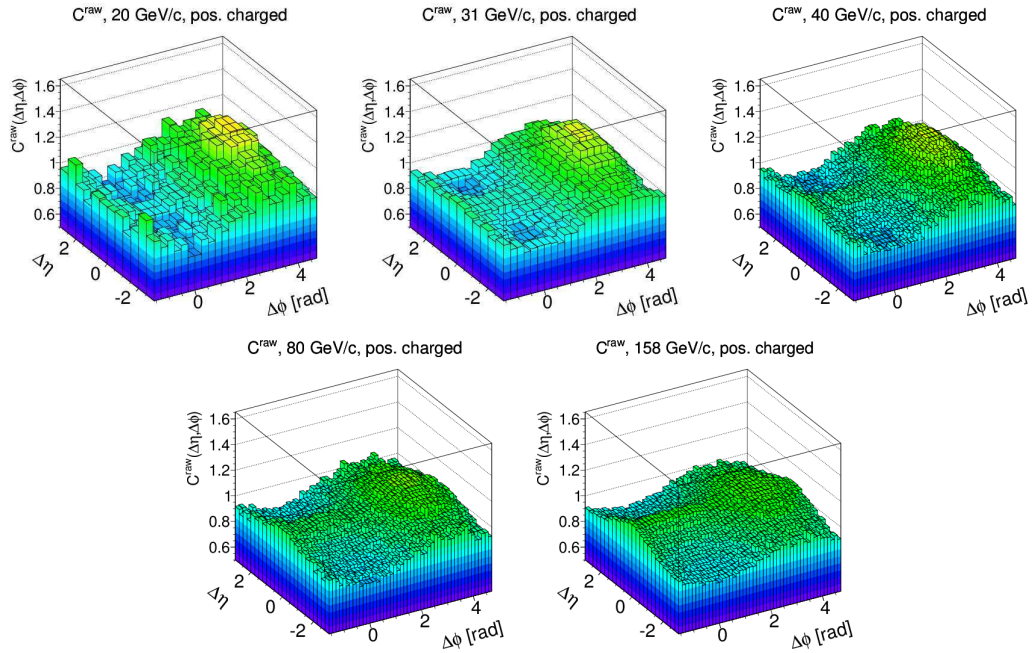
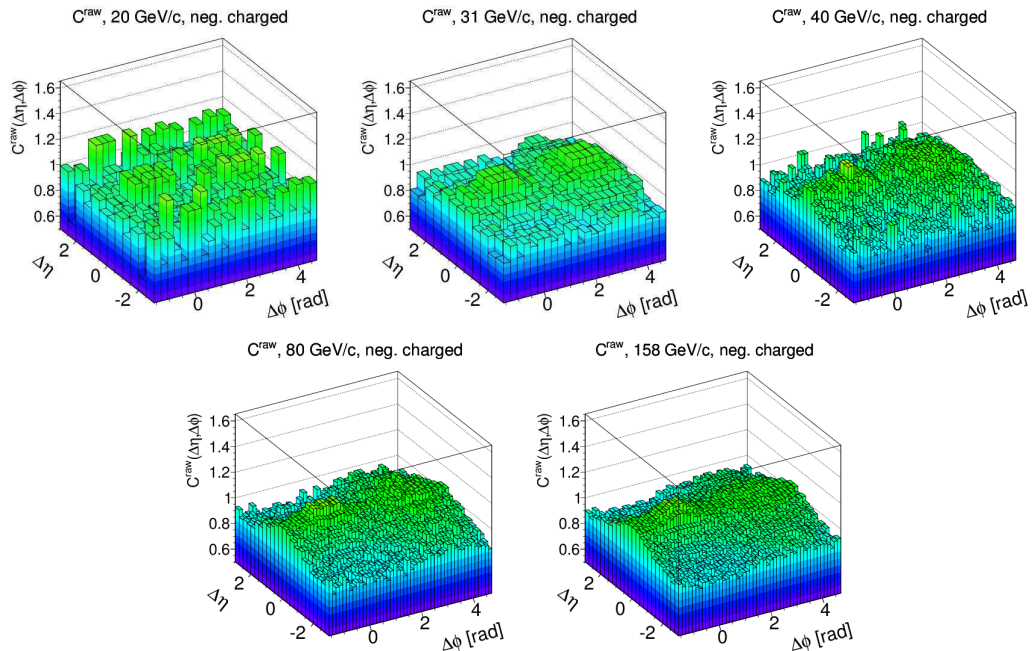


Figure 4.4: Uncorrected results on $\Delta\eta\Delta\phi$ correlations for unlike-sign particle pairs.

4.2.1 Uncorrected results

Figures 4.3, 4.4, 4.5 and 4.6 present uncorrected $C^{\text{raw}}(\Delta\eta, \Delta\phi)$ results for various energies and charge combinations.

Figure 4.5: Uncorrected results on $\Delta\eta\Delta\phi$ correlations for positively charged particle pairs.Figure 4.6: Uncorrected results on $\Delta\eta\Delta\phi$ correlations for negatively charged particle pairs.

4.2.2 Detector effects

In this subsection detector effects analysis is described and presented. Firstly, the method of corrections calculation is discussed, then the magnitudes of corrections for all charge combinations and beam momenta are shown.

Correction method

The NA61/SHINE detector and its reconstruction framework, as all real (non-ideal) pieces of hardware and software, have their limits and flaws. They manifest themselves in trigger bias and reconstruction inefficiencies. Here are some examples.

The S4 counter, put in an anti-coincidence in the trigger logic (see Sec. 3.2.1) rejects an event when a particle hits it. This solution works well for recognition of events when the beam particle misses the target. However, in minority of cases a particle produced in a “good” event may hit S4 (wrong-side track⁵ or a product of $V0$ decay⁶). This results in rejecting “good” events and such effect is called “trigger bias”.

During reconstruction process (described in Sec. 3.3), the fitting of points to create a track is done. During fitting, the points may be wrongly connected to each other and create two separate tracks instead of a proper one (split tracks) or oppositely, two neighboring tracks may be interpreted as one track (merged tracks). These reconstruction inefficiency effects are results of non-ideal hardware setup (e.g. limited resolution of TPC pads).

The analyzed two-particle correlations can be corrected for these effects. This is achieved by doing a similar analysis of correlation function on two datasets of Monte Carlo data. As mentioned in Sec. 4.1.2, the first dataset, not processed by the NA61 reconstruction process (pure MC), is treated as “ideal” data, while the second (rec MC) is processed through reconstruction chain which implements the same effects as in real data. After processing both datasets separately, a correction factor $\text{Corr}(\Delta\eta, \Delta\phi)$ is calculated as a ratio:

$$\text{Corr}(\Delta\eta, \Delta\phi) = \frac{C^{\text{pure}}(\Delta\eta, \Delta\phi)}{C^{\text{rec}}(\Delta\eta, \Delta\phi)}, \quad (4.1)$$

where C^{pure} is the correlation function $C(\Delta\eta, \Delta\phi)$ obtained for generated (pure MC) events and C^{rec} is the correlation function $C(\Delta\eta, \Delta\phi)$ obtained for reconstructed (rec MC) events. The correction factors are presented in the next paragraph.

Uncorrected results (C^{raw}) are then corrected using correction factors simply by calculating bin-by-bin:

$$C(\Delta\eta, \Delta\phi) = C^{\text{raw}}(\Delta\eta, \Delta\phi) \cdot \text{Corr}(\Delta\eta, \Delta\phi). \quad (4.2)$$

The corrected results are presented in Sec. 4.2.3.

Correction factors

The correction factors were calculated using Eq. 4.1. The results of $\frac{C^{\text{pure}}(\Delta\eta, \Delta\phi)}{C^{\text{rec}}(\Delta\eta, \Delta\phi)}$ for all charged, unlike-sign, positively, and negatively charged pairs are presented in Figs. 4.7, 4.8, 4.9, and 4.10, respectively.

⁵A track for which $q \cdot p_x$ is smaller than zero; right-side track is the track for which $q \cdot p_x$ is higher than zero (q is the electric charge of the particle).

⁶ $V0$ is a characteristic shape of two oppositely charged tracks left by products of a weak decay of a neutral particle.

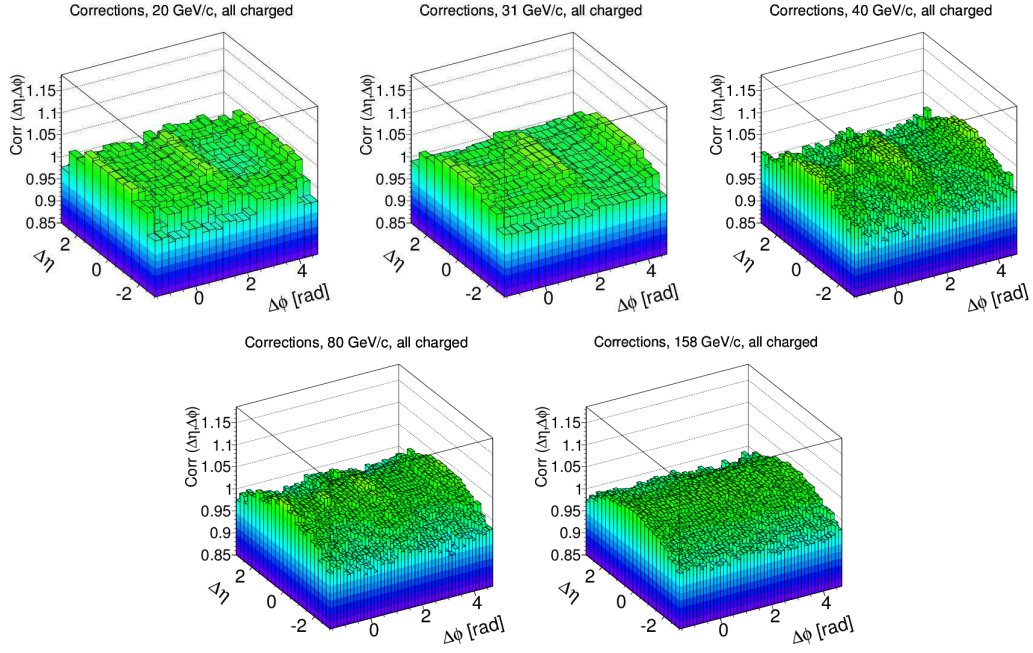


Figure 4.7: Correction factors for all charged particle pairs.

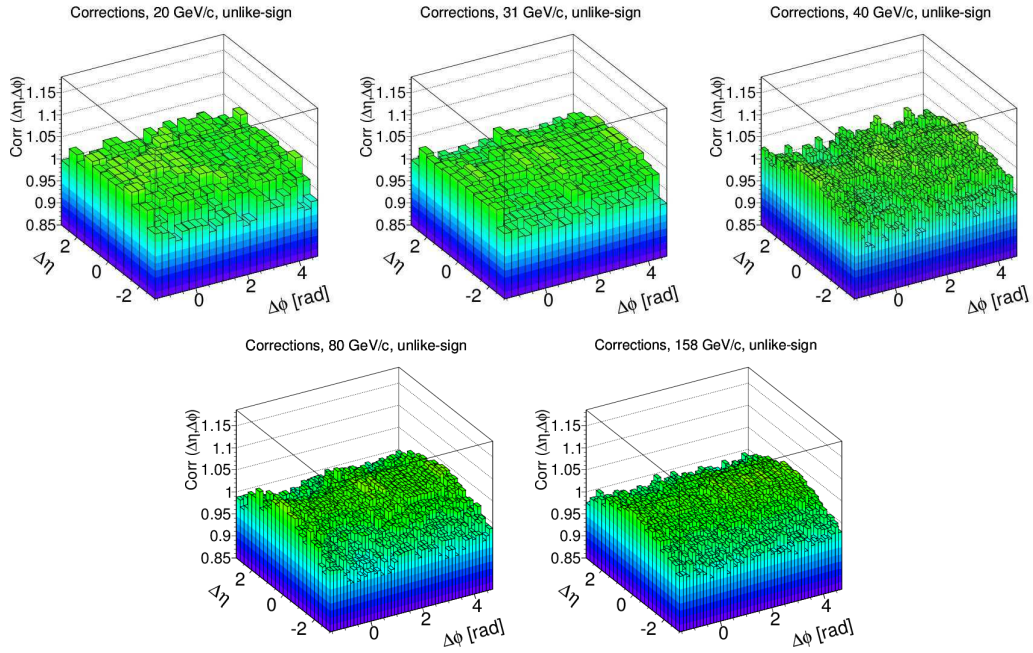


Figure 4.8: Correction factors for unlike-sign particle pairs.

The values of detector effects correction factors are below 10% with respect to unity. The distributions present a general structure of one-dimensional hill in $\Delta\eta$. The effects magnitude (Corr) is typically higher than unity for $|\Delta\eta| < 2$ (more contribution from pure MC than from rec MC) and lower than unity outside this range (less contribution from pure MC than from rec MC). Additionally, enhancements at $\Delta\phi \approx \pi/2$ for $|\Delta\eta| < 2$ at lower beam momenta can be noticed. They are probably large bin-by-bin fluctuations. The largest fluctuations are for lower beam momenta and for like-sign pair distributions.

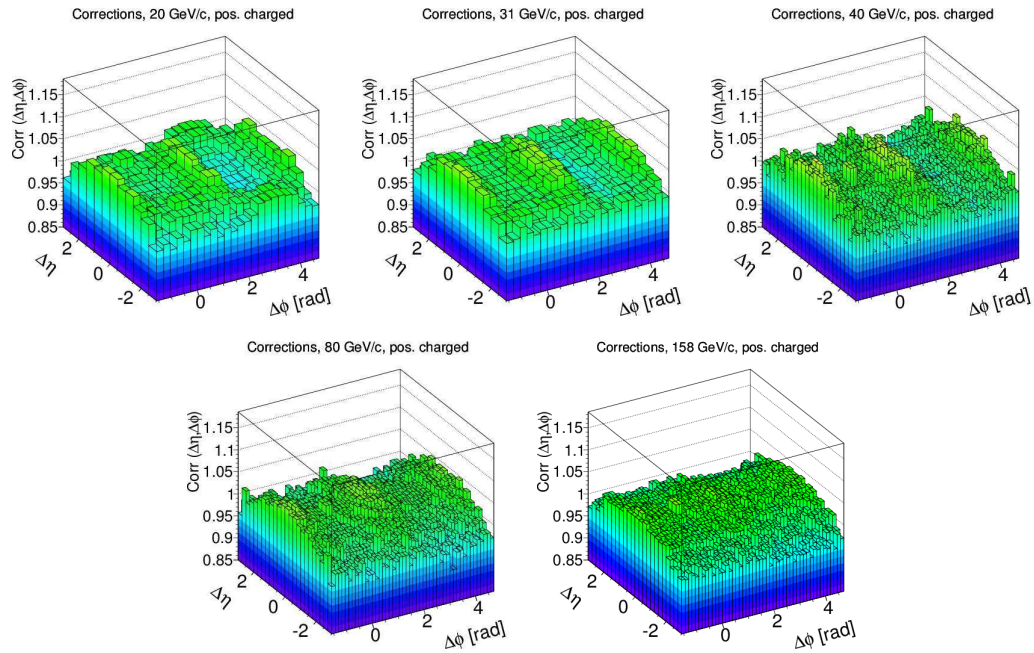


Figure 4.9: Correction factors for positively charged particle pairs.

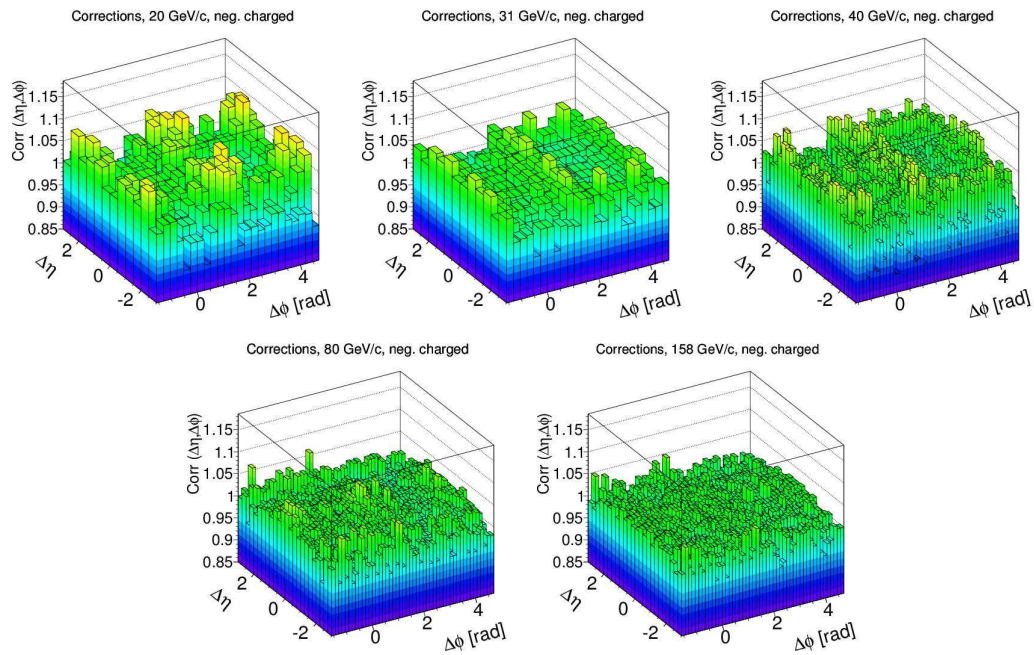


Figure 4.10: Correction factors for negatively charged particle pairs.

4.2.3 Corrected results

Uncorrected results, presented in Sec. 4.2.1, were corrected using correction factors presented in the previous section, according to Eq. 4.2. Figures 4.11, 4.12, 4.13, and 4.14 show final results on two-particle correlation function $C(\Delta\eta, \Delta\phi)$ for all charged pairs, unlike-sign pairs, positively charged pairs, and negatively charged pairs, respectively.

Two-particle correlations in pseudorapidity and azimuthal angle at the SPS energies show following structures:

- A maximum at $(\Delta\eta, \Delta\phi) \approx (0, \pi)$. The most prominent in all charged and unlike-sign pairs and significantly weaker in like-sign correlations. The most probable explanation is the contribution from resonance decays. A weaker resonance maximum in positively charged pairs can be attributed to e.g. Δ^{++} resonance decay. No such a structure in negatively charged pairs can be connected with a fact that there are almost no double negative resonances.
- $-\cos(\Delta\phi)$ modulation appearing as a one-dimensional minimum near $\Delta\phi = 0$ and maximum near $\Delta\phi = \pi$. It is visible in all charge combinations, but it is stronger in all charged and unlike-sign pairs, weaker but still visible in positively charged and barely noticeable for negatively charged pairs. The modulation is roughly independent of beam momentum. Such a structure is probably due to momentum conservation.
- A longitudinal gaussian-like enhancement around $\Delta\eta = 0$. Clearly visible for all charged and unlike-sign pairs, however significantly weaker, but still noticeable in like-sign correlations. It may be connected to fragmentation of strings or flux-tube. A discussion of the latter one is given in Sec. 4.4.2.
- A hill around $(\Delta\eta, \Delta\phi) = (0, 0)$ in like-sign correlations. For positively charged pairs it grows with increasing beam momentum, but it is independent of it for negatively charged pairs. Since the products of γ decays were rejected during the analysis, the hill is probably caused by Bose-Einstein statistics.
- Clearly, there is no jet-like peak at $(\Delta\eta, \Delta\phi) = (0, 0)$. The structure does not appear because the analysis was done with the restriction on transverse momentum of a particle $p_T < 1.5$ GeV/c. However, without such cut applied, the distributions look very similar (see details in Sec. 4.5). This indicates that, at SPS energies, hard scattering effects are absent or below the background threshold.

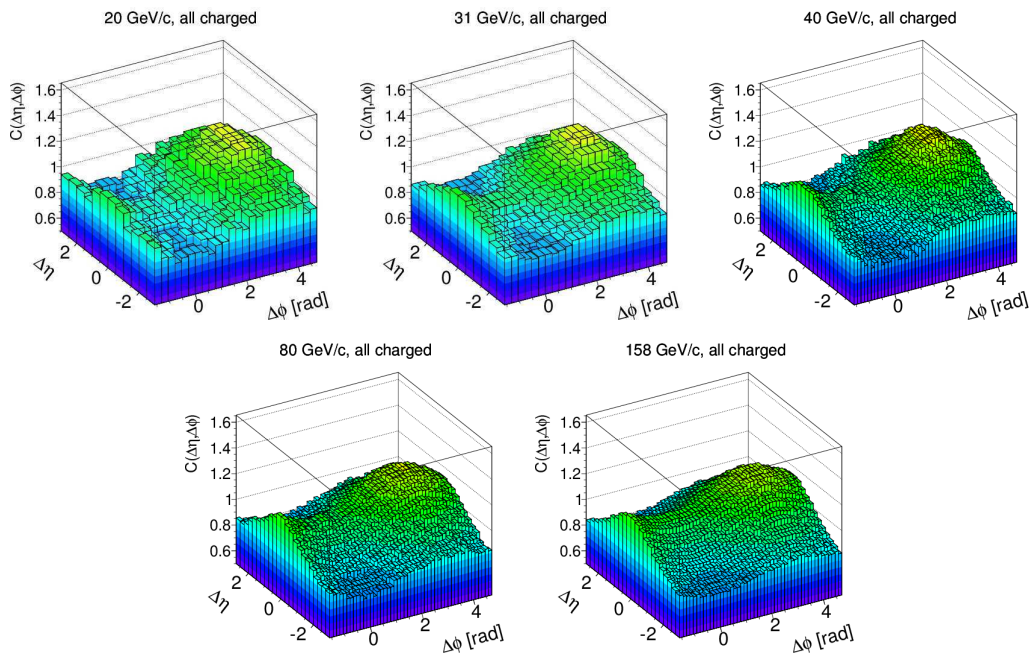


Figure 4.11: Final results on two-particle correlation function $C(\Delta\eta, \Delta\phi)$ in inelastic p+p collisions, corrected for detector effects. All charged pairs.

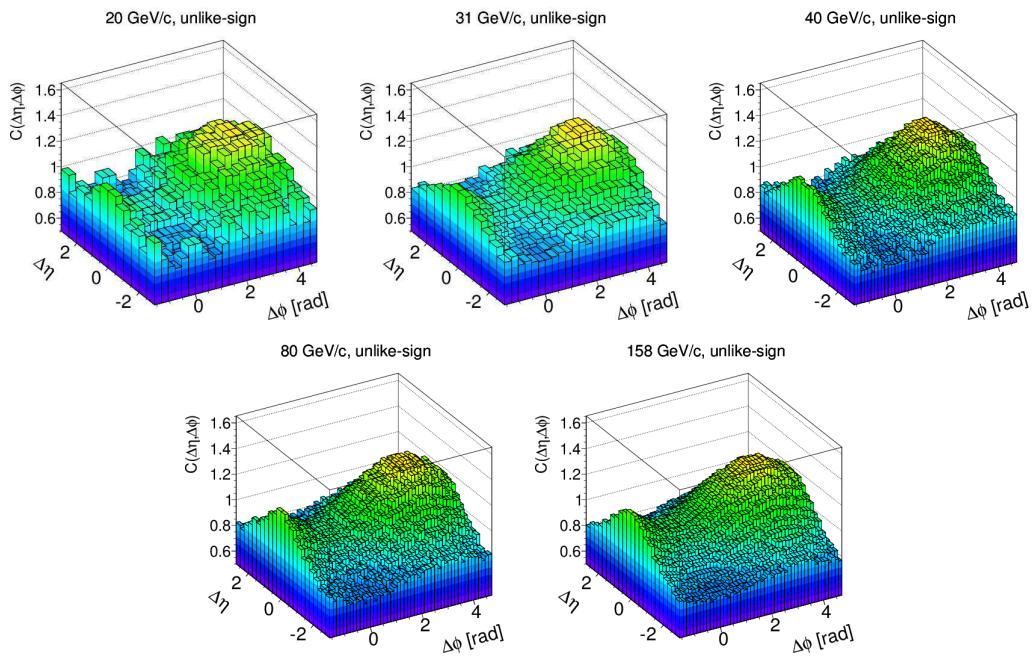


Figure 4.12: Final results on two-particle correlation function $C(\Delta\eta, \Delta\phi)$ in inelastic p+p collisions, corrected for detector effects. Unlike-sign pairs.

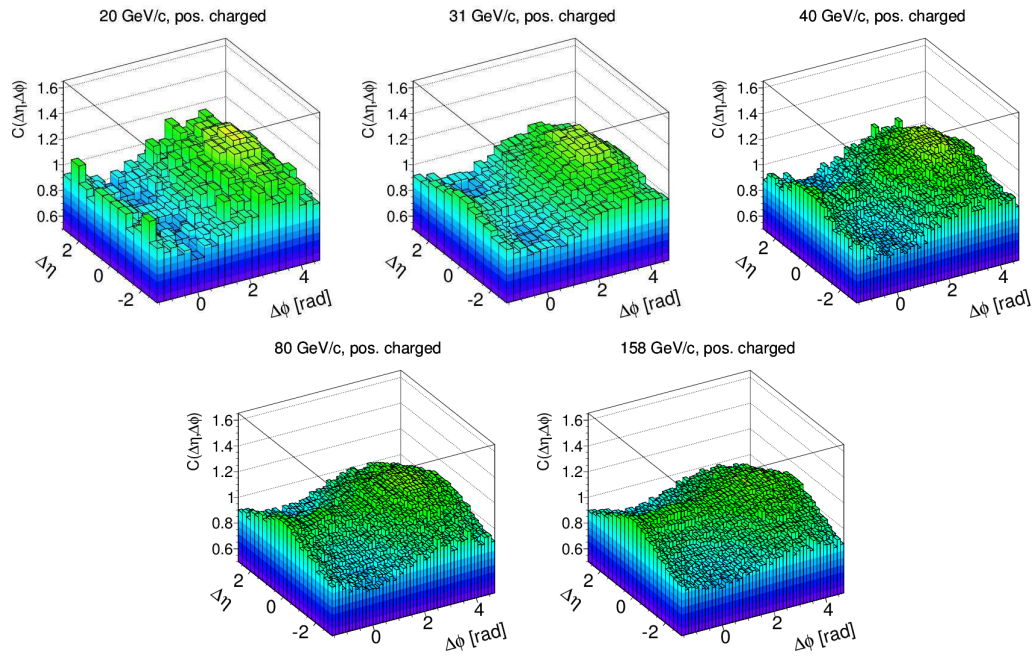


Figure 4.13: Final results on two-particle correlation function $C(\Delta\eta, \Delta\phi)$ in inelastic p+p collisions, corrected for detector effects. Positively charged pairs.

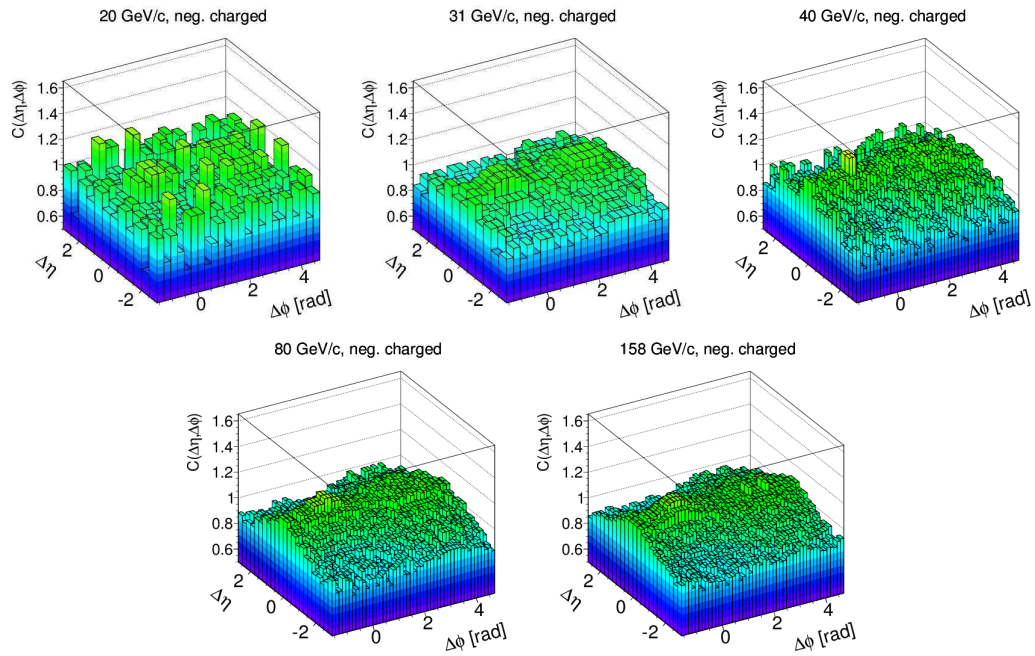


Figure 4.14: Final results on two-particle correlation function $C(\Delta\eta, \Delta\phi)$ in inelastic p+p collisions, corrected for detector effects. Negatively charged pairs.

4.3 Uncertainties

In this section statistical and systematic uncertainties are discussed. The statistical uncertainties formulas are evaluated and their results are shown in Sec. 4.3.1. The systematic uncertainties estimation and their results are shown in Sec. 4.3.2.

4.3.1 Statistical uncertainties

The statistical uncertainties of two-particle correlation function were calculated bin-by-bin for each final distribution of corrected $C(\Delta\eta, \Delta\phi)$ function (for each beam momentum and each charge pair combination).

The ROOT framework offers an automatic statistical uncertainty calculation using `Sumw2()` function. However, ROOT assumes that all data taken to calculations are independent which does not apply to detector effects part of statistical uncertainties of two-particle correlations. Indeed, both numerator and denominator in Eq. 4.1 have the same origin, and therefore they are not independent. Thus, the calculations of statistical uncertainties in this part cannot be executed automatically in ROOT. A manual method of calculating statistical uncertainties was developed as described below.

The corrected correlation function C is given by Eq. 4.2. For simplicity $(\Delta\eta, \Delta\phi)$ part is omitted:

$$C = \text{Corr} \cdot C^{\text{raw}}. \quad (4.3)$$

The statistical uncertainty of the correlation function is:

$$\sigma(C) = \sqrt{[\text{Corr} \cdot \sigma(C^{\text{raw}})]^2 + [C^{\text{raw}} \cdot \sigma(\text{Corr})]^2}, \quad (4.4)$$

where $\sigma(C^{\text{raw}})$ and $\sigma(\text{Corr})$ are the statistical uncertainties of the raw correlation distribution and correction distribution, respectively.

Since the results in `Corr` and in C^{raw} origin from different datasets (`Corr` from both pure MC and rec MC and C^{raw} from real data), only statistical fluctuations of `Corr` and C^{raw} are uncorrelated. The values of C , `Corr`, and C^{raw} as well as $\sigma(C)$, $\sigma(C^{\text{raw}})$, and $\sigma(\text{Corr})$ are calculated for each $(\Delta\eta, \Delta\phi)$ bin.

The uncorrected correlation function C^{raw} is calculated as:

$$\begin{aligned} C^{\text{raw}} &= \frac{N_B}{N_S} \cdot \frac{S}{B}; \\ S &= \frac{n_S}{\Delta\eta\Delta\phi}, \quad B = \frac{n_B}{\Delta\eta\Delta\phi}; \\ C^{\text{raw}} &= \frac{N_B}{N_S} \cdot \frac{n_S}{n_B}; \end{aligned}$$

where n_S, n_B are the number of pairs in a given $(\Delta\eta, \Delta\phi)$ bin and N_S, N_B are total number of pairs in signal and mixed distributions, respectively.

Assuming $n_S \ll N_S$ and $n_B \ll N_B$, the statistical uncertainty of C^{raw} is:

$$\sigma(C^{\text{raw}}) = \frac{N_B}{N_S} \frac{n_S}{n_B} \left[\left(\frac{\sigma(n_S)}{n_S} \right)^2 + \left(\frac{\sigma(n_B)}{n_B} \right)^2 \right]^{\frac{1}{2}}; \quad (4.5)$$

$$\sigma(n_S) = \sqrt{n_S}, \quad \sigma(n_B) = \sqrt{n_B}.$$

The correction factor Corr is calculated as:

$$\text{Corr} = \frac{C^P}{C^R}; \quad (4.6)$$

$$C^P = \frac{N_B^P n_S^P}{N_S^P n_B^P}, \quad C^R = \frac{N_B^R n_S^R}{N_S^R n_B^R},$$

where C^P is the correlation function in pure Monte Carlo and C^R is the correlation function in reconstructed Monte Carlo.

The transformation of Eq. 4.6 leads to:

$$\text{Corr} = \frac{N_B^P N_S^R}{N_B^R N_S^P} \cdot \frac{n_S^P n_B^R}{n_B^P n_S^R} = \alpha \cdot \frac{n_S^P n_B^R}{n_B^P n_S^R}. \quad (4.7)$$

Assuming $n_S^{P,R} \ll N_S^{P,R}$ and $n_B^{P,R} \ll N_B^{P,R}$, the statistical uncertainty for correction factor $\sigma(\text{Corr})$ is:

$$\sigma(\text{Corr}) = \alpha \cdot \sqrt{\left(\frac{n_B^R}{n_B^P} \cdot \sigma\left(\frac{n_S^P}{n_S^R}\right)\right)^2 + \left(\frac{n_S^P}{n_S^R} \cdot \sigma\left(\frac{n_B^R}{n_B^P}\right)\right)^2}. \quad (4.8)$$

The ratios $\frac{n_S^P}{n_S^R}$ and $\frac{n_B^R}{n_B^P}$ may be expressed as:

$$\frac{n_S^P}{n_S^R} = \frac{n_S^P}{n_S^P + n_S^F} = \frac{1}{1 + n_S^F/n_S^P}, \quad \frac{n_B^R}{n_B^P} = \frac{n_B^P + n_B^F}{n_B^P} = 1 + \frac{n_B^F}{n_B^P}, \quad (4.9)$$

where $n_S^F = n_S^R - n_S^P$ and $n_B^F = n_B^R - n_B^P$ are the loss or gain of pairs due to all possible biases. Hence:

$$\sigma\left(\frac{n_S^P}{n_S^R}\right) = \sigma\left(\frac{1}{1 + n_S^F/n_S^P}\right), \quad \sigma\left(\frac{n_B^R}{n_B^P}\right) = \sigma\left(1 + \frac{n_B^F}{n_B^P}\right). \quad (4.10)$$

Assuming $n_S^F \ll n_S^P$ and $n_B^F \ll n_B^P$:

$$\sigma\left(\frac{n_S^P}{n_S^R}\right) = \frac{\sigma(n_S^F)}{n_S^P} = \frac{\sqrt{|n_S^F|}}{n_S^P}, \quad \sigma\left(\frac{n_B^R}{n_B^P}\right) = \frac{\sigma(n_B^F)}{n_B^P} = \frac{\sqrt{|n_B^F|}}{n_B^P}. \quad (4.11)$$

The final statistical uncertainty for the correction factor $\sigma(\text{Corr})$ is:

$$\sigma(\text{Corr}) = \alpha \cdot \sqrt{\left(\frac{n_B^R}{n_B^P} \frac{\sqrt{|n_S^F|}}{n_S^P}\right)^2 + \left(\frac{n_S^P}{n_S^R} \frac{\sqrt{|n_B^F|}}{n_B^P}\right)^2}. \quad (4.12)$$

The statistical uncertainties for all charge combinations and beam momenta are presented in Figs. 4.15, 4.16, 4.17, and 4.18.

All statistical uncertainty distributions suffer lack of statistics which appears as red bands at the borders of pseudorapidity range. The conclusions below will be made with exclusion of such bands. The upper limit of statistical uncertainties is at the level of 5% (with respect to unity) with exception of negatively charged pairs in collisions at the lowest beam momenta where they reach 20%. The lowest uncertainties are in the pseudorapidity range $|\Delta\eta| < 2$, especially in the regions around $(\Delta\eta, \Delta\phi) = (0, 0)$ and $(0, \pi)$. At higher $\Delta\eta$ strong statistical fluctuations occur which give clearly higher values of uncertainties.

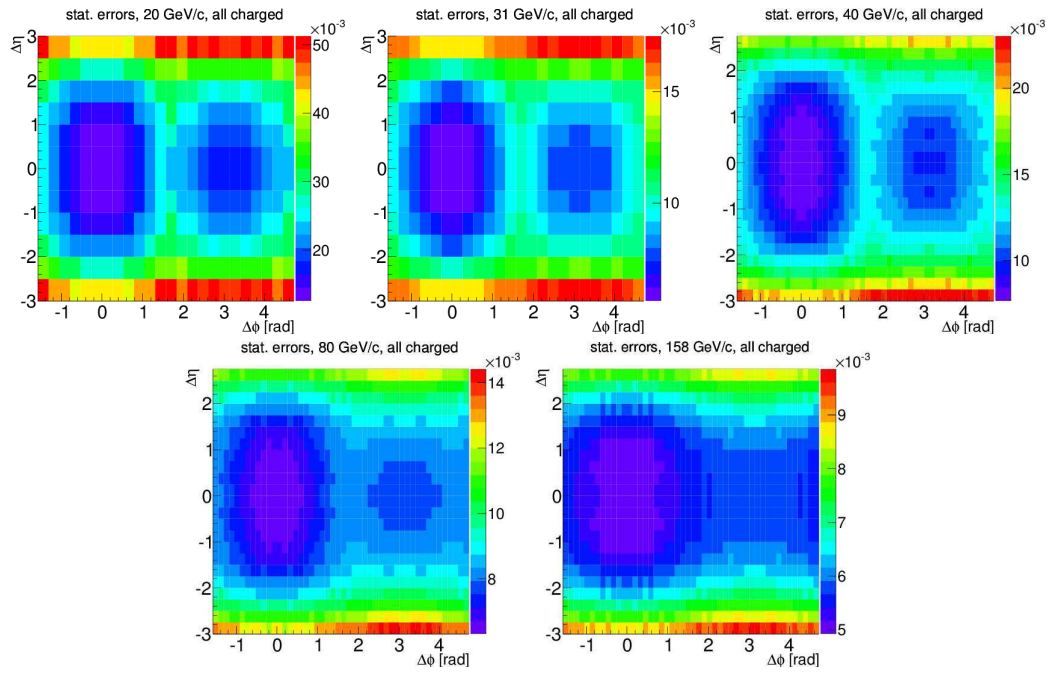


Figure 4.15: Statistical uncertainties of corrected correlation functions. All charged pairs.

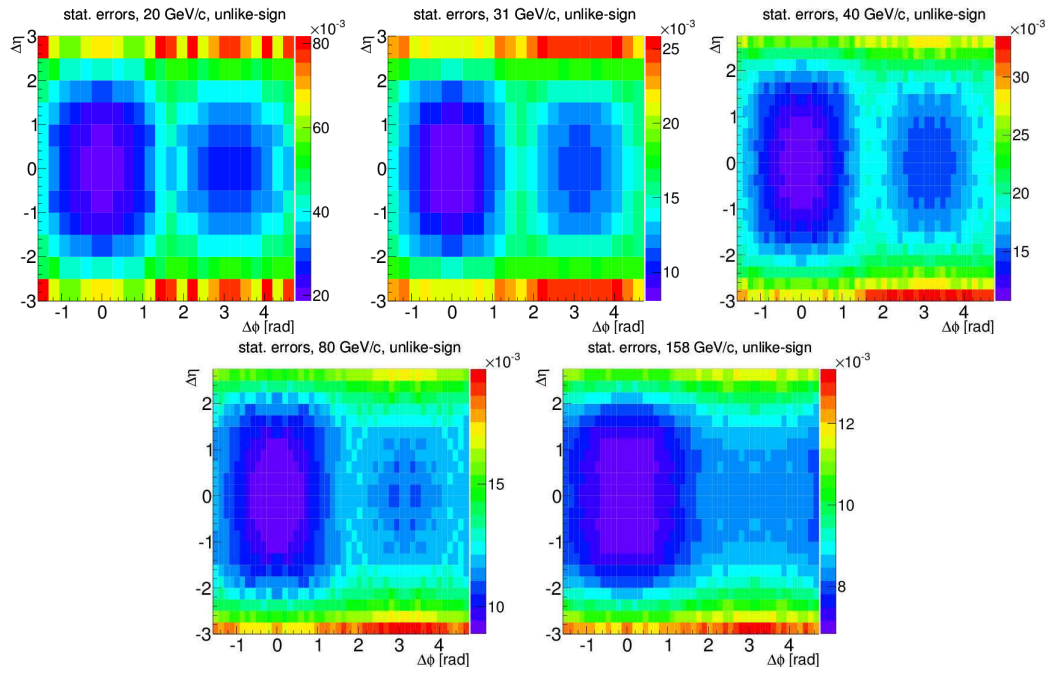


Figure 4.16: Statistical uncertainties of corrected correlation functions. Unlike-sign pairs.

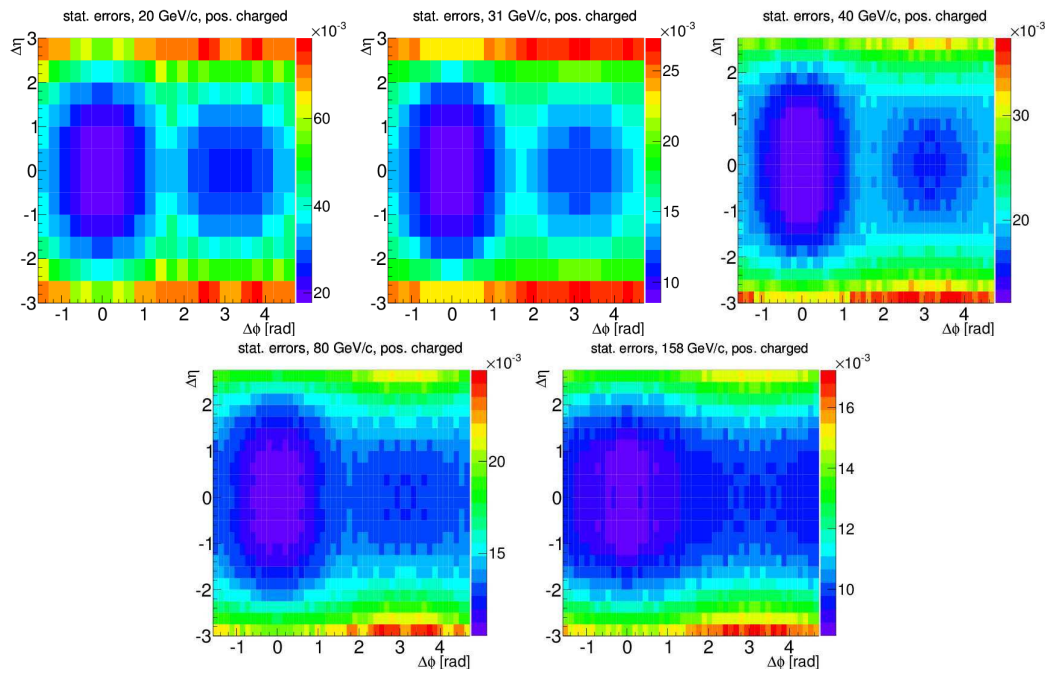


Figure 4.17: Statistical uncertainties of corrected correlation functions. Positively charged pairs.

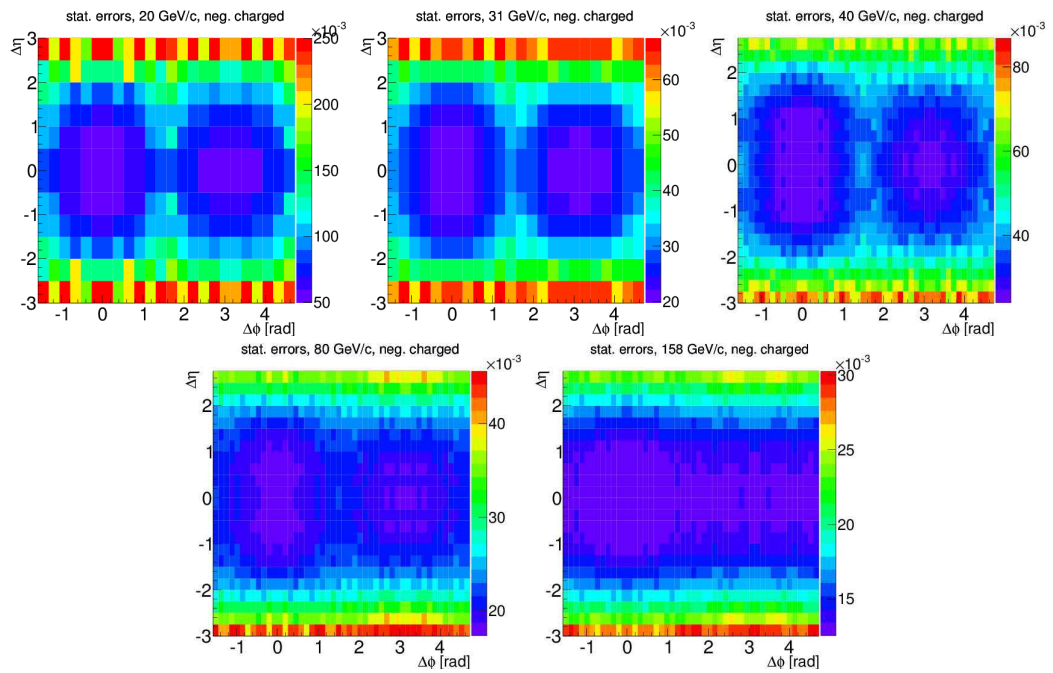


Figure 4.18: Statistical uncertainties of corrected correlation functions. Negatively charged pairs.

4.3.2 Systematic uncertainties

In order to estimate systematic uncertainties, that come from choosing the actual set of cuts⁷, the full analysis process was repeated under two different sets of cuts (so-called “loose” and “tight” cuts). The cut values are presented in Tab. 4.7.

| Event cuts | | | |
|--------------------------------|---------------|----------------------|----------------------|
| | Loose | Standard | Tight |
| Event with interaction trigger | applied | | |
| BPD cuts | applied | | |
| No off-time beam particles | disabled | $< \pm 1\mu\text{s}$ | $< \pm 5\mu\text{s}$ |
| Vertex fit | applied | | |
| Vertex z position | ± 11 cm | ± 10 cm | ± 7 cm |
| No elastic events | applied | | |
| Track cuts | | | |
| Charge $\neq 0$ | applied | | |
| Total TPC points | ≥ 10 | ≥ 30 | |
| VTPC (GTPC) points | $> 10(5)$ | $\geq 15(5)$ | $\geq 30(6)$ |
| $ B_x $ | ≤ 5 cm | ≤ 4 cm | ≤ 1 cm |
| $ B_y $ | ≤ 2.5 cm | ≤ 2 cm | ≤ 0.5 cm |
| p_T cut | applied | | |
| e^-e^+ cut | applied | | |

Table 4.7: Standard, loose, and tight cuts definitions. See Sec. 4.1 for details.

The procedure of systematic uncertainties estimation was as follows. The full analysis procedure was performed for both tight and loose cuts. This involved calculation of detector effects corrections and applying them to raw correlation functions (see corrected results on top rows of Figs. 4.19 and 4.20). Then, bin-by-bin, tight set of cuts results were subtracted from the results for loose cuts. The distributions of *loose* – *tight* differences were drawn and are presented in bottom left panels of Figs. 4.19 and 4.20. Due to lower statistics in higher $\Delta\eta$, the full pseudorapidity difference range was splitted into two subranges: $\Delta\eta \leq 2$ and $\Delta\eta > 2$. The *loose* – *tight* differences were drawn for those two subranges as well (see bottom middle and bottom right panels in Figs. 4.19 and 4.20).

The *loose* – *tight* differences have approximately gaussian distributions with mean values around zero. The systematic error of each distribution was calculated as the standard deviation of the mean⁸. The results of such calculations for three beam momenta: 20, 40, and 158 GeV/c, for all charge combinations, and three ranges of $\Delta\eta$ are presented in Tab. 4.8.

The systematic uncertainties of the analysis are below 1% (with respect to unity) with exception of correlations for high $\Delta\eta$ range at low beam momenta where they are about 5%.

⁷Called here “standard”; see Sec. 4.1 for details.

⁸RMS value divided by the square root of the number of entries in the histogram.

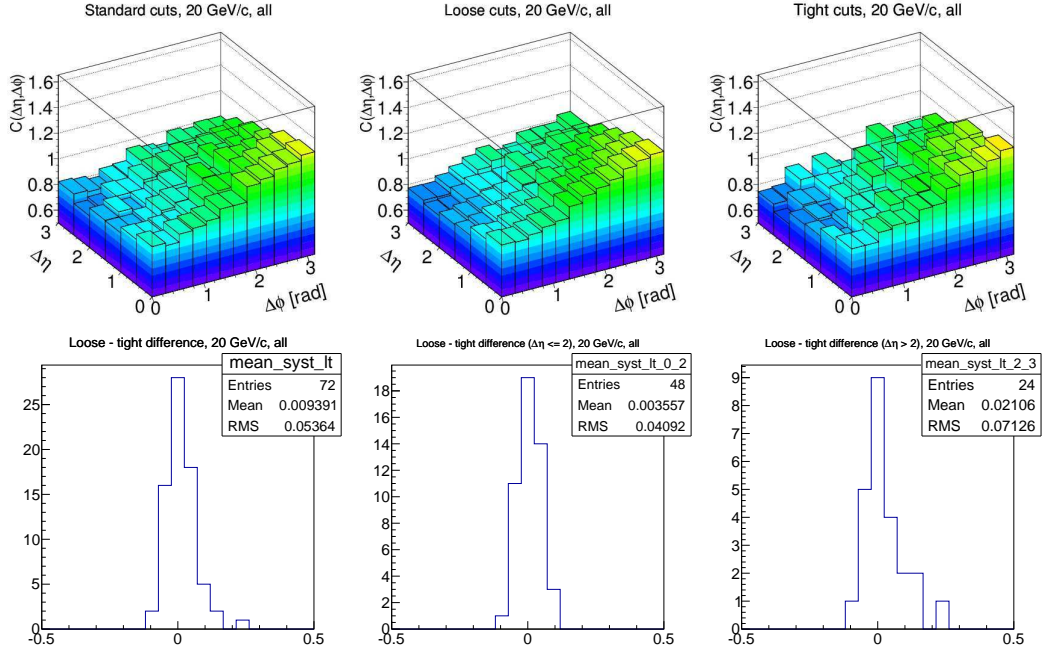


Figure 4.19: Estimation of systematic uncertainty – the example for p+p at 20 GeV/c. Top row presents corrected correlation functions for standard set of cuts (left), loose set of cuts (middle), and tight set of cuts (right). Differences of *loose* – *tight* are presented in the bottom row for full $\Delta\eta$ range (left) as well as for two subranges: $\Delta\eta \leq 2$ (middle) and $\Delta\eta > 2$ (right). Correlation function results are presented for original, unmirrored range.

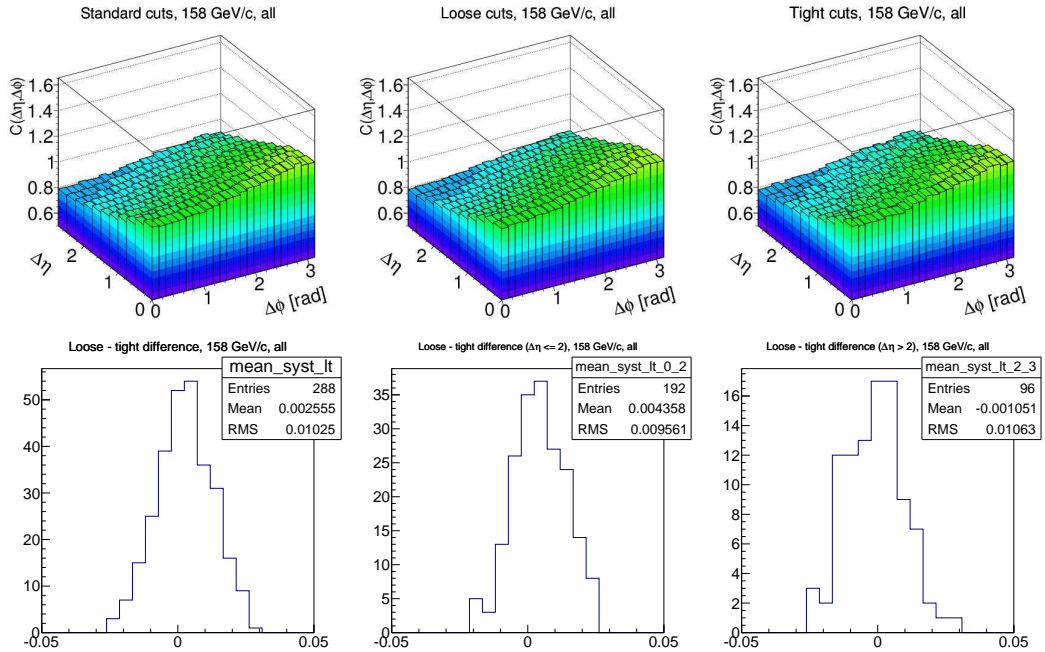


Figure 4.20: Estimation of systematic uncertainty – the example for p+p at 158 GeV/c. Top row presents corrected correlation functions for standard set of cuts (left), loose set of cuts (middle), and tight set of cuts (right). Differences of *loose* – *tight* are presented in the bottom row for full $\Delta\eta$ range (left) as well as for two subranges: $\Delta\eta \leq 2$ (middle) and $\Delta\eta > 2$ (right). Correlation function results are presented for original, unmirrored range.

| Energy | All charged | Unlike-sign | Pos. charged | Neg. charged |
|----------------------------|----------------------------|----------------------------|----------------------------|--------------------------|
| 20 GeV/c | $9.4(6.3) \cdot 10^{-3}$ | $5.3(9.7) \cdot 10^{-3}$ | $13(11) \cdot 10^{-3}$ | $-2(25) \cdot 10^{-3}$ |
| 40 GeV/c | $1.1(1.6) \cdot 10^{-3}$ | $1.5(2.3) \cdot 10^{-3}$ | $-0.1(2.5) \cdot 10^{-3}$ | $0.2(4.8) \cdot 10^{-3}$ |
| 158 GeV/c | $2.55(0.60) \cdot 10^{-3}$ | $2.73(0.84) \cdot 10^{-3}$ | $1.60(0.96) \cdot 10^{-3}$ | $4.9(1.3) \cdot 10^{-3}$ |
| $0 \leq \Delta\eta < 2$ | | | | |
| 20 GeV/c | $3.6(5.9) \cdot 10^{-3}$ | $-0.1(10) \cdot 10^{-3}$ | $-3.4(7.1) \cdot 10^{-3}$ | $3(27) \cdot 10^{-3}$ |
| 40 GeV/c | $2.4(1.7) \cdot 10^{-3}$ | $0.8(2.4) \cdot 10^{-3}$ | $3.6(2.6) \cdot 10^{-3}$ | $2.9(4.3) \cdot 10^{-3}$ |
| 158 GeV/c | $4.36(0.68) \cdot 10^{-3}$ | $5.10(0.96) \cdot 10^{-3}$ | $3.4(1.1) \cdot 10^{-3}$ | $5.2(1.5) \cdot 10^{-3}$ |
| $2 \leq \Delta\eta \leq 3$ | | | | |
| 20 GeV/c | $21(15) \cdot 10^{-3}$ | $16(19) \cdot 10^{-3}$ | $31(28) \cdot 10^{-3}$ | $-19(57) \cdot 10^{-3}$ |
| 40 GeV/c | $-1.4(3.2) \cdot 10^{-3}$ | $2.7(4.9) \cdot 10^{-3}$ | $-7.5(4.9) \cdot 10^{-3}$ | $-5(12) \cdot 10^{-3}$ |
| 158 GeV/c | $-1.1(1.1) \cdot 10^{-3}$ | $-2.0(1.5) \cdot 10^{-3}$ | $-2.0(1.8) \cdot 10^{-3}$ | $4.3(2.5) \cdot 10^{-3}$ |

Table 4.8: Mean of differences *loose* – *tight* and systematic uncertainties of correlation functions (the latter given in brackets) for beam momenta: 20, 40, and 158 GeV/c, for all charge combinations and three ranges of pseudorapidity difference: full $0 < \Delta\eta < 3$, low $\Delta\eta \leq 2$, and high $\Delta\eta > 2$.

4.4 Comparison with models

4.4.1 EPOS and UrQMD

The corrected results, presented in Sec. 4.2.3, were compared to the results obtained from two models: EPOS1.99 [103], which was already used in this analysis to calculate detector effects (see Sec. 4.2.2 for details) and the UrQMD v3.4⁹ model [105, 106]. Table 4.9 shows the number of events generated and used in the analysis.

| Model | Beam momentum [GeV/c] | | | | |
|------------|-----------------------|------------------|------------------|------------------|-------------------|
| | 20 | 31 | 40 | 80 | 158 |
| EPOS1.99 | $5 \cdot 10^6$ | $5 \cdot 10^6$ | $5 \cdot 10^6$ | $5 \cdot 10^6$ | $5 \cdot 10^6$ |
| UrQMD v3.4 | $4 \cdot 10^6$ | $0.3 \cdot 10^6$ | $0.3 \cdot 10^6$ | $0.3 \cdot 10^6$ | $2.35 \cdot 10^6$ |

Table 4.9: Number of events generated in both models for each beam momentum.

The cuts for EPOS data were described in Sec. 4.1.2 (Pure MC sample). The UrQMD simulation conditions are described below:

- An option of generating jets was turned on¹⁰.
- Elastic events were suppressed (using the configuration file option), however a fraction of events with only two protons in the final state were still observed. Therefore, additional cuts on non-zero number of collisions, non-zero number of inelastic collisions, and the number of final state particles larger than 2 were applied to obtain only inelastic interactions.
- Time of simulation was set to 200 fm/c.
- The NA61/SHINE detector acceptance was applied, similarly as in EPOS, using Particle Population Matrix (see Appendix B for details).

⁹UrQMD abbreviation stands for Ultra-relativistic Quantum Molecular Dynamics.

¹⁰The option calls PYTHIA [107] routines that simulate hard processes for $\sqrt{s} > 10$ GeV.

- Transverse momentum cut: $p_T < 1.5$ GeV/c was used.

The comparisons are presented in Figs. 4.21, 4.22, 4.23, and 4.24. The EPOS model reproduces NA61/SHINE data well. However, an absence of near-side hill ($\Delta\eta, \Delta\phi \approx (0, 0)$) is visible in EPOS which is due to the lack of implementation of Bose-Einstein correlations in the model. This is noticeable especially for same-sign pairs. Correlations in EPOS for negatively charged pairs are almost flat.

The correlations obtained from UrQMD differ qualitatively. The most visible is an excessive maximum at $(\Delta\eta, \Delta\phi) \approx (0, \pi)$ for lower beam momenta which is clearly higher than the resonance hill which can be seen in the data. It is produced mostly in positively charged and unlike-sign pairs. The excess disappears at higher SPS energies. Despite of the lack of implementation of Bose-Einstein correlations (as in EPOS) the UrQMD model produces a strange structure at about $(0, 0)$. Especially, this distinctive structure in this region can be observed at medium beam momenta.

To make all the results from the inclusive analysis of p+p interactions more comparable to models, the correlation function was projected onto $\Delta\eta$ and $\Delta\phi$ axes, separately. The $C(\Delta\eta)$ function produced this way was plotted in four intervals: $0 < \Delta\phi < \pi/4$, $\pi/4 < \Delta\phi < \pi/2$, $\pi/2 < \Delta\phi < 3\pi/2$, and $3\pi/2 < \Delta\phi < \pi$. The $C(\Delta\phi)$ function was plotted in three different intervals: $0 < \Delta\eta < 1$, $1 < \Delta\eta < 2$, and $2 < \Delta\eta < 3$. Please note that, for this analysis, in order to estimate systematic uncertainties, a different binning (than the one shown in Tab. 4.8) in $\Delta\eta$ and $\Delta\phi$ was performed.

The results are presented in Figs. 4.25 and 4.26 and show general agreement between trends for corrected data (full boxes) and both models (lines). As mentioned earlier, the EPOS model (solid lines) reproduces data better than UrQMD (dotted line). In $\Delta\eta$ domain (Fig. 4.25) one can notice that EPOS results are systematically lower in $\Delta\eta < 1.5$ which may be a result of no Bose-Einstein correlations implemented in the model. The UrQMD model in $\Delta\phi$ domain (Fig. 4.26) produces correlations stronger for short-range region ($0 < \Delta\eta < 1$) and weaker in long-range region ($2 < \Delta\eta < 3$).

EPOS in large acceptance

The EPOS and UrQMD results presented above were prepared with the same acceptance restrictions as those in NA61/SHINE. In principle, single-particle azimuthal angle distribution in NA61/SHINE is not flat, while rapidity covers mainly forward hemisphere (see Appendix B for details of the NA61/SHINE acceptance). In Figs. 4.27 and 4.28 (upper panels) the results of EPOS without azimuthal angle and pseudorapidity restrictions are shown (only $p_T < 1.5$ GeV/c cut was applied). One sees that the correlation functions for both acceptances are qualitatively similar (only the maxima close to $\Delta\phi \approx \pi$ are slightly stronger in case of plots with larger acceptance). Thus, in case of EPOS, similar physics conclusions can be drawn also from large acceptance plots.

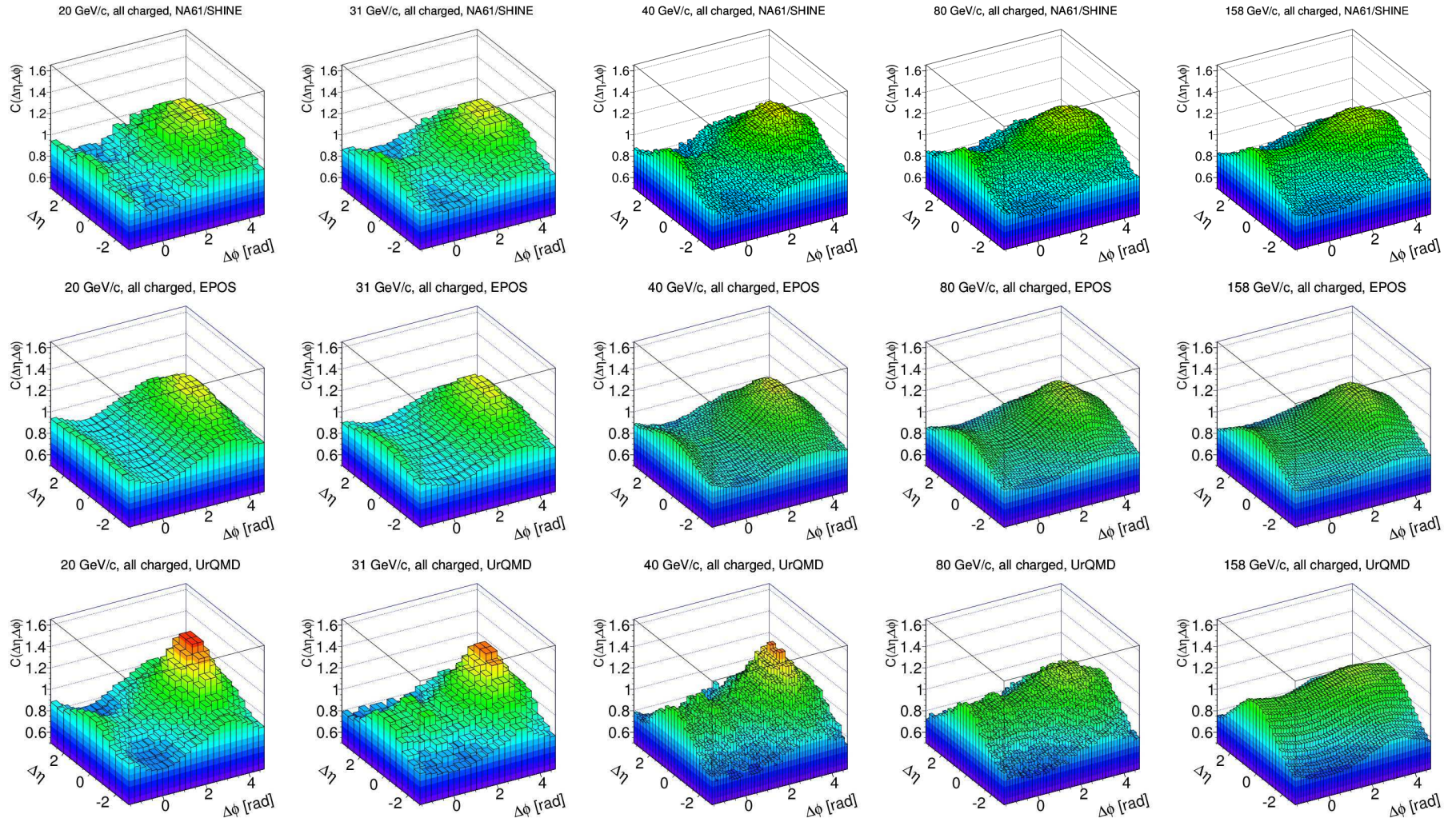


Figure 4.21: NA61/SHINE data (top row) compared to EPOS (middle row) and UrQMD (bottom row). Results for all charged pairs.

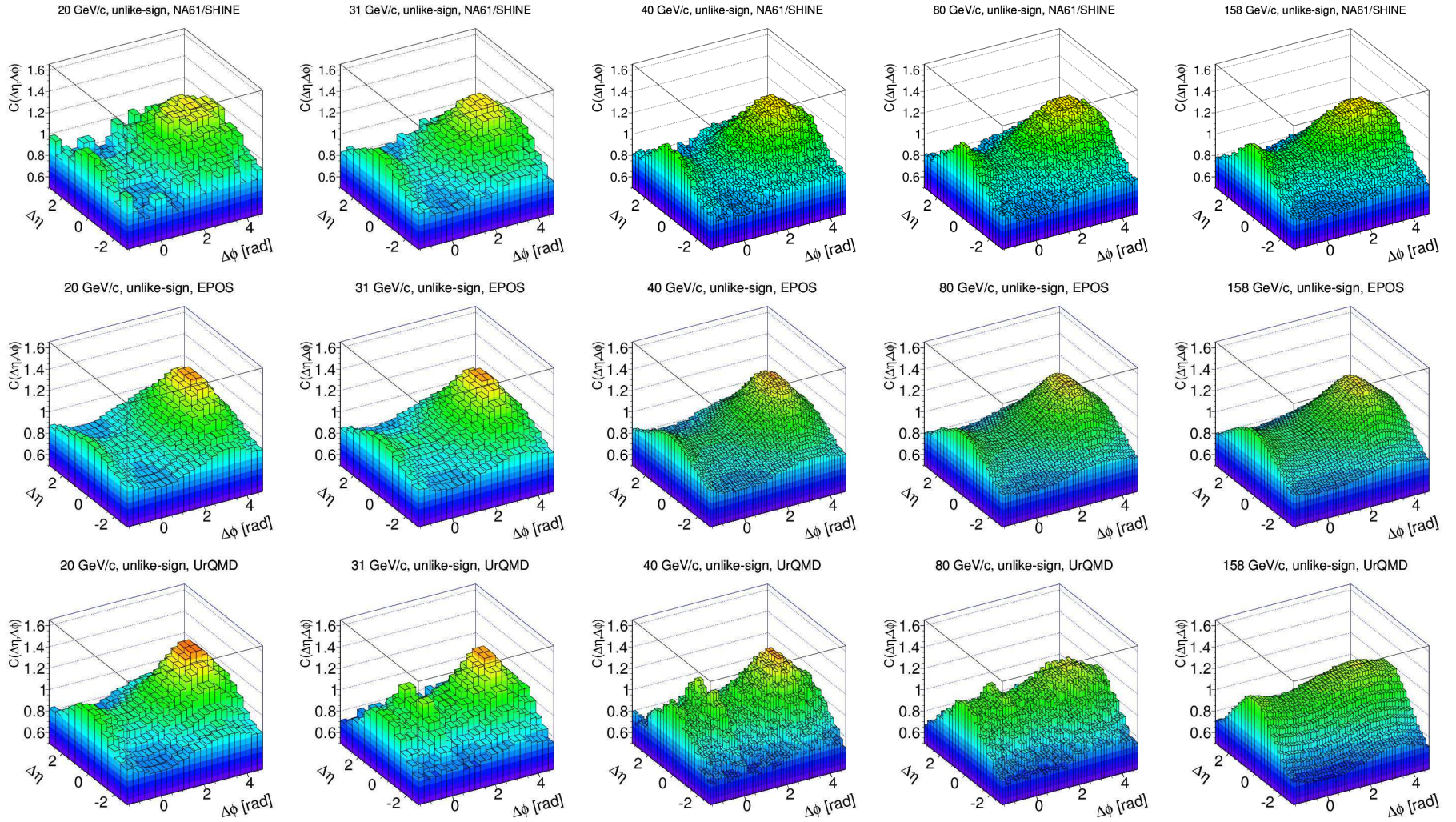


Figure 4.22: NA61/SHINE data (top row) compared to EPOS (middle row) and UrQMD (bottom row). Results for unlike-sign pairs.

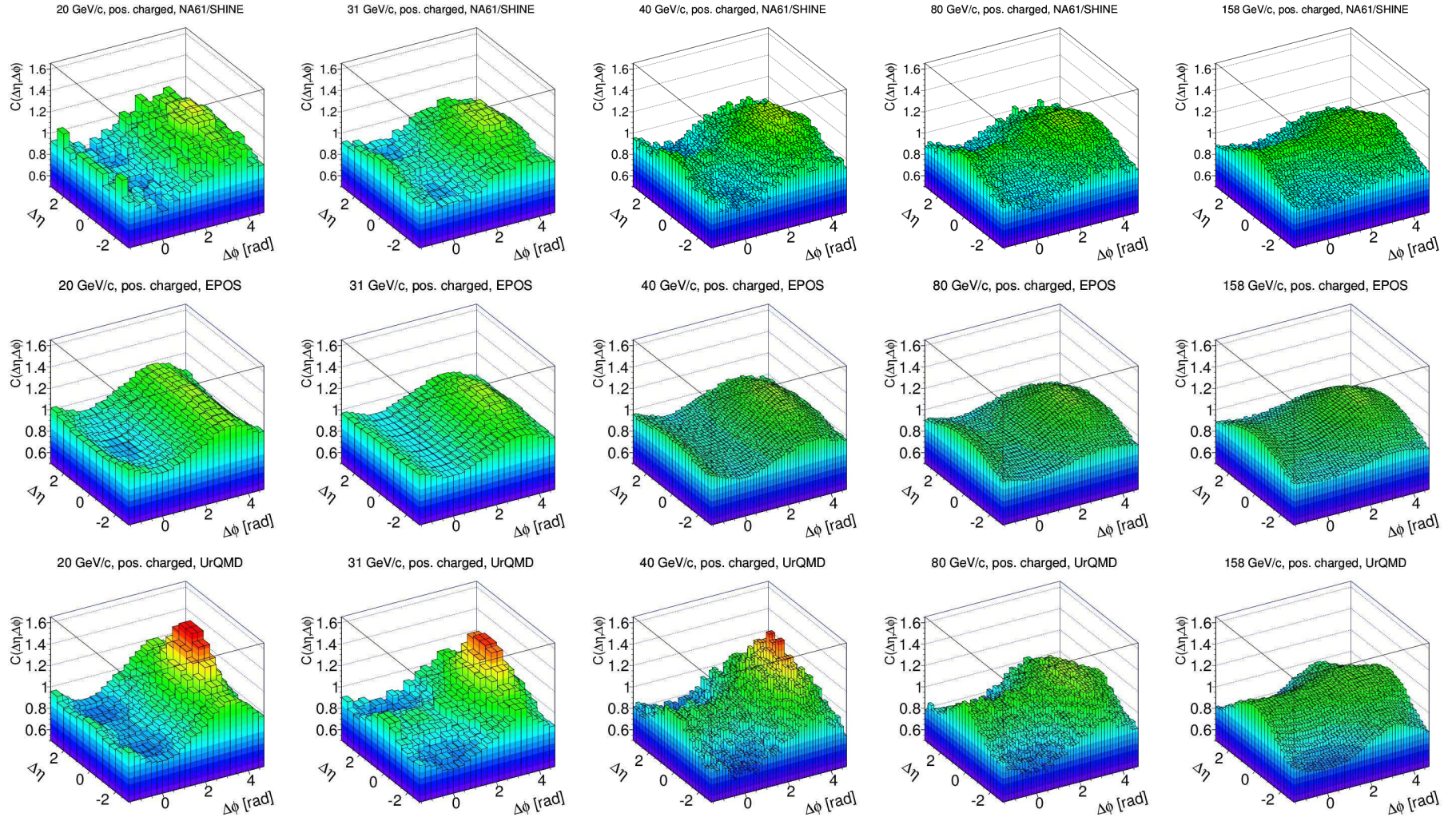


Figure 4.23: NA61/SHINE data (top row) compared to EPOS (middle row) and UrQMD (bottom row). Results for positively charged pairs.

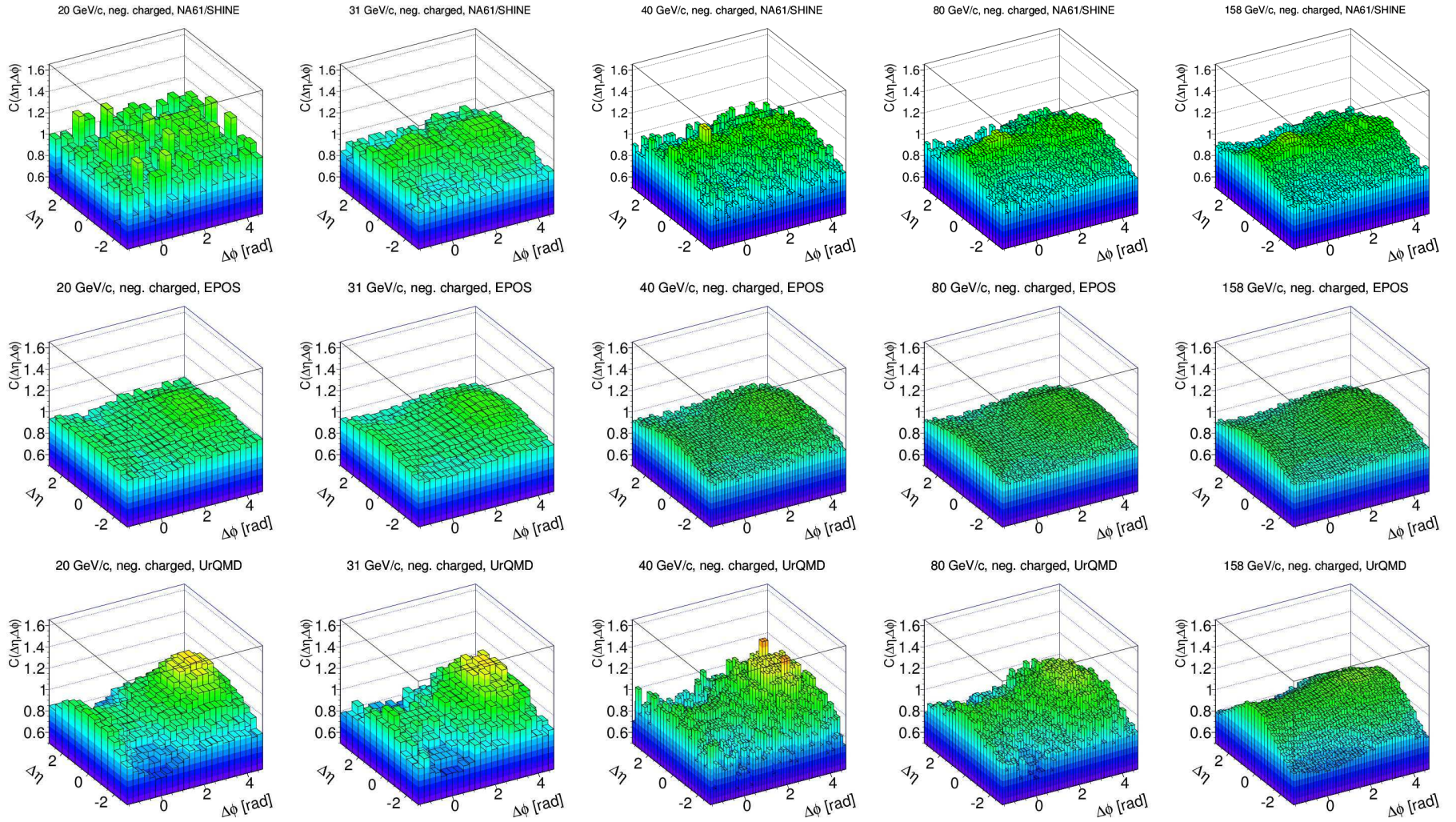


Figure 4.24: NA61/SHINE data (top row) compared to EPOS (middle row) and UrQMD (bottom row). Results for negatively charged pairs.

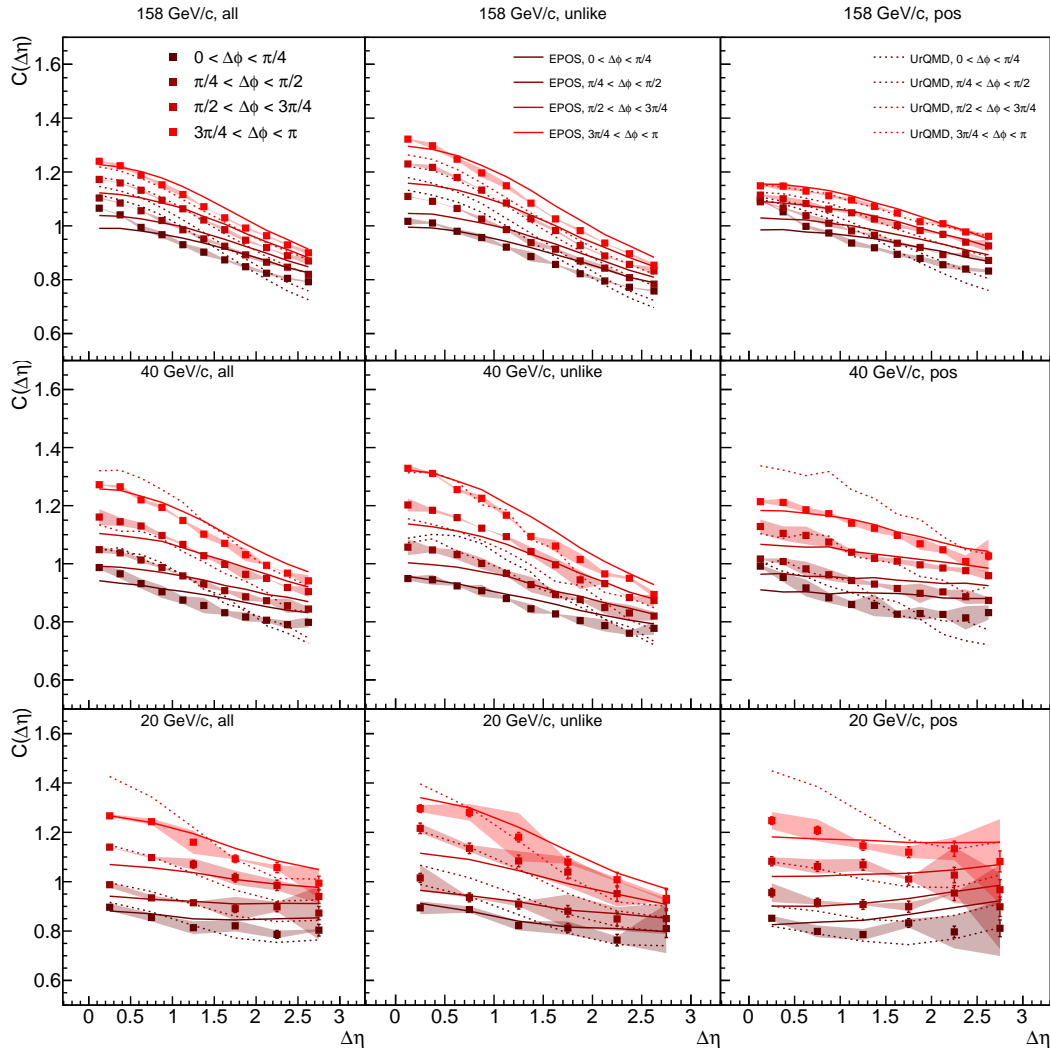


Figure 4.25: $C(\Delta\eta)$ function for p+p interactions in four $\Delta\phi$ intervals. Left column shows results for all charged pairs, middle column for unlike-sign pairs, right for positively charged pairs. EPOS and UrQMD predictions are also plotted, as well as statistical (vertical bars) and systematic (shaded regions) uncertainties.

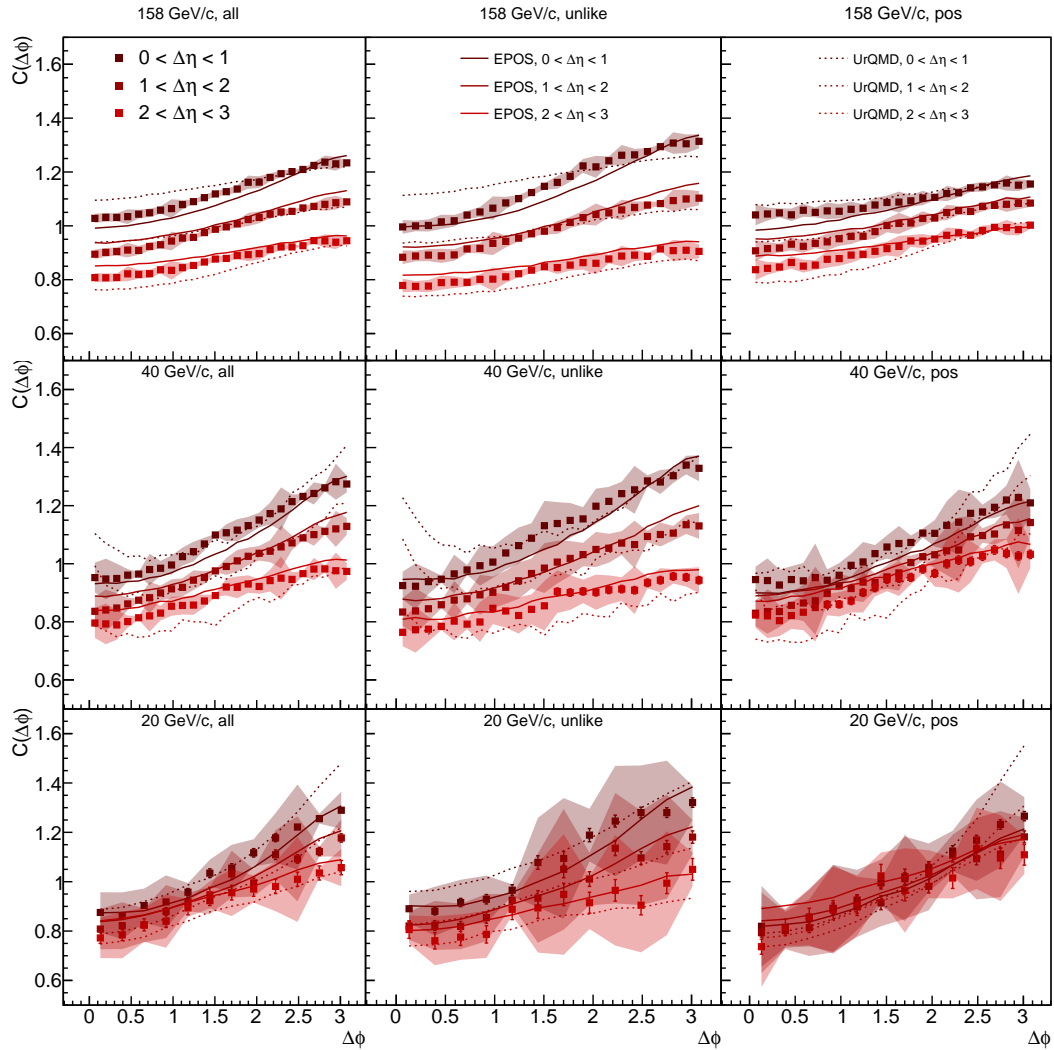


Figure 4.26: $C(\Delta\phi)$ function for p+p interactions in three $\Delta\eta$ intervals. Left columns shows results for all charged pairs, middle column for unlike-sign pairs, right for positively charged pairs. EPOS and UrQMD predictions are also plotted, as well as statistical (vertical bars) and systematic (shaded regions) uncertainties.

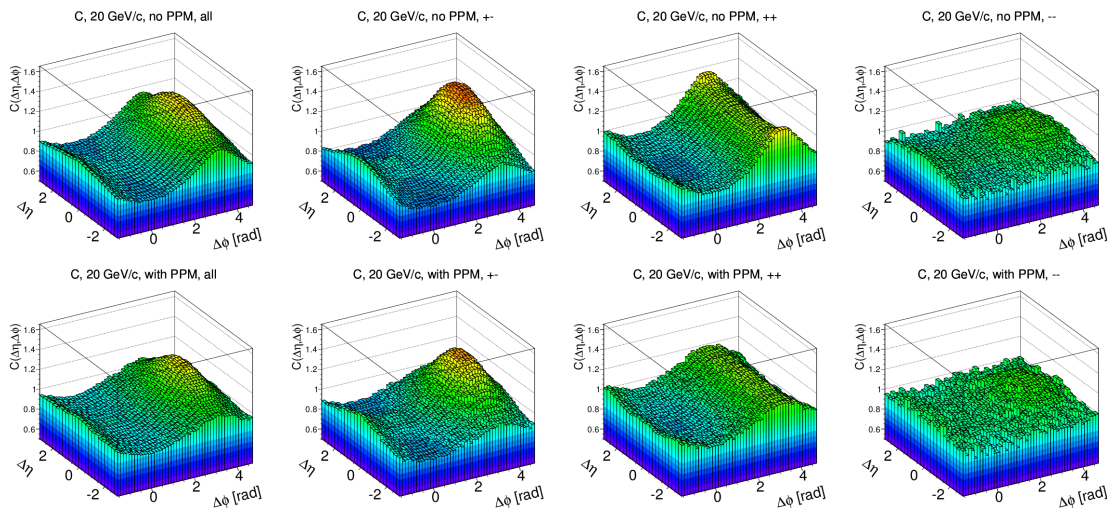


Figure 4.27: Correlation functions obtained for EPOS p+p collisions at 20 GeV/c. Upper panel: results for large acceptance (without Particle Population Matrix – PPM – applied). Lower panel: results within NA61/SHINE acceptance (PPM applied). Left column shows data for all charged particles, middle left for unlike-sign particles, middle right for positively charged, and right column for negatively charged particles.

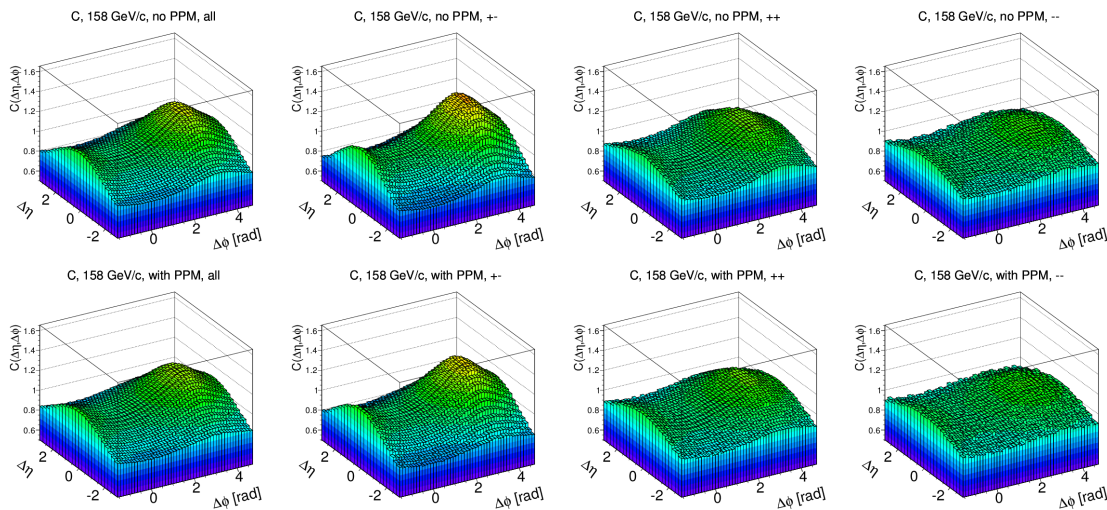


Figure 4.28: Correlation functions obtained for EPOS p+p collisions at 158 GeV/c. Upper panel: results for large acceptance (without Particle Population Matrix – PPM – applied). Lower panel: results within NA61/SHINE acceptance (PPM applied). Left column shows data for all charged particles, middle left for unlike-sign particles, middle right for positively charged, and right column for negatively charged particles.

4.4.2 Flux-tube fragmentation model

A longitudinal gaussian structure, which appears as an enhancement around $\Delta\eta = 0$ in $C(\Delta\eta, \Delta\phi)$ function for p+p, visible especially at higher beam momenta, may be a result of a flux-tube fragmentation. C.-Y. Wong provided model simulations [108] which agreed with $C(\Delta\eta, \Delta\phi)$ for unlike-sign pairs at top SPS. The comparison is shown in Fig. 4.29.

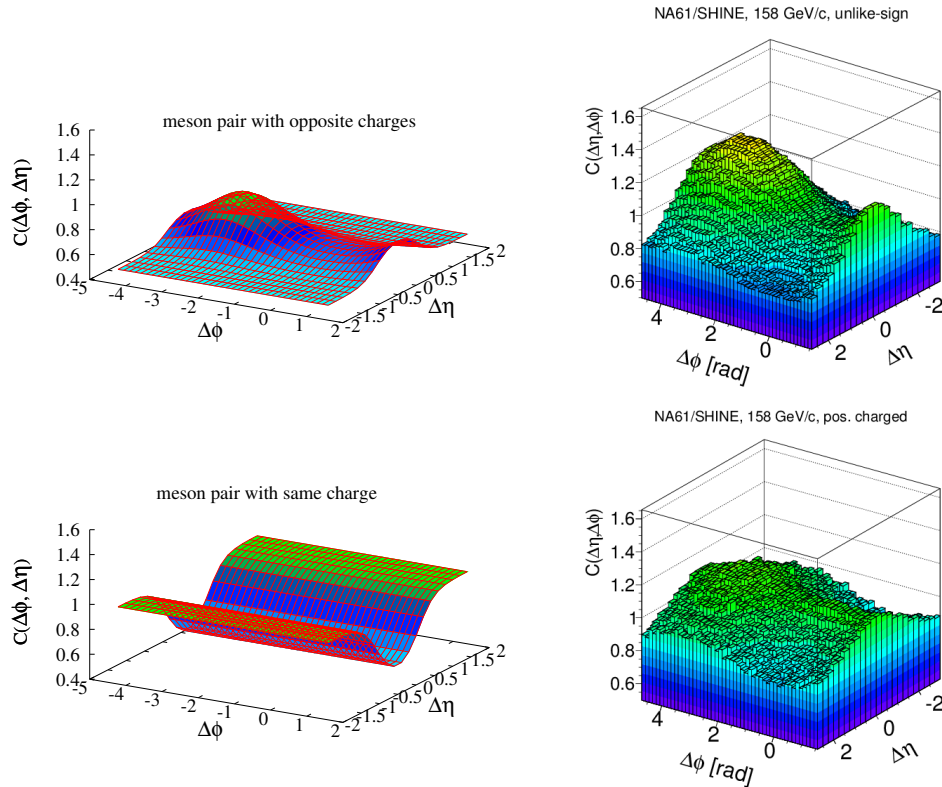


Figure 4.29: Left column: Correlation functions $C(\Delta\eta, \Delta\phi)$ obtained from flux-tube fragmentation model for two oppositely charged mesons (top left panel) and for two mesons with the same charge (bottom left panel). Right column: results of NA61/SHINE for unlike-sign pairs (top right panel) and for positively (same charged) pairs of particles (bottom right panel). Left figures taken from Ref. [108]. Right figures are corrected correlation function as shown in Sec. 4.2.3, with perspective after rotation to make the comparison with the model easier.

Wong explains the flux-tube fragmentation as a characteristic mechanism of soft physics domain [109]. A scheme of the mechanism is presented in Fig. 4.30. Let us consider the situation where during the collision two leading quarks form a flux-tube which is a polarized vacuum between these quarks pulling apart from each other. The flux-tube fragmentation process starts with production of many quark–anti-quark pairs along the tube. An example pair of quark–anti-quark (p_2 and p_3 in Fig. 4.30) is created at the vertex V . After the creation, quark p_2 interacts with anti-quark p_1 which was created in another vertex in the tube, while anti-quark p_3 interacts with quark p_4 from yet another vertex. The result of interactions are adjacent mesons P_{12} and P_{34} which almost do not interact with themselves. The formation of the nearly interacting mesons leads to the fragmentation of flux-tube along the longitudinal direction and, therefore, close to each other in rapidity. Production of a pair of adjacently produced mesons follows local conservation laws (charge, momentum) thus, this leads to near-side suppression and away-side enhancement in production of

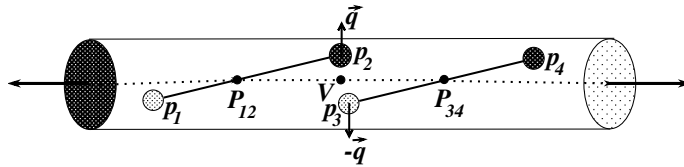


Figure 4.30: Schematic description of the production of quarks and anti-quarks in two adjacent mesons P_{12} and P_{34} . While the leading quark is pulling to the left and the leading anti-quark is pulling to the right, the quarks p_1 (anti-quark), p_2 (quark), p_3 (anti-quark), and p_4 (quark) are produced along the flux tube. Figure taken from Ref. [108].

particles with opposite charges. A simulation performed by C.-Y. Wong produced results consistent with NA61/SHINE data (see Fig. 4.29, top left and top right for a comparison). The interpretation of the results is that oppositely charged mesons are likely to be correlated back-to-back, because their constituent quarks were produced at the same spatial point (e.g. both at vertex V in Fig. 4.30) where the production required local conservation of charge and momentum.

Unfortunately, the flux-tube fragmentation model does not explain NA61/SHINE results for same-sign charged pairs. The model predicts a longitudinal gaussian valley along $\Delta\phi$ for $\Delta\eta \approx 0$ for the same-sign charged pairs of mesons, which does not agree with NA61/SHINE data for positively nor for negatively charged particles (see the comparison in Fig. 4.29, bottom left and bottom right panels). The disagreement is currently explained by the limitation of the model. Namely, the model creates primary mesons only, therefore there is no implementation of the decays to secondary particles. According to the model, the gaussian valley (see bottom left panel in Fig. 4.29) is visible because it is unlikely to have two adjacently produced primary particles of the same charges. Although the model allows to produce mesons like ρ^0 resonance (which, in reality, decays into pair π^+ and π^-), the lack of implementation of the decays makes it only a neutral particle which is not taken into account in the two-particle correlations analysis. In general, ρ^0 decay products (π^+ and π^-) could be combined with primary produced charged mesons to form structures as visible in data [110]. Due to the fact that, at the moment, the model does not implement meson decays (in particular, neutral meson ρ^0), instead of the structures observed in NA61/SHINE, we see a gaussian valley along $\Delta\phi$ at $\Delta\eta \approx 0$ [110].

4.5 Contribution of jets

4.5.1 Analysis with p_T restrictions

An additional analysis was performed to study jets contribution to $\Delta\eta\Delta\phi$ correlations at 158 GeV/c. As described in Sec. 2.3 correlations from jets manifest in two structures: high near-side ($\Delta\phi \approx 0$) peak as a result of many particles traveling within the same (leading) jet (therefore, having similar production angle) and an away-side ($\Delta\phi \approx \pi$) enhancement being a contribution of correlations between particles from opposite jets of a di-jet. The main part of the analysis done in this thesis (presented in Sec. 4.2) was meant to discover the correlation sources in soft physics domain. Because hard physics processes start to dominate in transverse momentum range $p_T > 1.5$ GeV/c, the p_T cut was applied on the results of inclusive analysis. In this section an analysis was done to study the contribution of jets, thus a restriction on minimal transverse momentum of the analyzed particles was introduced.

It should be mentioned that an attempt to reject all particles with p_T below 1.5 GeV/c leads to loss of statistics so significant, that qualitative distinction of any correlation structure is very difficult due to large bin-by-bin fluctuations. Therefore, three cuts on minimal transverse momentum were applied to data to find any structures emerging or vanishing in dependence of the minimal p_T cut. The analysis was performed on full statistics of NA61/SHINE data on p+p collisions at beam momentum 158 GeV/c. The applied cuts were the same as in the previous analysis (cuts were described in Sec. 4.1) with exception of transverse momentum cut. Results for no p_T restrictions were obtained as well as for three minimal transverse momentum cuts: $p_T > 0.5$ GeV/c, $p_T > 0.75$ GeV/c, and $p_T > 1$ GeV/c. They were compared with full statistics EPOS and UrQMD generated events analyzed with the same p_T conditions.

Figures 4.31, 4.32, 4.33, and 4.34 present correlation functions for aforementioned transverse momentum cuts, for NA61/SHINE data as well as EPOS and UrQMD. Note the vertical scale change when compared to $C(\Delta\eta, \Delta\phi)$ distributions shown before. One sees, that for data the near-side jet peak ($\Delta\eta, \Delta\phi) = (0, 0)$ does not appear at high p_T . Therefore, jet contribution at SPS energies is small.

A global trend is seen that an away-side $\Delta\eta$ -wide structure emerges with increasing minimal p_T cut. While presented in a common scale, the results with no transverse momentum restrictions are almost flat; the ones with particles with momentum higher than 1 GeV/c show a steep long-range enhancement at $\Delta\phi \approx \pi$ and a suppression in near-side region. Another interesting structure is coming from particles produced in back-to-back ($\Delta\phi \approx \pi$) manner and with large pseudorapidity separation. The structure is qualitatively similar to away-side ridge presented in many plots in Sec. 2.3 which, in the experiments at RHIC and LHC, was interpreted as correlations of particles from the opposite jets of a di-jet or as a result of momentum conservation. Because the NA61/SHINE results do not show any significant signal of the near-side peak, the explanation of this structure as a result of momentum conservation is more probable.

The EPOS model at high p_T generates more particles correlated back-to-back ($\Delta\phi \approx \pi$ and in $|\Delta\eta| < 1.5$) than it is visible in data, especially in all charged and unlike-sign pairs. On the other hand, UrQMD generates more particles correlated back-to-back but on longer range ($|\Delta\eta| > 1.5$) than they are produced in real interactions. Moreover, the near-side region is reproduced better by EPOS, while UrQMD produces there a small hill for all p_T

| Particle | $\overline{p_T}$ [GeV/c] |
|-----------|--------------------------|
| π^+ | 0.357 |
| π^- | 0.362 |
| K^+ | 0.470 |
| K^- | 0.462 |
| p | 0.578 |
| \bar{p} | 0.514 |

Table 4.10: NA61/SHINE (non-official) results [111] on inclusive mean transverse momentum ($\overline{p_T}$) of identified particles in p+p collisions at beam momentum 158 GeV/c. Results obtained from p_T -extrapolated spectra at midrapidity ($0 < y < 0.2$). Statical uncertainties (not presented) are on the level of 5%.

cuts.

The NA61/SHINE distributions with p_T restrictions are qualitatively similar to the ALICE results of identified protons with elongated structure at $\Delta\phi \approx \pi$ (see Fig. 2.24).

According to the NA61/SHINE results of mean transverse momentum for identified particles (see Tab. 4.10) protons have the highest mean transverse momentum. It suggests that, with increasing minimal p_T cut, lighter particles are rejected more than heavier (like protons). Thus, p_T restricted distributions qualitatively agree with distributions of two-proton correlations presented by ALICE. This would suggest that the away-side enhancement along $\Delta\eta$ and near-side depression are the structures characteristic for correlations between protons. Another argument, which could confirm that higher p_T distributions contain mostly protons, is that dE/dx distributions with rejected lower p_T particles (Fig. 4.35) reveal higher proton contribution with increasing minimal p_T cut. As seen, the proton “cloud” (lower “strip”) gets more pronounced with respect to the pion “cloud” (upper “strip”) with increasing cut on minimal p_T .

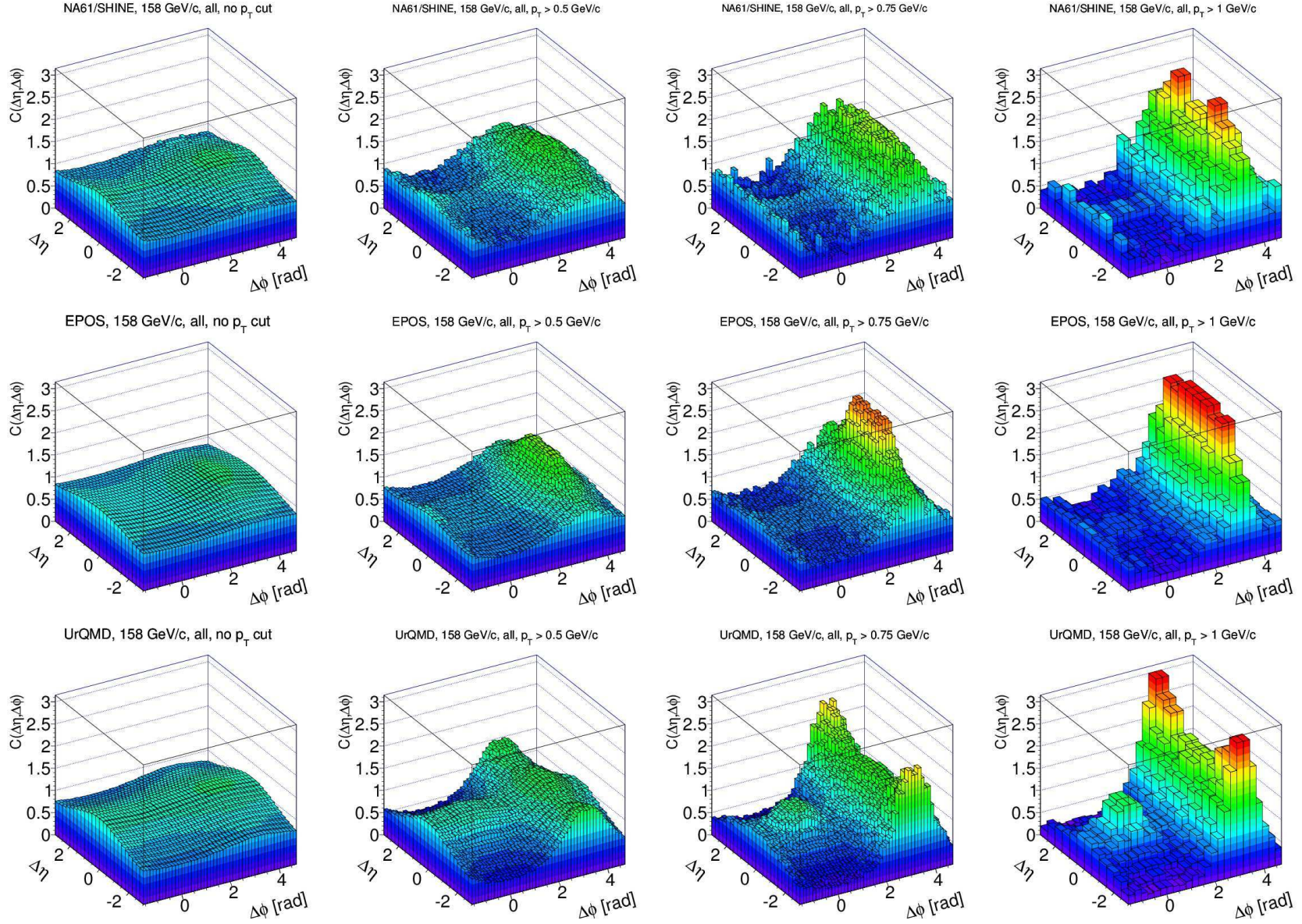


Figure 4.31: Distributions of $C(\Delta\eta, \Delta\phi)$ correlation function for various p_T cut conditions in p+p collisions at beam momentum 158 GeV/c. From left to right: without p_T cut, with $p_T > 0.5$ GeV/c cut, with $p_T > 0.75$ GeV/c cut, with $p_T > 1$ GeV/c cut. Top row contains results for NA61/SHINE data, middle row for EPOS, bottom row for UrQMD. Results for all charged pairs.

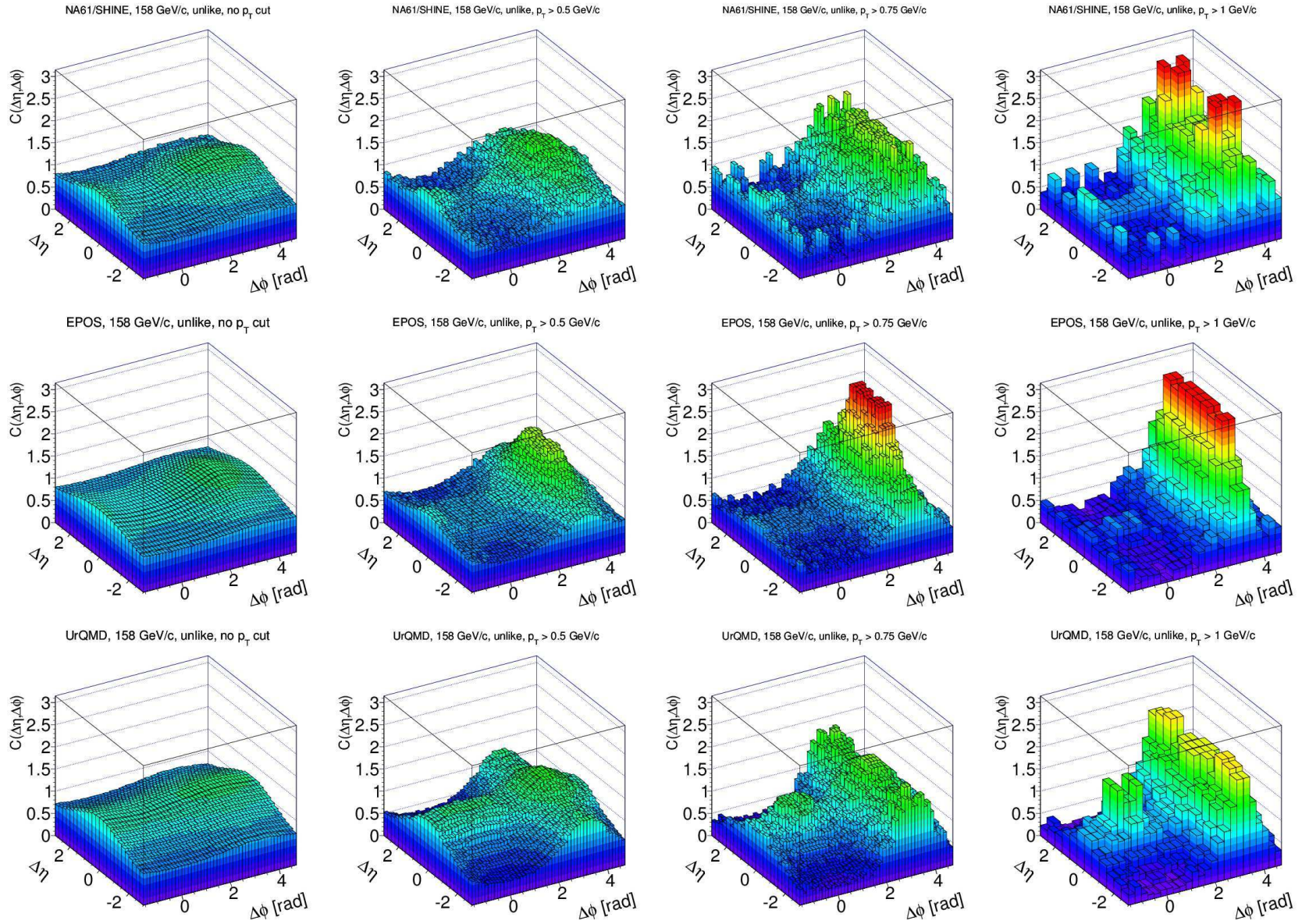


Figure 4.32: Distributions of $C(\Delta\eta, \Delta\phi)$ correlation function for various p_T cut conditions in p+p collisions at beam momentum 158 GeV/c. From left to right: without p_T cut, with $p_T > 0.5$ GeV/c cut, with $p_T > 0.75$ GeV/c cut, with $p_T > 1$ GeV/c cut. Top row contains results for NA61/SHINE data, middle row for EPOS, bottom row for UrQMD. Results for unlike-sign charged pairs.

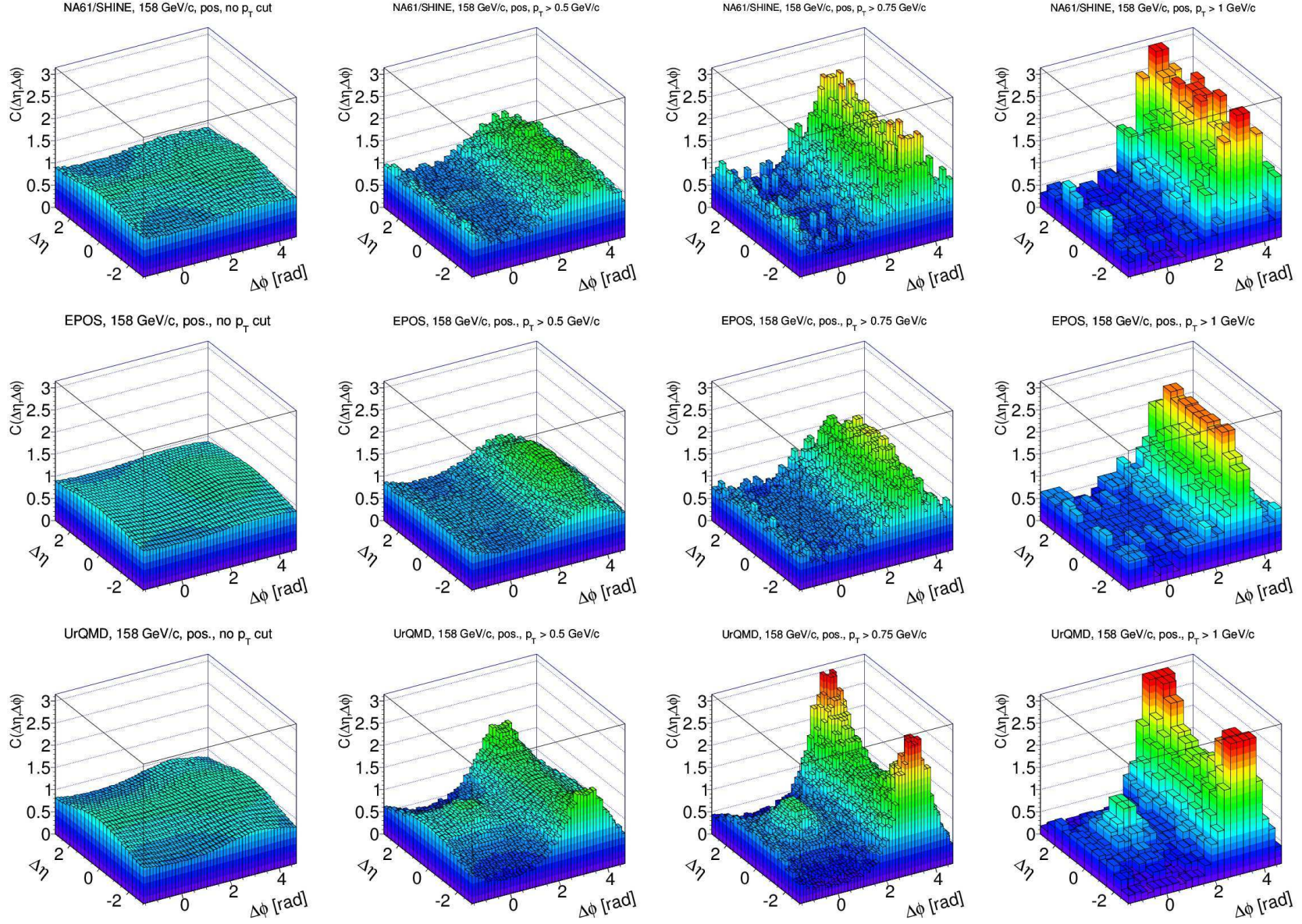


Figure 4.33: Distributions of $C(\Delta\eta, \Delta\phi)$ correlation function for various p_T cut conditions in p+p collisions at beam momentum 158 GeV/c. From left to right: without p_T cut, with $p_T > 0.5$ GeV/c cut, with $p_T > 0.75$ GeV/c cut, with $p_T > 1$ GeV/c cut. Top row contains results for NA61/SHINE data, middle row for EPOS, bottom row for UrQMD. Results for positively charged pairs.

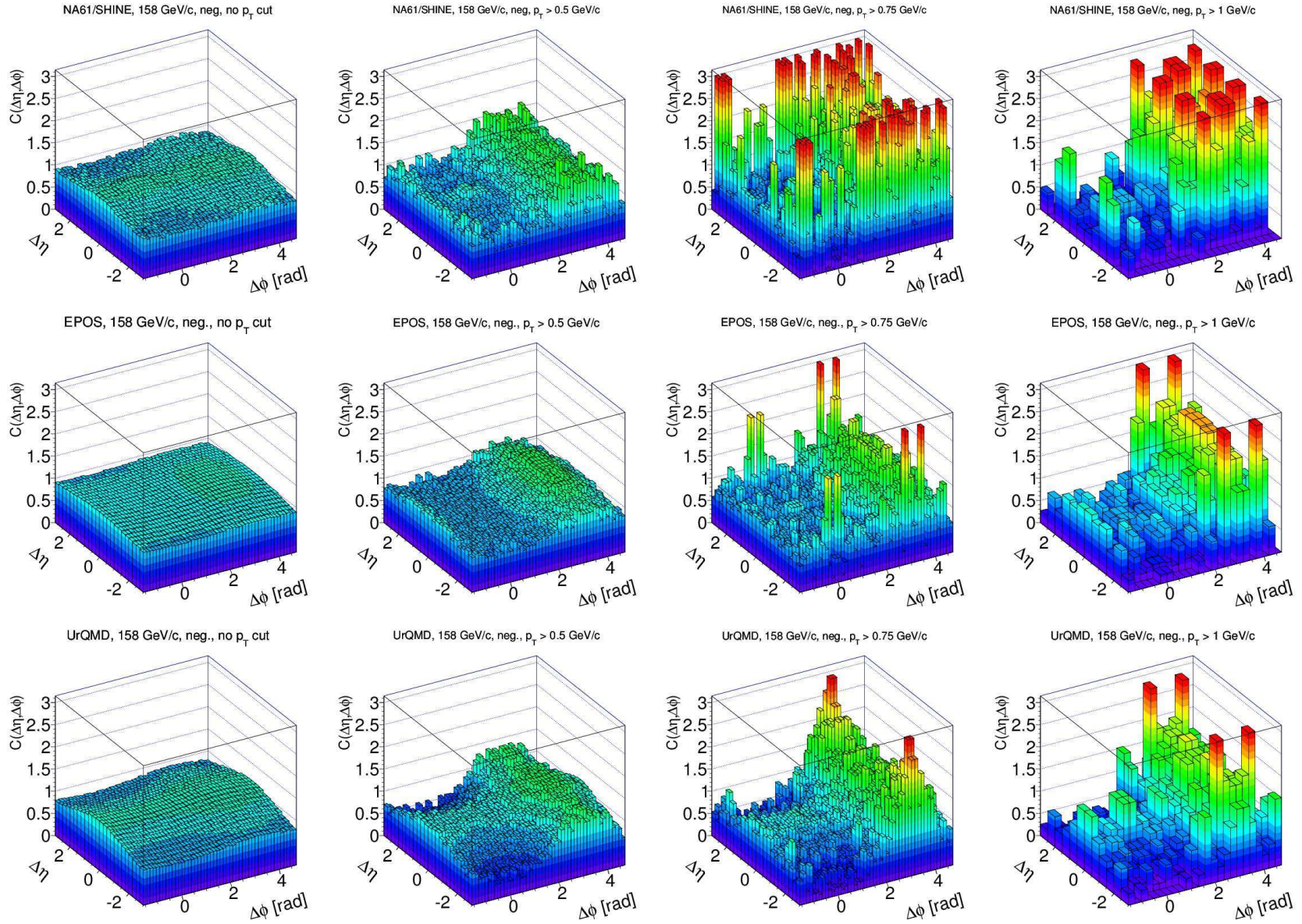


Figure 4.34: Distributions of $C(\Delta\eta, \Delta\phi)$ correlation function for various p_T cut conditions in p+p collisions at beam momentum 158 GeV/c. From left to right: without p_T cut, with $p_T > 0.5$ GeV/c cut, with $p_T > 0.75$ GeV/c cut, with $p_T > 1$ GeV/c cut. Top row contains results for NA61/SHINE data, middle row for EPOS, bottom row for UrQMD. Results for negatively charged pairs.

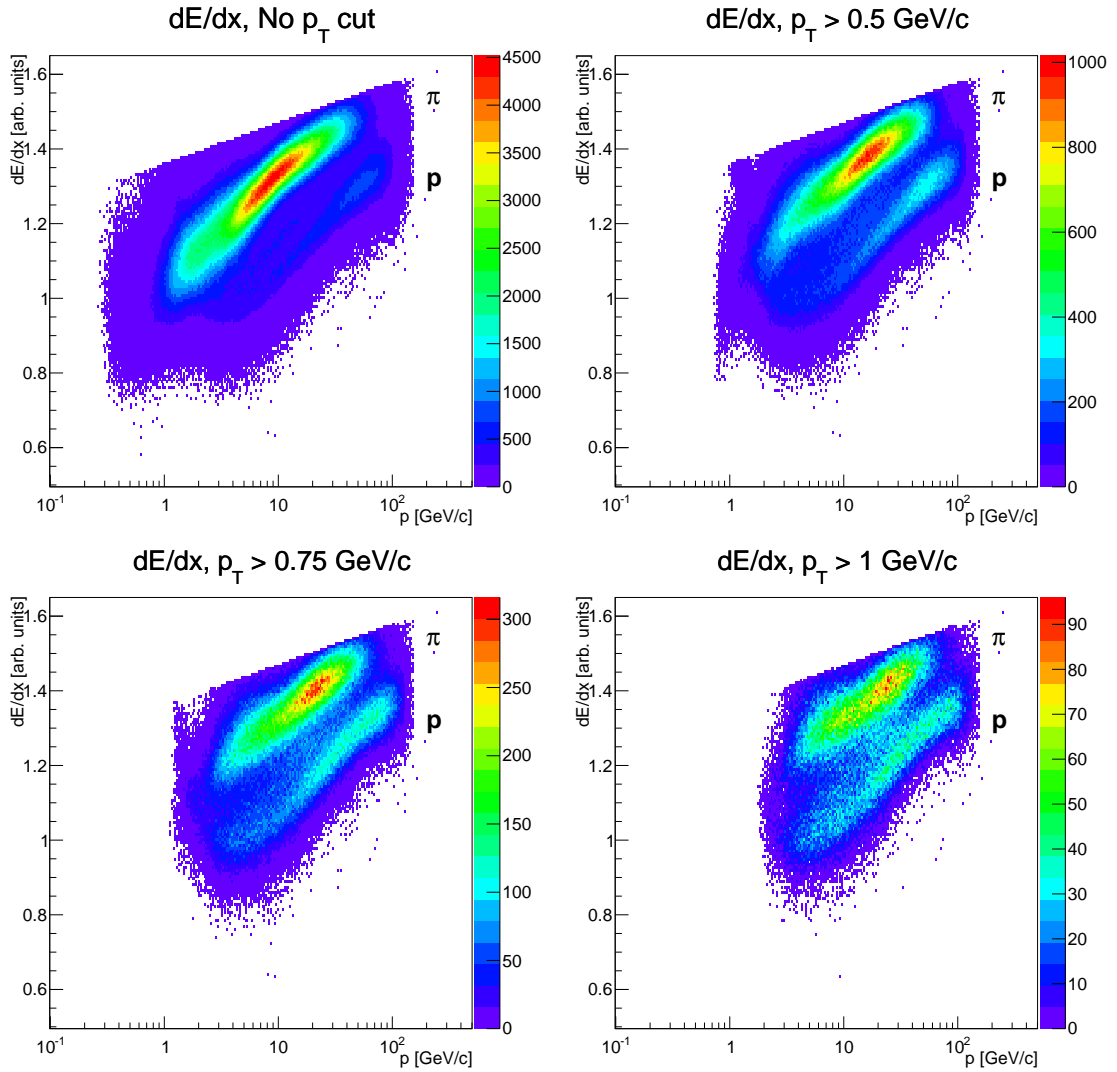


Figure 4.35: dE/dx distributions versus total momentum with changing minimal transverse momentum cut. Presented for all charged particles produced in p+p collisions at beam momentum 158 GeV/c.

4.5.2 UrQMD pseudo-jet structure

The structures visible in UrQMD for the highest transverse momentum restrictions (see bottom right panel in Figs. 4.31, 4.32, 4.33, and 4.34) are unusual enough to check how they look like at the lowest beam momentum. Therefore, a similar analysis was done on UrQMD data only at beam momentum 20 GeV/c. The comparison of results at beam momenta 20 and 158 GeV/c for all charged and unlike-sign pairs and for two transverse momentum cut configurations is presented in Fig. 4.36.

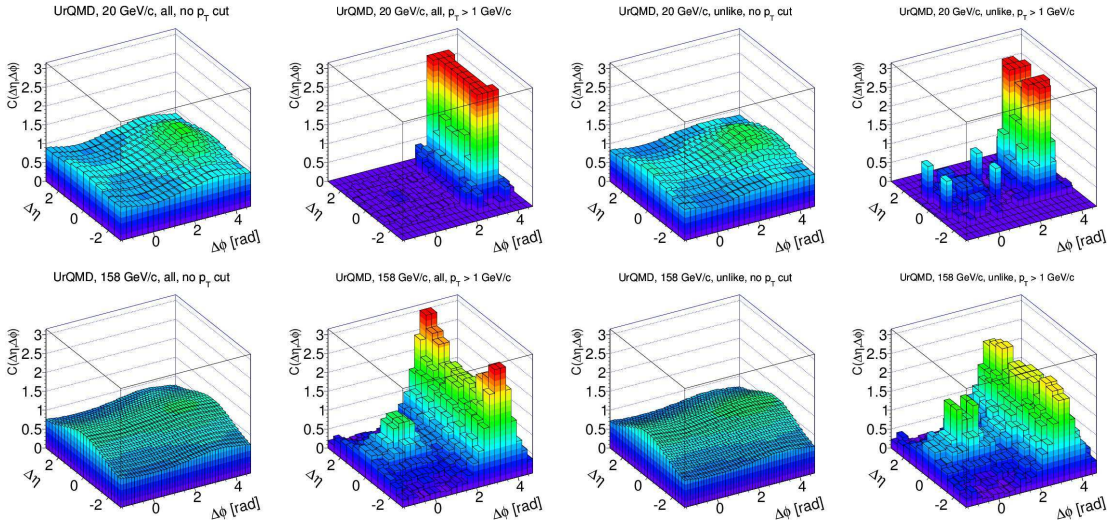


Figure 4.36: $C(\Delta\eta, \Delta\phi)$ function distributions for UrQMD data generated at 20 GeV/c (top row) and 158 GeV/c (bottom row). Presented for all charged (two left columns) and unlike-sign (two right columns) pairs with different momentum cut restrictions: without any cuts (first and third column) and with $p_T > 1$ GeV/c cut (second and fourth column).

Due to very low statistics in 20 GeV/c results (because of low event multiplicity connected with high minimal p_T restriction) only two structures are present in the distributions. The most visible is the elongated structure at $\Delta\phi \approx \pi$, but the one around $(\Delta\eta, \Delta\phi) = (0, 0)$ is also emerging. The probability of a jet production at such low momentum like 20 GeV/c ($\sqrt{s_{NN}} = 6.3$ GeV/c) is much lower than at 158 GeV/c ($\sqrt{s_{NN}} = 17.3$ GeV/c)¹¹. Despite this fact, the near-side enhancement in UrQMD appears at both beam momenta. Therefore, interpreting this structure as a result of jets is excluded. The other, away-side structure, noticeable in the results with high minimal p_T restriction, may be a result of conservation laws.

The results presented in this analysis were produced in the same simulation conditions as the previous results described in Sec. 4.4.1. In particular, jets simulation option was enabled. However, it has been checked if the results change with the option of jets simulation disabled, but the results are similar both qualitatively and quantitatively. This is another argument that the UrQMD structures visible with high minimal p_T cut are not connected with jet production.

¹¹In fact, UrQMD does not even start jet production for $\sqrt{s} \leq 10$ GeV.

4.6 Results of semi-inclusive analysis in multiplicity bins

An additional analysis on multiplicity bins was performed on p+p interactions. This analysis was meant to cover the region of two-particle correlations in events with different multiplicities at beam momenta much lower than the ones achieved in LHC. The LHC experiments showed that $\Delta\eta\Delta\phi$ correlations in p+p collisions are different for low and high multiplicity bins (or for different centralities).

In this analysis contributions of events with two, three, four, five, six, and seven produced particles in various charge combinations for p+p collisions at beam momentum 158 GeV/c are studied (see Fig. 4.37 for multiplicity distributions of accepted particles in NA61/SHINE p+p at 158 GeV/c). The analyzed dataset consisted of events and tracks accepted in the inclusive analysis (cuts described in Sec. 4.1). The data was divided into six separate multiplicity bins (2,3,4,5,6,7) in three charge combinations:

- **All:** Events composed by two, three, four, five, six, or seven accepted charged particles.
- **Positively charged (Pos):** Events composed by any number of charged particles but having two, three, four, five, six, or seven accepted positively charged ones.
- **Negatively charged (Neg):** Events composed by any number of charged particles but having two, three, four, five, six, or seven accepted negatively charged ones.

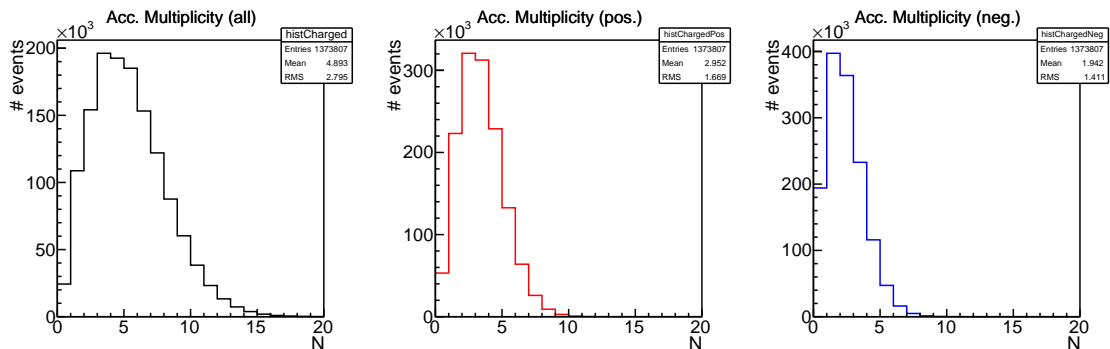


Figure 4.37: Multiplicity distributions of accepted particles in NA61/SHINE p+p collisions at 158 GeV/c. Multiplicities are given for all charged (left), positively charged (middle), and negatively charged (right).

The mixing procedure (described in Sec. 2.1.2) was done for each of subdatasets separately. The results were corrected for detector effects by applying the same procedure as described in Sec. 4.2.2. Figure 4.38 shows corrections for detector effects in different multiplicity bins. The largest corrections (up to 20%) are in the lowest multiplicity bin for dataset that takes into account all charged particles. It is due to low statistics, namely a relatively small number of events which contain two charged particles only. In the remaining cases, the corrections are up to 10%.

The corrected correlation functions in six different multiplicity bins in inelastic p+p interactions at beam momentum 158 GeV/c are shown in Fig. 4.39. It can be clearly seen that the structures are the most prominent in the lowest multiplicity bin and then smeared with increasing multiplicity. The smearing effect is probably due to increased statistics. Moreover, if one interprets the away-side enhancement as a result of momentum

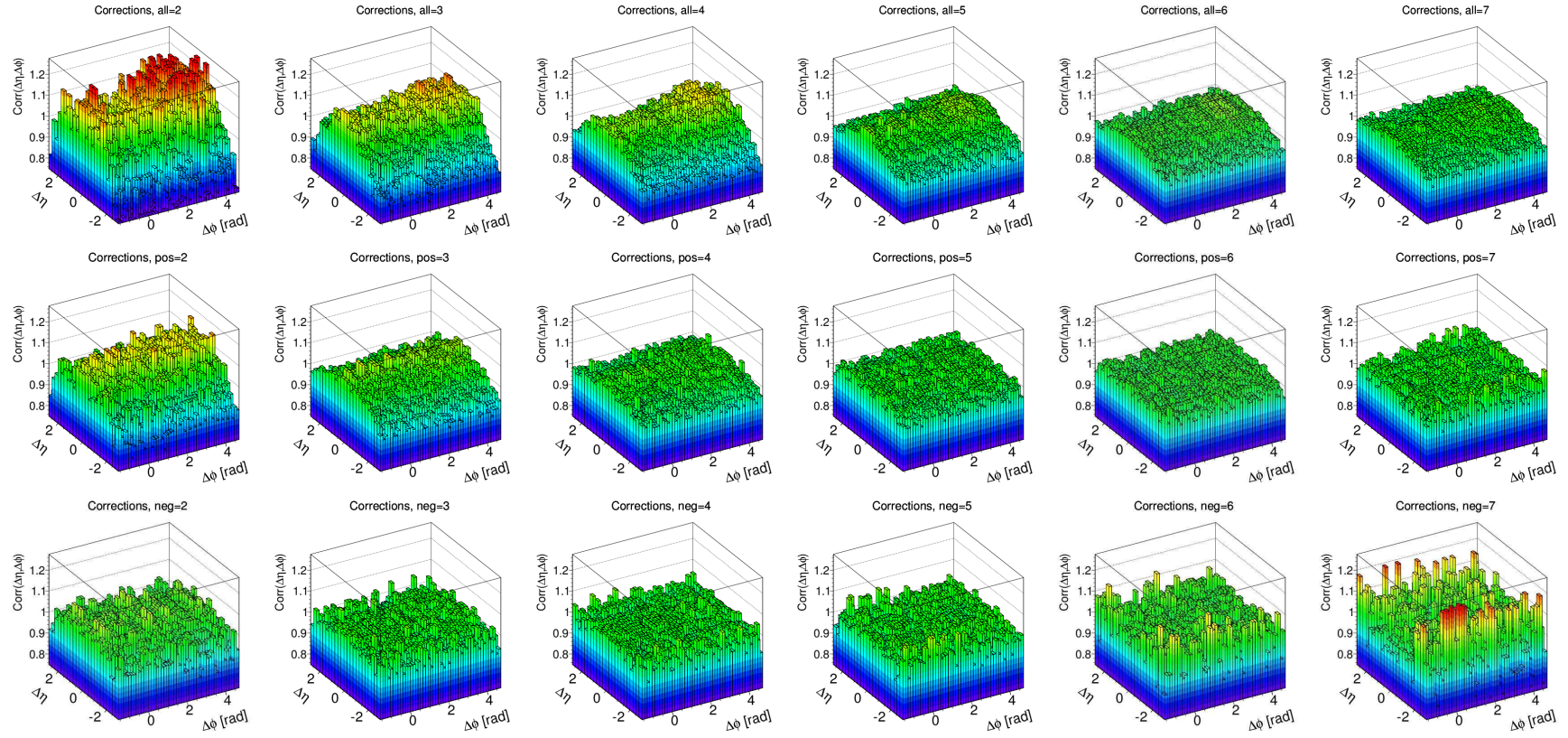


Figure 4.38: Corrections $\text{Corr}(\Delta\eta, \Delta\phi)$ for different accepted multiplicity bins of p+p at 158 GeV/c. Top row presents results for all charged particles, middle row for positively charged particles, bottom row for negatively charged particles. Multiplicities of accepted particles increase from left to right.

conservation and resonance decays, the smearing effect may be due to the fact, that the contributions from both phenomena are the largest for the events with low number of final state particles and are smeared in higher multiplicity events by particles coming from other sources. Distributions in low multiplicity bins at 158 GeV/c are qualitatively similar to according inclusive results at low beam momenta (see Figs. 4.11, 4.13, and 4.14 for a comparison), while distributions in higher multiplicity bins are more similar to inclusive results at 158 GeV/c. The most prominent is a hill in away-side region, probably being a result of resonance decays and momentum conservation. The hill is the best visible for all charged pairs, but it is still noticeable for positively charged pairs. A low enhancement at near-side region for both positively and negatively charged pairs, that persists in through all multiplicity bins, can be also noticed. This enhancement is probably an effect of Bose-Einstein statistics. Finally, there are rather no additional and different structures appearing in high multiplicity events when compared to low multiplicity ones.

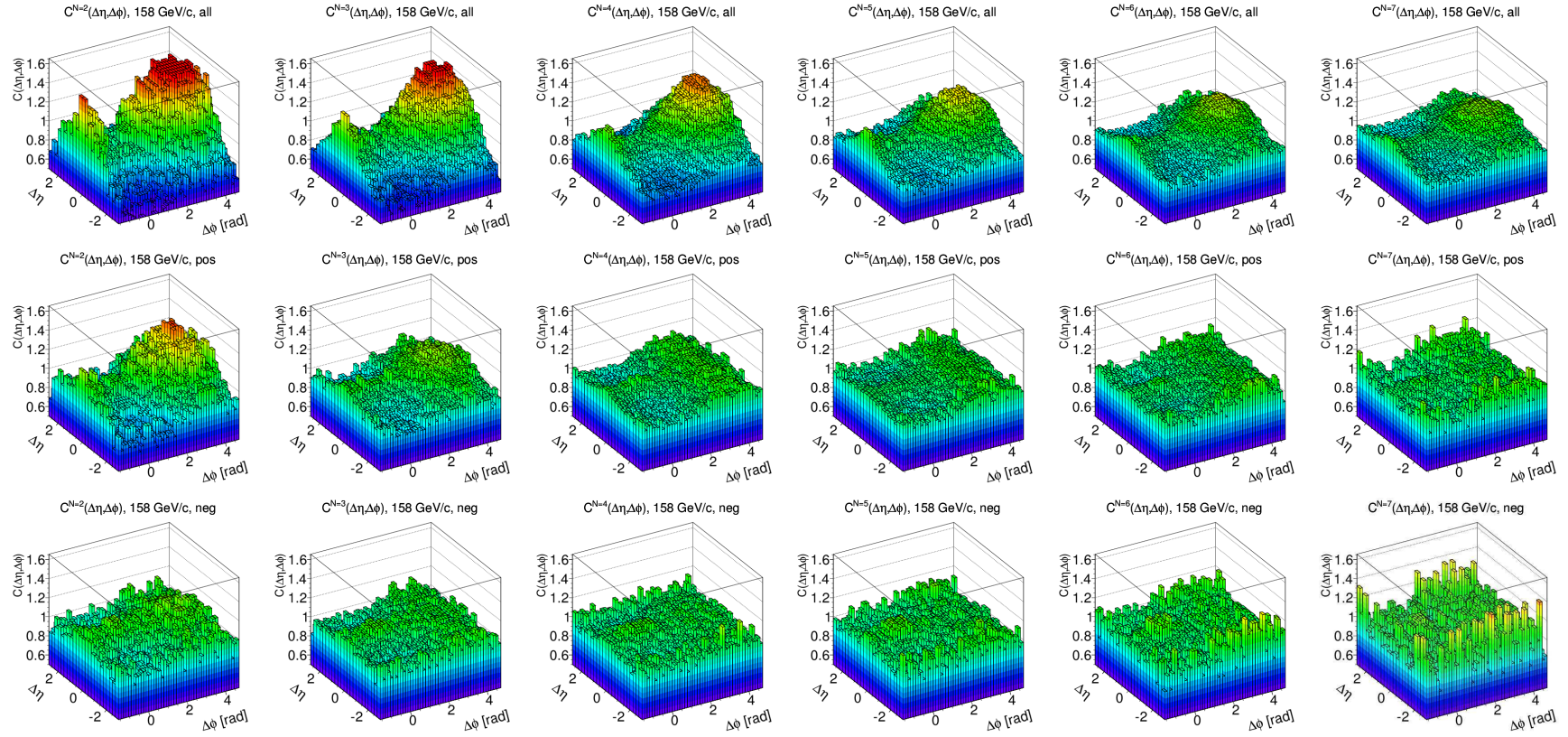


Figure 4.39: Corrected $C(\Delta\eta, \Delta\phi)$ in accepted multiplicity bins for three different charge combinations in inelastic p+p at 158 GeV/c. Top row presents results in events with a given number of accepted charged particles. Middle row – results in events with a given number of accepted positively charged particles. Bottom row – results with a given number of accepted negatively charged particles.

4.7 Comparison with other experiments

Corrected NA61/SHINE results on p+p interactions were compared to p+p results from other experiments. The comparison is presented in Fig. 4.40 and contains already shown NA61/SHINE results from the inclusive analysis (see Sec. 4.2.3) presented in the first row and two left plots of the second row. Since the original analysis was performed with $p_T < 1.5$ GeV/c cut, an additional plot, with no such cut, is also presented (Fig. 4.40, second row, rightmost plot). The results without p_T cut were discussed in Sec. 4.5 (however, with different vertical scale; see Fig. 4.31). Because there are almost no differences between p+p at 158 GeV/c results with $p_T < 1.5$ GeV/c and without p_T cut, the other plots for lower NA61/SHINE energies are not presented.

For the comparison, minimum-bias results for p+p collisions from different experiments (more details in Sec. 2.3) are presented: collisions at 200 GeV from PHOBOS (Fig. 4.40, third row, left plot), at 0.9 and 7 TeV from ATLAS (Fig. 4.40, third row, middle and right plots), at 0.9, 2.36, and 7 TeV from CMS (Fig. 4.40, fourth row), and at 0.9, 2.76, and 7 TeV from ALICE (Fig. 4.40, bottom row).

The biggest visible difference between NA61/SHINE and other results is the lack of peak at $(\Delta\eta, \Delta\phi) = (0, 0)$ which is interpreted as a contribution of particles taking part in hard processes – (mini)jets. The absence of such structures suggests that even beam energy of 158 GeV ($\sqrt{s} = 17.3$ GeV) is not sufficient to let hard processes to show up. However, a small enhancement in this region, that rises with increasing beam momentum in NA61/SHINE, may be an indication of a presence of Bose-Einstein correlations.

A structure that is common for all results, including low-energy NA61/SHINE ones, is a one-dimensional gaussian enhancement (at $\Delta\eta \approx 0$), spreading over a full range of $\Delta\phi$. The structure was interpreted as a result of strings fragmentation [61, 81, 88, 109, 108]. It is visible at all SPS beam momenta as well as in all other experiments whose results are presented in Fig. 4.40. It is, however, barely visible in ALICE (bottom panel). The difference is especially visible when comparing the results from ATLAS, CMS, and ALICE at 7 TeV (right column of third, fourth, and fifth rows).

Another enhancement in away-side ($\Delta\phi \approx \pi$) is visible also in all results. At lower energies it is interpreted more as a result of momentum conservation and resonance decays, while at high energies as an interplay of momentum conservation, resonance decays, and a contribution from particles from opposite jets of di-jets.

In summary, the NA61/SHINE p+p results present two-particle correlation structures in a domain of soft physics, where dominating processes are: momentum conservation, resonance decays, strings fragmentation, and Bose-Einstein correlations.

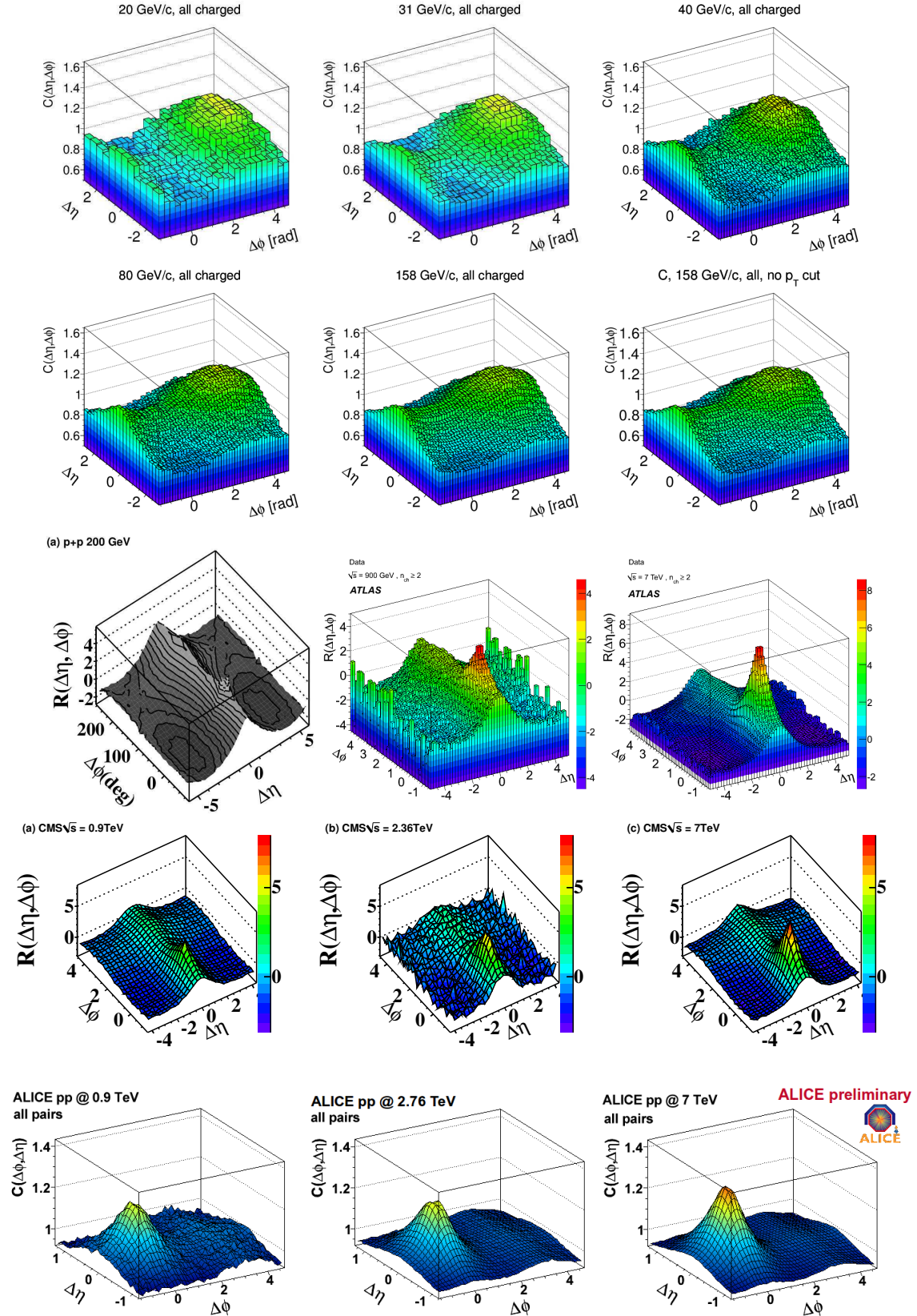


Figure 4.40: Results of inclusive two-particle correlations in pseudorapidity and azimuthal angle in p+p interactions. Juxtaposition for several experiments. NA61/SHINE results in two first rows (158 GeV/c data are shown with and without p_T cut). Third row, from the left: PHOBOS results at 200 GeV [67], ATLAS results at 0.9 and 7 TeV [87]. Fourth row presents CMS results at 0.9, 2.36, and 7 TeV [80]. Fifth row shows ALICE results at 0.9, 2.76, and 7 TeV [89].

Chapter 5

Correlations in Pb+Pb collisions

Correlations in p+p collisions, presented in the previous chapter, were compared with correlations in Pb+Pb data obtained from the NA49 experiment. The NA49 experiment was an ancestor of NA61/SHINE with very similar detector setup (more information in Sec. 3).

5.1 Data sets and cuts

In this analysis Pb+Pb collisions, taken at two beam momenta: 20A and 158A GeV/c, are used. Table 5.1 shows data statistics and datasets used in the analysis.

| p_{beam} [GeV/c] | $\sqrt{s_{NN}}$ [GeV] | Dataset ID | Events used |
|---------------------------|-----------------------|------------|-------------|
| 20 | 6.3 | 03A | 246701 |
| 158 | 17.3 | 00B | 37196 |

Table 5.1: NA49 Pb+Pb data used in the analysis.

Events with good quality were taken to the analysis. They had to satisfy also following conditions:

- The position of the reconstructed main vertex in 158 GeV/c sample had to be located in ranges: $x \in (-0.1, 0.04)$ cm; $y \in (-0.1, 0.13)$ cm; $z \in (-579.2, -578.6)$ cm. The same position in 20 GeV/c sample was restricted to: $x \in (-0.25, 0.2)$ cm; $y \in (-0.2, 0.2)$ cm; $z \in (-581.3, -580.8)$ cm.
- For 158 GeV/c, an additional offline cut on the energy deposited in the VETO calorimeter was applied. Namely, this energy had to be smaller than 10868 GeV which corresponds to 7.2% of the most central Pb+Pb collisions from 10% originally recorded by online trigger. For 20 GeV/c, online trigger was already selecting 7.2% of the most central collisions.
- The number of all tracks outgoing from the main vertex had to be greater than zero and the ratio of the number of tracks used to fit the main vertex to the number of all outgoing tracks had to be greater than 0.25.

In order to reduce the contamination of secondary interactions and non-vertex tracks, the tracks also should satisfy their selection conditions:

- Each non-neutral track should be reconstructed and fitted properly.
- The maximum number of points (the number of potential points that could be left by the track in the detector; calculated from the track geometry) should be at least 30.
- The sum of the number of points left by the track in both VTPCs should be at least 15.
- The ratio of the number of points left by the track in the detector to maximal number of points should be at least 0.5 to eliminate split tracks.
- The distance between the track and reconstructed primary vertex in the target plane should be $|B_x| < 2$ cm and $|B_y| < 1$ cm.
- The products of γ conversion are rejected by dE/dx graphical cut, similar as in p+p analysis (see Sec. 4.1 for details).

The most of event and track cuts were inherited from NA49 analysis of transverse momentum fluctuations [41]. The event cuts were applied to ensure that the interactions were in the target and the vertex reconstruction quality was fine. The tracks cuts were applied to reduce contamination of track from secondary interactions and weak decays. Products of gamma decays were cut out similarly as in p+p data by visual dE/dx cut. One should note that, due to the lack of high statistics Monte Carlo data, Pb+Pb results presented here are not corrected for detector effects.

5.2 Correlation results

5.2.1 Comparison with p+p

The comparisons of Pb+Pb and p+p collisions are presented in Figs. 5.1, 5.2, 5.3, and 5.4. When compared to p+p, the magnitude of correlations in Pb+Pb collisions is about two orders of magnitude smaller. This is probably due to significantly higher track multiplicity in Pb+Pb which dilutes the signal.

Two-particle correlations in $\Delta\eta$ and $\Delta\phi$ in Pb+Pb have different shapes than those in p+p. Correlations in 20A GeV/c data of all charged pairs (Fig. 5.1, right panel) show two enhancements: one in near-side and second one in away-side region. Such hills are barely visible in 158A GeV/c data (middle panel). The near-side hill is rather not observed in p+p data (left panel).

The near-side hill mentioned above is coming mostly from unlike-sign pairs correlations (Fig. 5.2). The shape of plots from Pb+Pb collisions (middle and right panels) are clearly different from p+p (left panel). Here, the near-side hill is very prominent for both Pb+Pb energies. Due to the cut on γ decays it cannot be attributed to e^+e^- pairs. The most probable explanation is the Coulomb attraction of unlikely charged particles.

Correlations of positively charged pairs (Fig. 5.3) are generally similar in both systems with two enhancements at near- and away-side. However, the near-side hill is weaker in

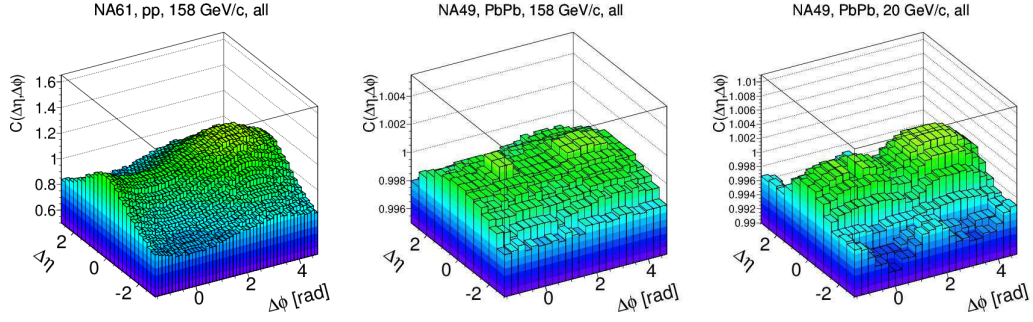


Figure 5.1: Correlation results comparison. Left panel: results for p+p collisions at 158 GeV/c. Middle panel: results for Pb+Pb collisions at 158A GeV/c. Right panel: results for Pb+Pb collisions at 20A GeV/c. All charged pairs. Plots are in different scales on z -axis.

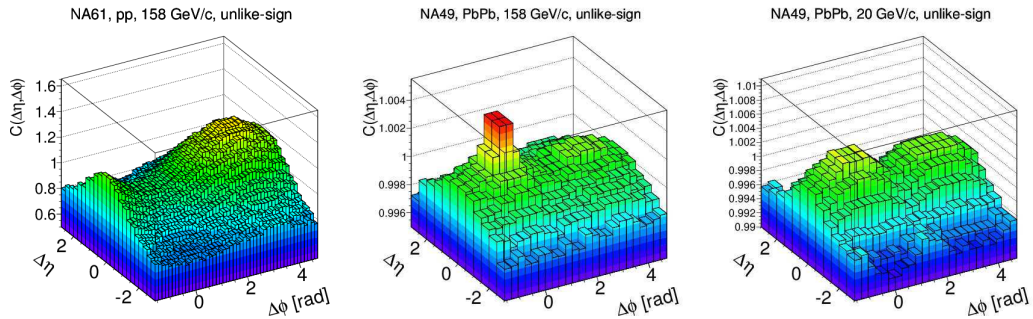


Figure 5.2: Correlation results comparison. Left panel: results for p+p collisions at 158 GeV/c. Middle panel: results for Pb+Pb collisions at 158A GeV/c. Right panel: results for Pb+Pb collisions at 20A GeV/c. Unlike-sign pairs. Plots are in different scales on z -axis.

Pb+Pb whereas the away-side is stronger, especially at 20A GeV/c (right panel). Additionally, local suppression close to $(\Delta\eta, \Delta\phi) = (0, 0)$ bin is present in bigger system for positively charged pairs.

Figure 5.5 shows the same results on correlations in Pb+Pb at 158A GeV/c (as in middle plots of Figs. 5.1, 5.2, 5.3, and 5.4), but on different (vertical) color scale to better show the magnitude of $(\Delta\eta, \Delta\phi) \approx (0, 0)$ suppression for positively charged particles. There are two possible explanations of this suppression. The first one is that it can be an effect of Coulomb repulsion which grows with increasing system size and energy. Another explanation is that information from many tracks traveling very close to each other may not be properly reconstructed due to limited resolution of detector electronics. High density of tracks, produced in high energy collisions of big systems, such as Pb+Pb, may lead to a situation when two tracks, traveling close to each other (with small relative differences in η and ϕ), would be treated in reconstruction as one track (both tracks, traveling through TPCs, will generate ions that will drift to the same readout pad). This may result as a lack of one entry to the correlations histogram. The more such pairs, the less contribution will be put into the region of $(\Delta\eta, \Delta\phi) \approx (0, 0)$. In order to check whether the suppression comes from such two-track resolution effect, an additional analysis was done. It is presented in the following section.

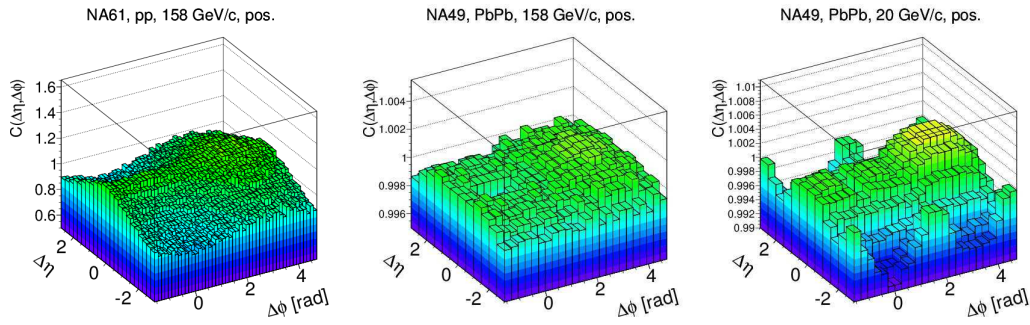


Figure 5.3: Correlation results comparison. Left panel: results for p+p collisions at 158 GeV/c. Middle panel: results for Pb+Pb collisions at 158A GeV/c. Right panel: results for Pb+Pb collisions at 20A GeV/c. Positively charged pairs. Plots are in different scales on z -axis.

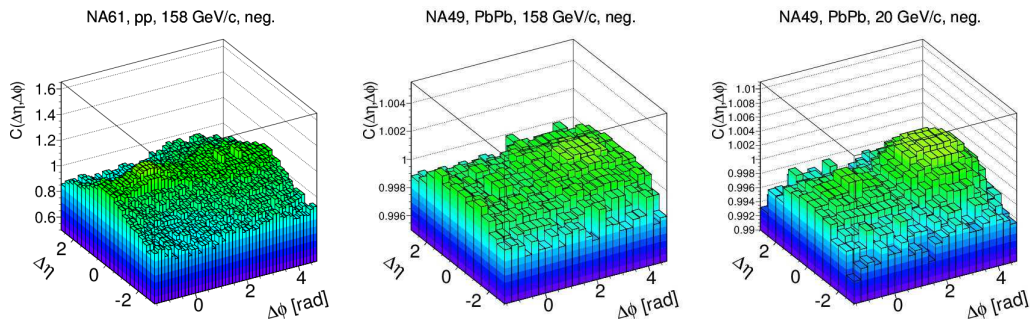


Figure 5.4: Correlation results comparison. Left panel: results for p+p collisions at 158 GeV/c. Middle panel: results for Pb+Pb collisions at 158A GeV/c. Right panel: results for Pb+Pb collisions at 20A GeV/c. Negatively charged pairs. Plots are in different scales on z -axis.

5.2.2 Two-track resolution cut analysis

This section describes two-track resolution (TTR) cut method and the analysis of impact of TTR cut distance on results of Pb+Pb collisions at 158A GeV/c.

Two-track resolution cut method

To make the two-track resolution cut possible, information about positions of each accepted track in several places in the detector were obtained. This was achieved by checking whether the track was registered by each TPC.

Figure 5.6 shows a simple scheme of determination of the average two-track distance d^{TTR} . The cut on d^{TTR} checks if each two tracks from one event travel close to each other through most of the way in TPCs. This is achieved by determining the distance between points of intersection of both tracks at both front and back walls of each TPC chamber. If the average distance d^{TTR} was smaller than a defined value $d_{\text{min}}^{\text{TTR}}$, the cut was applied on the tracks (rejection was done). The cut was applied with two-track distance increasing from 0 to 2 cm. It was done in two modes: rejection of a random track from the pair and rejection of both tracks.

A significant drawback of TTR cut appears as the multiplicity of accepted tracks drops suddenly with increasing $d_{\text{min}}^{\text{TTR}}$. This is presented in Fig. 5.7. The drop is observed even after

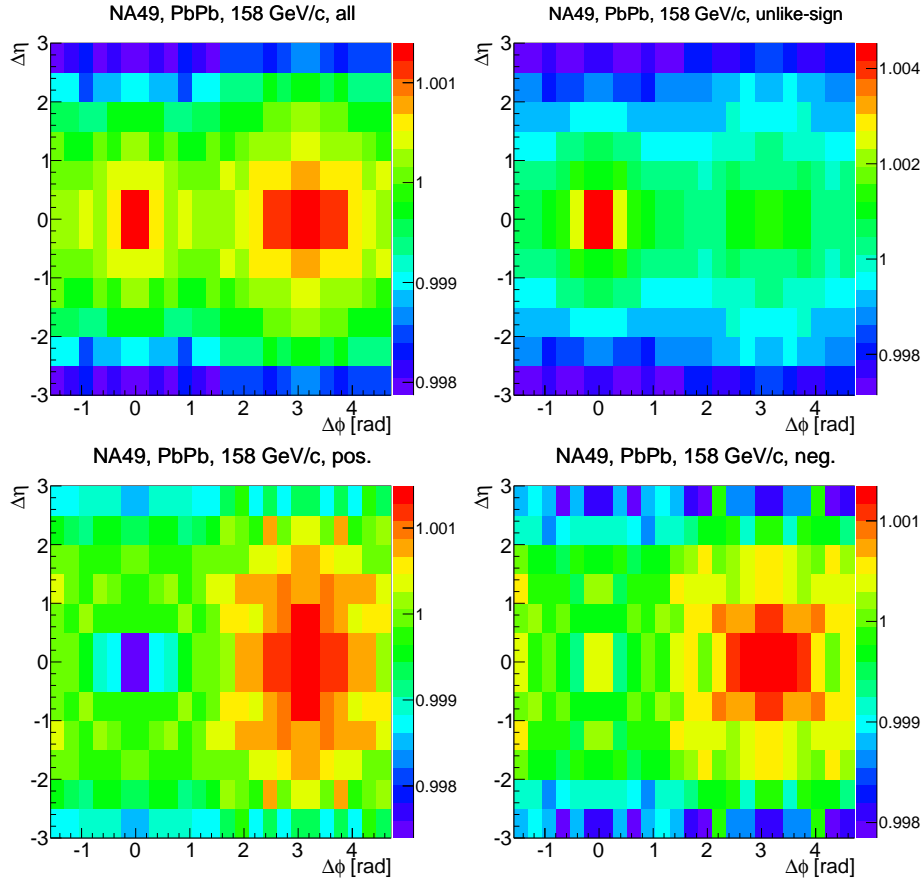


Figure 5.5: Two-particle correlations in Pb+Pb at 158A GeV/c. The results are the same as in Figs. 5.1, 5.2, 5.3, and 5.4 (middle plots) but in different visualization mode to show magnitudes of $(\Delta\eta, \Delta\phi) \approx (0, 0)$ bin in like-sign (bottom panel) pairs.

applying the smallest (0.01 cm) restriction on d^{TT} . Obviously, rejection of both tracks from the pair reduces the multiplicity much more than rejection of one random track.

The analysis of two-particle correlations in Pb+Pb at 158A GeV/c for different $d_{\text{min}}^{\text{TT}}$ cuts was performed for all charge combinations and for two modes of particle rejection. The results for random particle rejection mode are shown in Figs. 5.8, 5.9, 5.10, 5.11 (note non-standard scale on $C(\Delta\eta, \Delta\phi)$ axis). The results for both particles rejection mode are shown in Figs. 5.12, 5.13, 5.14, and 5.15. The distributions are presented for original (unmirrored) layout for a better observation of $(\Delta\eta, \Delta\phi) \approx (0, 0)$ region.

Two-track distance analysis in random particle rejection mode

In general, the distributions do not change for all lower $d_{\text{min}}^{\text{TT}}$ distances (see top rows in Figs. 5.8, 5.9, 5.10, and 5.11). This suggests that, for such $d_{\text{min}}^{\text{TT}}$ values, the correlation structures are due to physical phenomena, not due to two-track resolution effects. For larger $d_{\text{min}}^{\text{TT}}$ values physical conclusions are much less relevant because mean multiplicities are drastically limited and kinematic distributions differ (see also Fig. 5.16).

For all charged pairs (Fig. 5.8) one can notice a large one-dimensional enhancement at higher $\Delta\eta$ values, which emerges for $d_{\text{min}}^{\text{TT}} > 0.1$ cm. This is a result of rejecting particles traveling close to each other, hence with small pseudorapidity differences. Rejection of such particles creates a suppression in this region which, from the other point of view, looks like

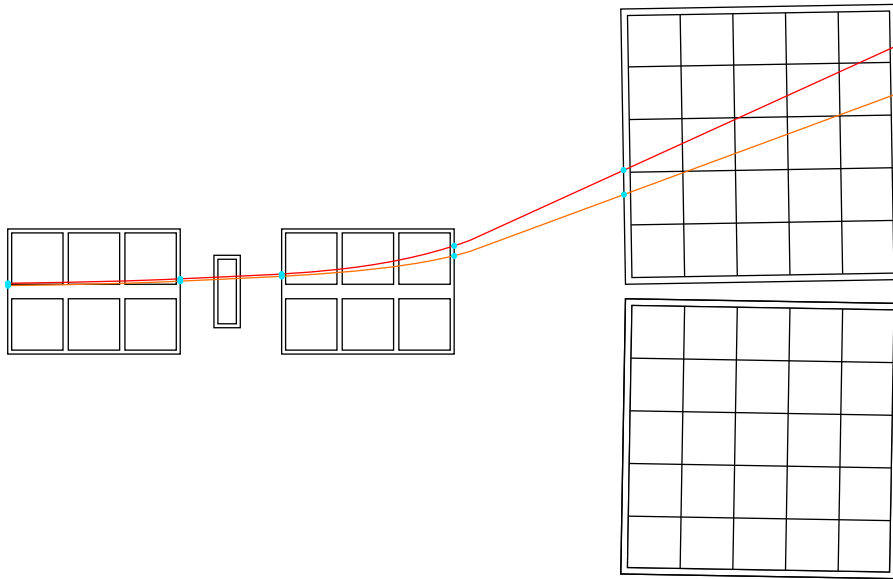


Figure 5.6: Simplified example of determination of the average two-track distance d^{TT} . Cyan circles are the points of intersections between track path and TPC walls perpendicular to the beam (front and back walls). In these points the partial distances between considered tracks are calculated. d^{TT} is the average value of these distances.

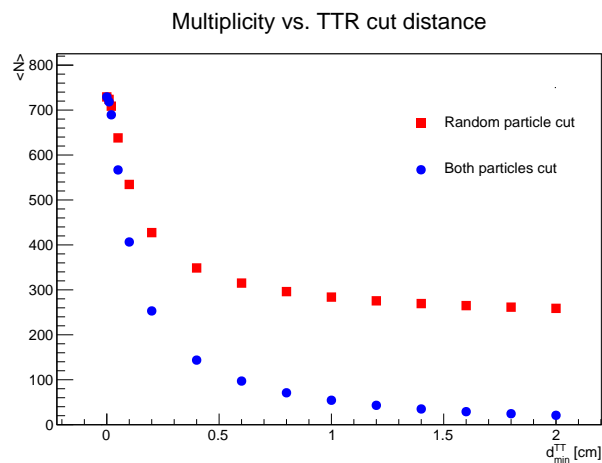


Figure 5.7: Mean multiplicity of accepted tracks as a function of d_{\min}^{TT} . Presented for two modes of TTR cut: rejection of random of two tracks (red boxes) and rejection of both tracks (blue circles). Results for Pb+Pb collisions at 158A GeV/c.

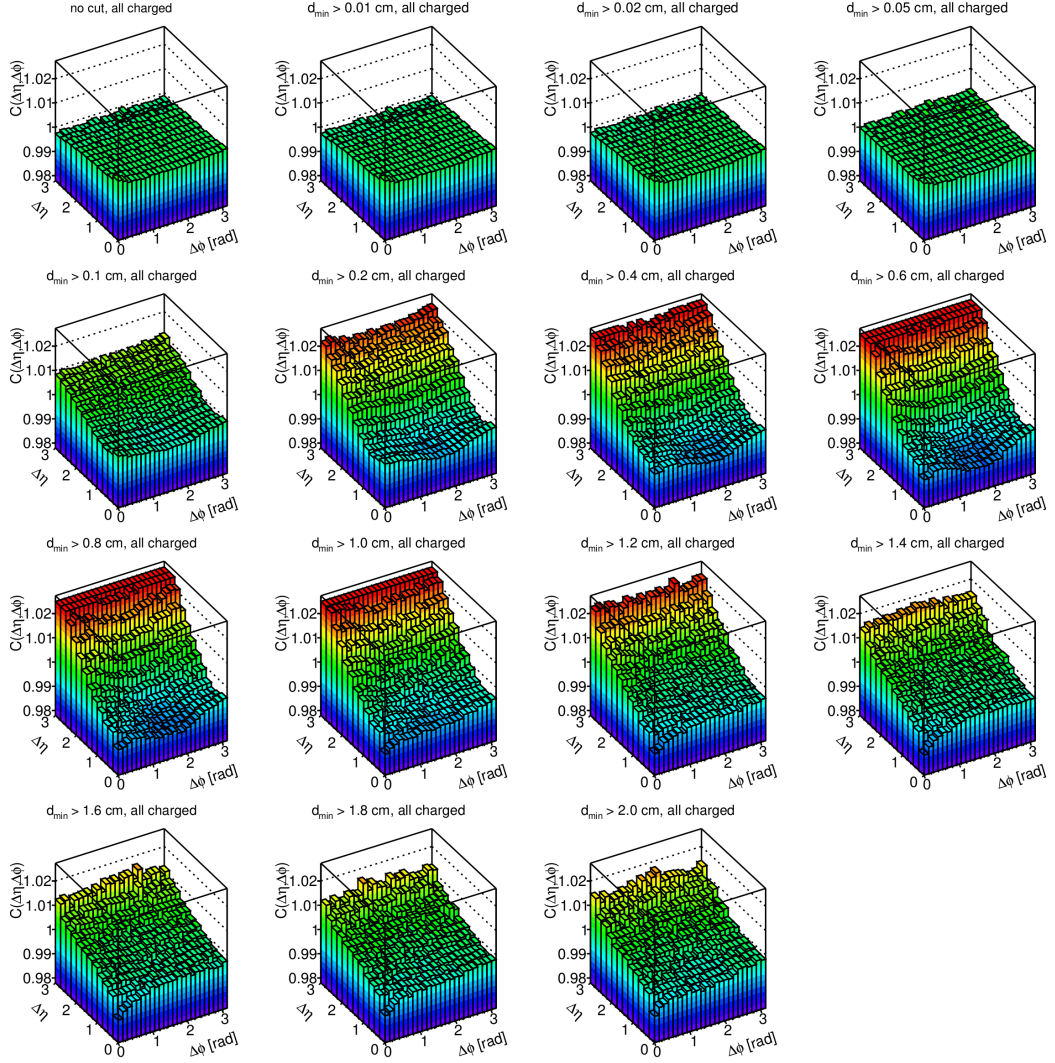


Figure 5.8: Two-particle correlations for different d_{\min}^{TT} distance. d_{\min}^{TT} increases from top-left (no d_{\min}^{TT} restriction) to bottom-right. Results for the mode of rejecting random particle, all charged. Results for Pb+Pb collisions at 158A GeV/c.

an enhancement in region of higher pseudorapidity differences.

The most important structure in unlike-sign pairs (Fig. 5.9) does not disappear with increasing d_{\min}^{TT} . Namely, a peak at $(\Delta\eta, \Delta\phi) = (0, 0)$ is still visible. Its most probable explanation is Coulomb attraction between oppositely charged particles in a pair.

Figure 5.10 presents two-track cut analysis for positively charged pairs. It can be clearly noticed that increasing d_{\min}^{TT} cut does not lead to disappearance of the $(\Delta\eta, \Delta\phi) = (0, 0)$ suppression. Thus, the explanation of Coulomb interactions probably applies also to the correlations of positively charged pairs. A suppression at $(\Delta\eta, \Delta\phi) = (0, 0)$ suggests a presence of Coulomb interactions working in a repulsive way to not allow the positively charged particles travel very close to each other.

On the other hand, the hypothesis of Coulomb repulsion for negatively charged pairs (see Fig. 5.11) may be contrainuitive because of the lack of similar suppression at $(\Delta\eta, \Delta\phi) = (0, 0)$. In fact, one sees a very small enhancement instead. This enhancement may be explained as a result of Bose-Einstein correlations which, for negatively charged pairs, can mask the effect of Coulomb repulsion. The multiplicity of positively charged particles is

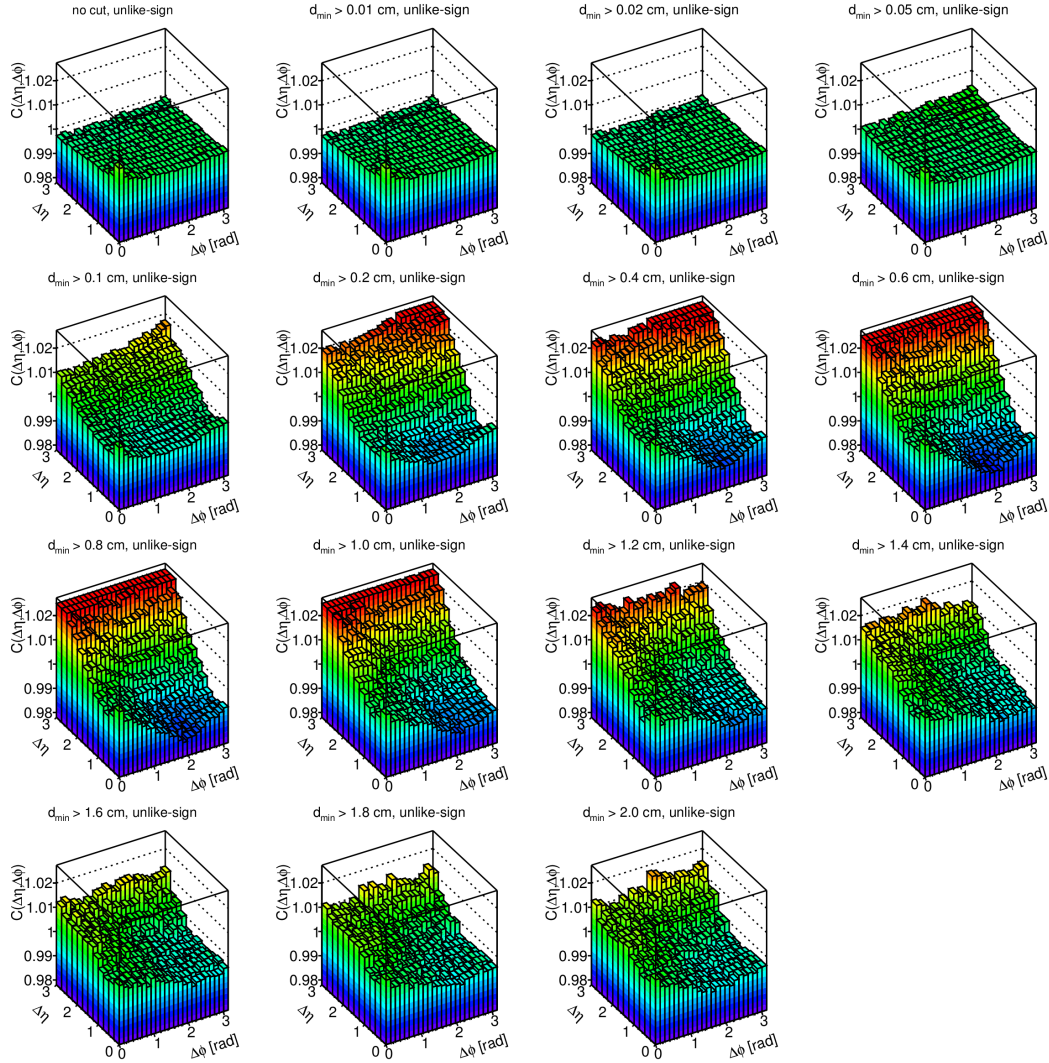


Figure 5.9: Two-particle correlations for different d_{\min}^{TT} distance. d_{\min}^{TT} increases from top-left (no d_{\min}^{TT} restriction) to bottom-right. Results for the mode of rejecting random particle, unlike-sign pairs of particles. Results for Pb+Pb collisions at 158A GeV/c.

higher which may lead to larger number of particles repulsed via Coulomb interactions resulting in a stronger suppression at $C(\Delta\eta, \Delta\phi) = (0, 0)$. The negatively charged particles have smaller multiplicities and thus have weaker suppression which is masked by an enhancement due to Bose-Einstein correlations which appears as a small peak. Such a structure disappears with increasing d_{\min}^{TT} cut and, for stronger restrictions on d_{\min}^{TT} , $C(\Delta\eta, \Delta\phi)$ distributions look qualitatively similar to the distributions for positively charged pairs.

The conclusion is that, close to $(0, 0)$ bin, an interplay between Bose-Einstein correlations and Coulomb interactions occurs which differ between combinations of particles. This opens a way to a deeper analysis of such region which, unfortunately, due to limited time and software problems, could not be continued.

Two-track distance analysis in both particles rejection mode

Results from the analysis in a cut mode rejecting both particles from the pair are shown in Figs. 5.12, 5.13, 5.14, and 5.15. They present different structures than those in a cut

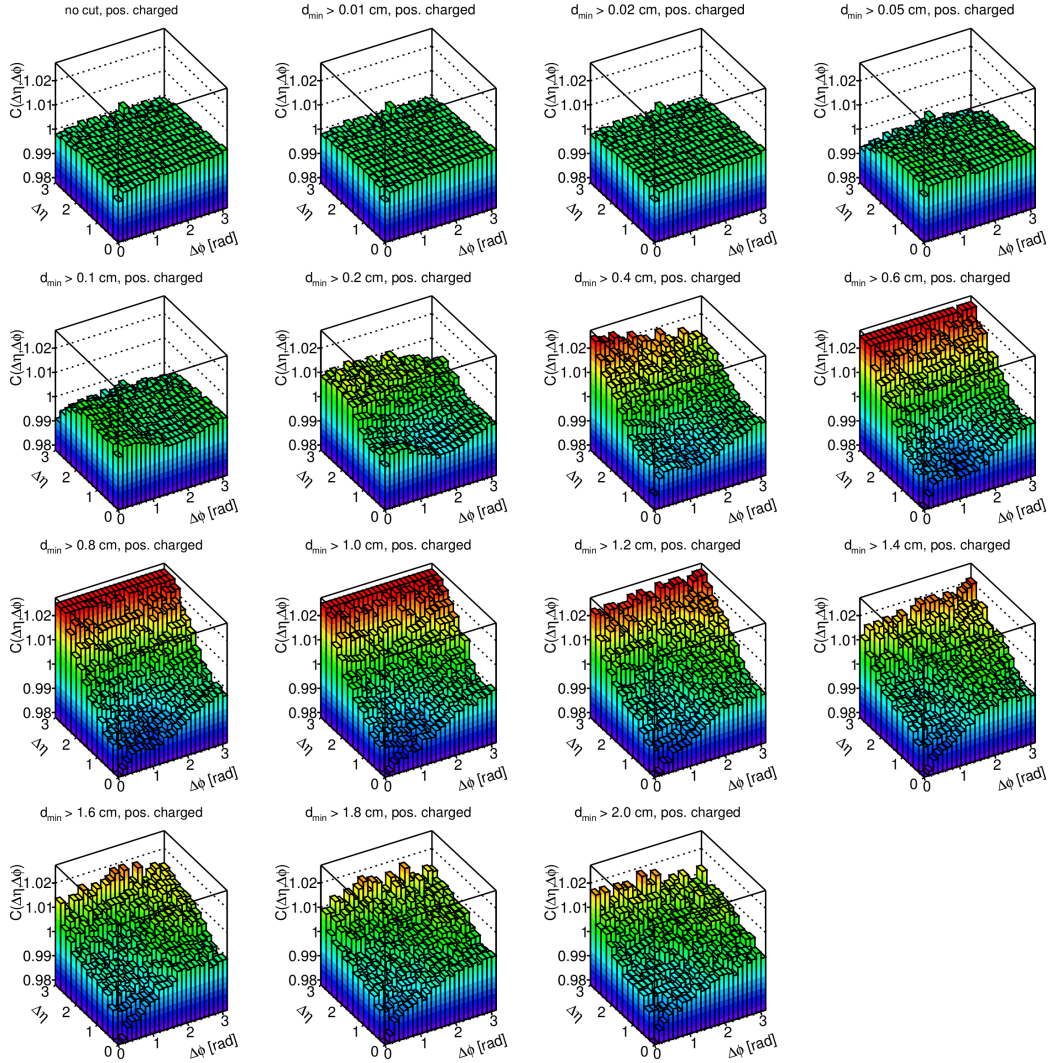


Figure 5.10: Two-particle correlations for different d_{\min}^{TT} distance. d_{\min}^{TT} increases from top-left (no d_{\min}^{TT} restriction) to bottom-right. Results for the mode of rejecting random particle, positively charged pairs. Results for Pb+Pb collisions at 158A GeV/c.

mode rejecting random particle from the pair. Due to removing much more particles, the statistics dramatically drops down with increasing d_{\min}^{TT} cut (see Fig. 5.7). The top panels of the figures are duplicated with a zoom on the vertical scale. The distributions change drastically already after applying the cut on $d_{\min}^{\text{TT}} > 0.05$ cm. In unlike-sign pairs the $(0,0)$ bin peaks over near-side region. A small enhancement at $(\Delta\eta, \Delta\phi) = (0,0)$ in negatively charged pairs disappears for $d_{\min}^{\text{TT}} > 0.05$ cm. A dip for positively charged pairs vanishes for $d_{\min}^{\text{TT}} > 0.1$ cm. This disappearance might be connected with the drop of statistics caused by the very “aggressive” cut that rejects both particles.

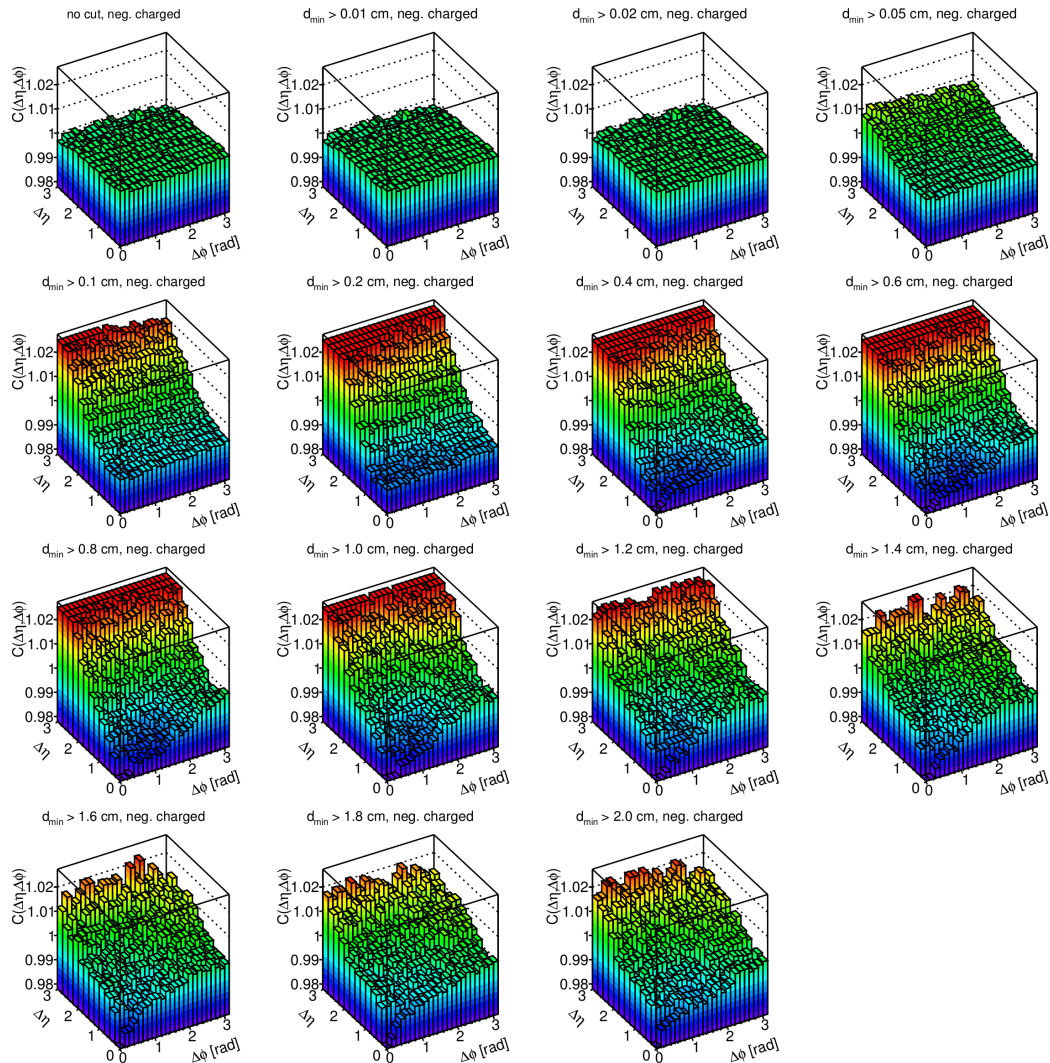


Figure 5.11: Two-particle correlations for different d_{\min}^{TT} distance. d_{\min}^{TT} increases from top-left (no d_{\min}^{TT} restriction) to bottom-right. Results for the mode of rejecting random particle, negatively charged pairs. Results for Pb+Pb collisions at 158A GeV/c.

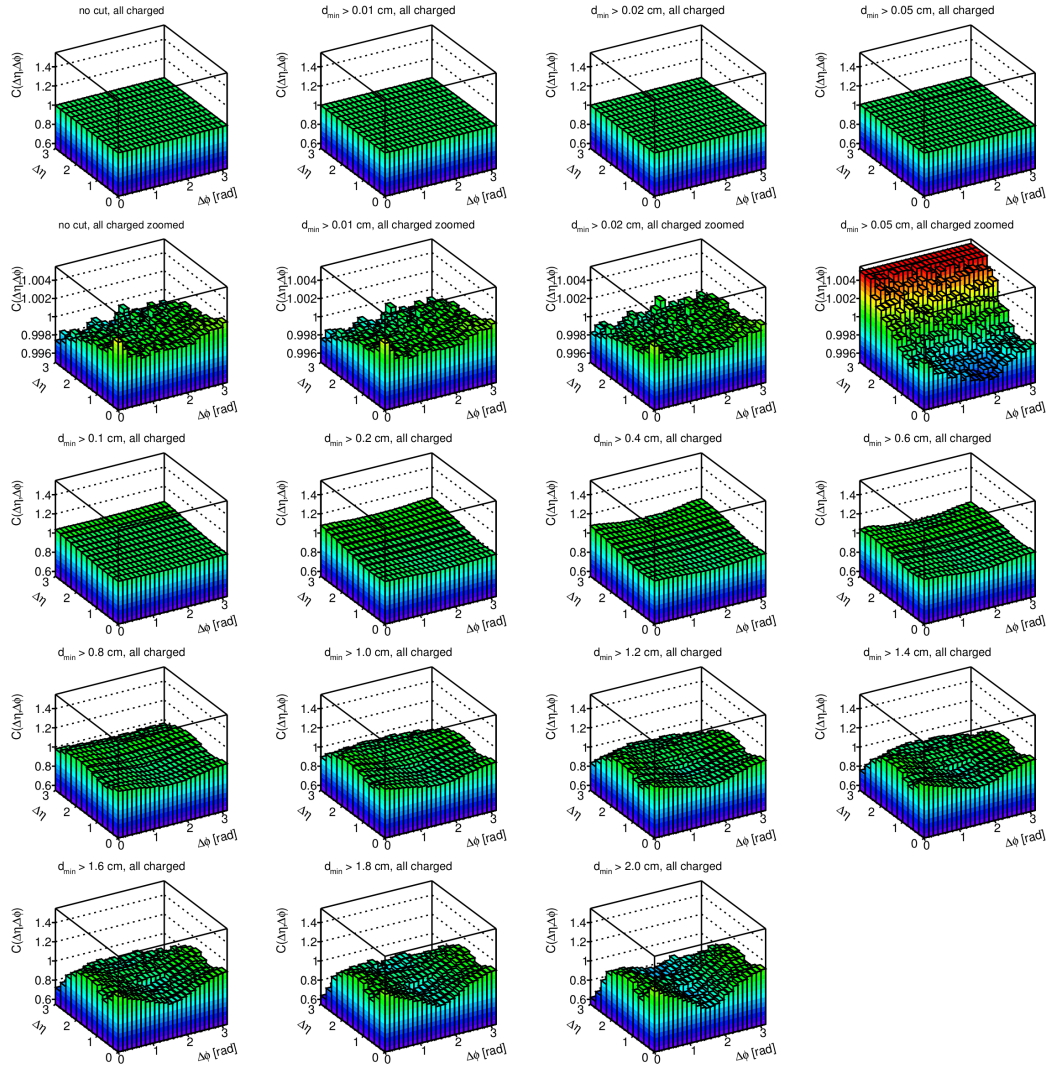


Figure 5.12: Two-particle correlations for different d_{\min}^{TT} distance. d_{\min}^{TT} increases from top-left (no d_{\min}^{TT} restriction) to bottom-right. Results for the mode of rejecting both particles, all charged pairs. Results for Pb+Pb collisions at 158A GeV/c.

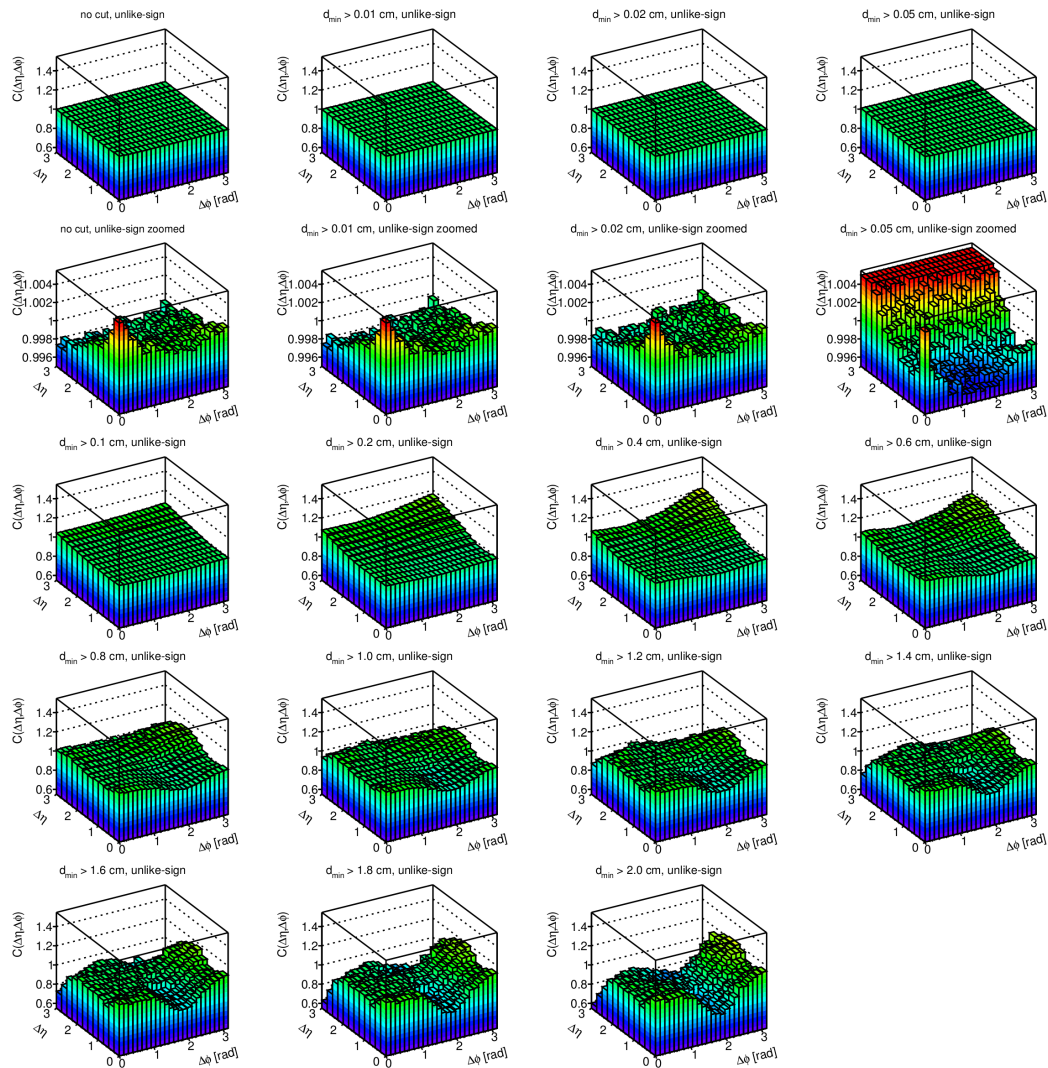


Figure 5.13: Two-particle correlations for different d_{\min}^{TT} distance. d_{\min}^{TT} increases from top-left (no d_{\min}^{TT} restriction) to bottom-right. Results for the mode of rejecting both particles, unlike-sign pairs. Results for Pb+Pb collisions at 158A GeV/c.

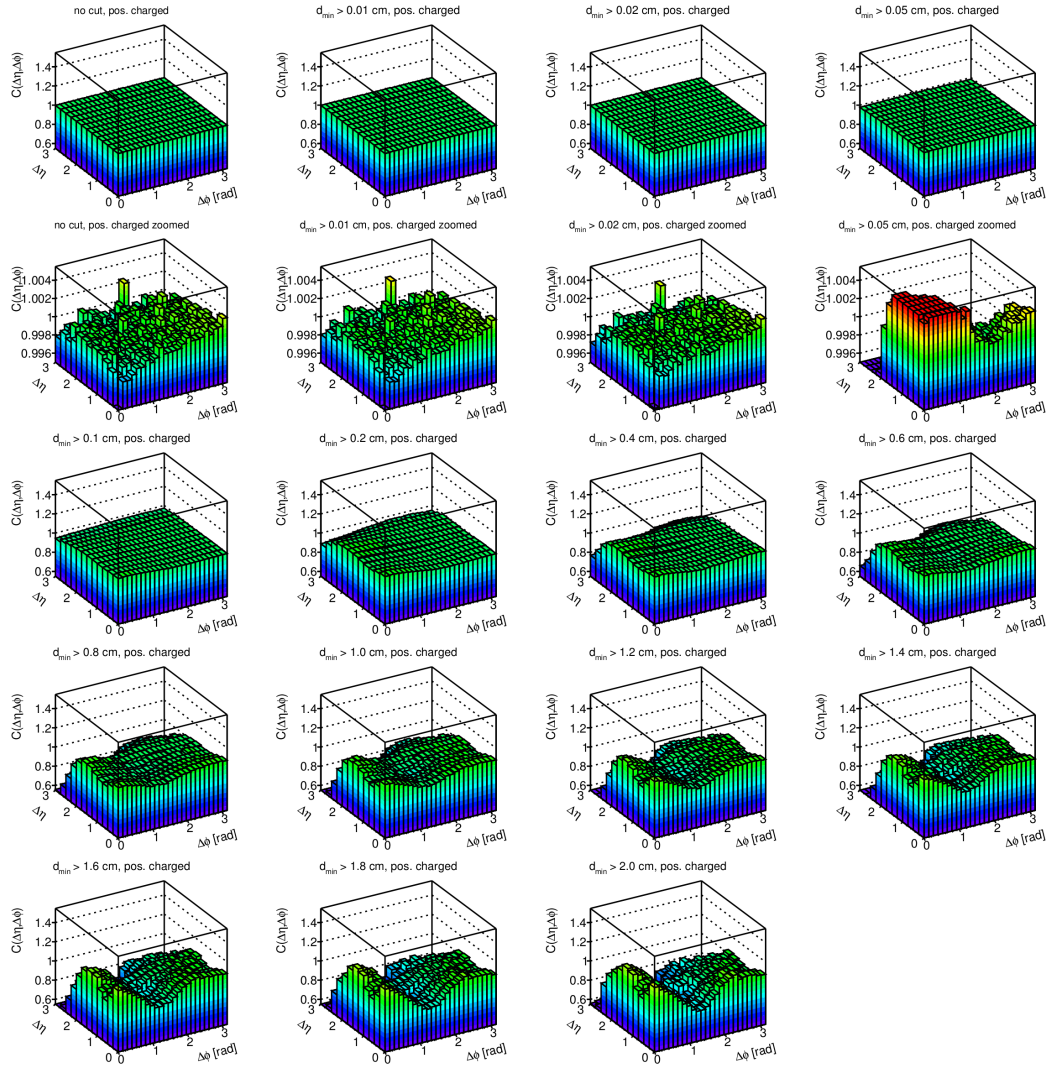


Figure 5.14: Two-particle correlations for different d_{\min}^{TT} distance. d_{\min}^{TT} increases from top-left (no d_{\min}^{TT} restriction) to bottom-right. Results for the mode of rejecting both particles, positively charged pairs. Results for Pb+Pb collisions at 158A GeV/c.

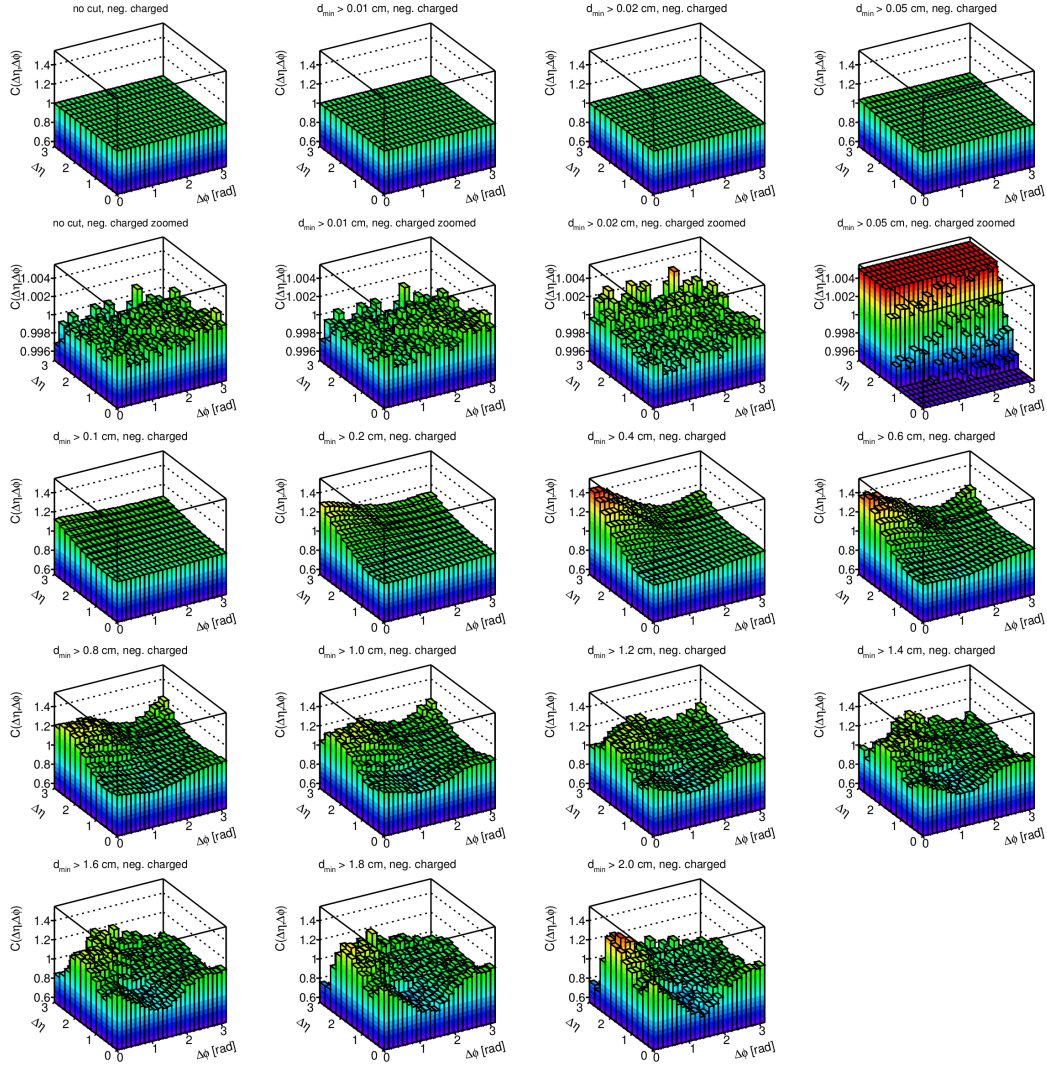


Figure 5.15: Two-particle correlations for different d_{\min}^{TT} distance. d_{\min}^{TT} increases from top-left (no d_{\min}^{TT} restriction) to bottom-right. Results for the mode of rejecting both particles, negatively charged pairs. Results for Pb+Pb collisions at 158A GeV/c.

Conclusions from Pb+Pb analysis

A direct comparison of both particle rejection modes cannot be made because both of them create datasets with very different kinematic distributions. Both cut modes reduce statistics and distort average multiplicities significantly (see Fig. 5.7). Figure 5.16 presents inclusive distributions of pseudorapidity and azimuthal angle without two-track distance cut as well as with the cut $d_{\min}^{\text{TT}} > 1.6$ cm for two particle rejection modes. It can be seen that the azimuthal angle distributions do not change significantly after d_{\min}^{TT} cut application. However, pseudorapidity distributions behave differently. The d_{\min}^{TT} cut in both particles rejection mode dramatically changes the shape of pseudorapidity distribution, whereas the random particle rejection mode preserves the shape of the original distribution. Because of introducing such distortion, even qualitative comparison of the rejection modes cannot be done. In fact, the results for larger values of d_{\min}^{TT} cut (in both particles rejection mode) probably should not be interpreted at all.

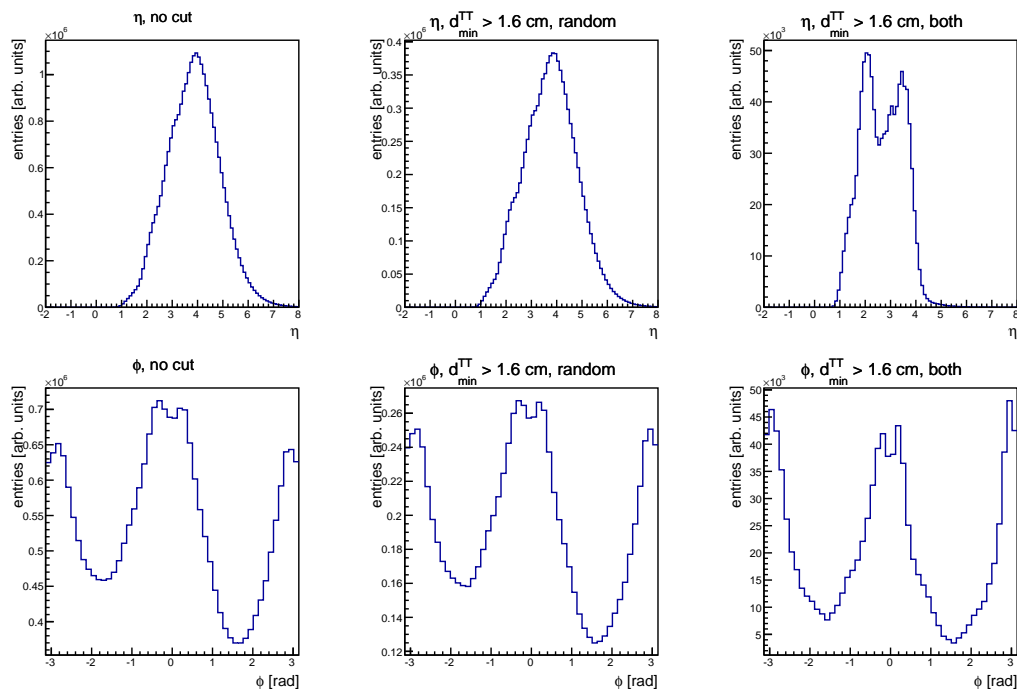


Figure 5.16: Inclusive distributions of pseudorapidity (top row) and azimuthal angle (bottom row) for data without cut on d_{\min}^{TT} (left column), with $d_{\min}^{\text{TT}} > 1.6$ cm in random particle rejection mode (middle column) and with the same cut value in both particles rejection mode (right column).

The analysis of Pb+Pb collisions was performed to compare $\Delta\eta\Delta\phi$ correlations with the results from p+p analysis. However, many difficulties occurred during the analysis caused mainly by very slow analysis of old NA49 data due to the fact that “legacy” software was not compatible with actual CERN software. The analysis for complete statistics and for other SPS energies needed to be suspended, but it should be continued when the old NA49 data are converted into new NA61/SHINE software format. Instead, some additional tests for p+p, not originally planned, were performed. Namely, the analysis of p+p in different multiplicity bins as well as with different minimal p_T cuts were done and presented in this thesis.

Chapter 6

Summary

The results on two-particle correlations in azimuthal angle and pseudorapidity were presented for the energy scan of inelastic p+p collisions obtained by the NA61/SHINE experiment at CERN.

The correlation functions at beam momenta: 20, 31, 40, 80, and 158 GeV/c, corrected for the detector effects and reconstruction inefficiencies, reveal several structures connected with particle correlations. The main structures are:

- An enhancement at $(\Delta\eta, \Delta\phi) \approx (0, \pi)$. It is the most prominent in unlike-sign and all charged, weaker in positively charged pairs, and almost invisible in negatively charged pairs. The charge dependence of this structure is consistent with resonance decays.
- A $\cos(\Delta\phi)$ modulation which appears in all charge combinations as a minimum along $\Delta\eta$ near $\Delta\phi = 0$ and maximum near $\Delta\phi = \pi$. It is stronger in all charged and unlike-sign pairs and weaker in like-sign pairs. The structure appears probably due to momentum conservation.
- A small enhancement at $(\Delta\eta, \Delta\phi) \approx (0, 0)$ in correlations of like-sign pairs. The structure raises with increasing beam momentum in positively charged pairs, whereas in negatively charged pairs it is independent of beam momentum. The enhancement is probably caused by Bose-Einstein statistics.
- A gaussian-like enhancement at $\Delta\eta \approx 0$ in full $\Delta\phi$ range. The probable origin of flux-tube fragmentation was discussed in Sec. 4.4.2.

The inclusive results were compared to theoretical predictions of the EPOS and the UrQMD models. EPOS reproduced data better than UrQMD leaving only a disagreement in near-side $(\Delta\eta, \Delta\phi) \approx (0, 0)$ region where correlations of Bose-Einstein statistics appear – EPOS has no implementation of such phenomenon. The UrQMD model has many disagreements with data visible mostly as an excessive enhancement in away-side region $(\Delta\eta, \Delta\phi) \approx (0, \pi)$. The comparison was also done with the results from inclusive analysis of p+p interactions from other experiments: CMS, ATLAS, ALICE, and PHOBOS. Large differences in the correlation function landscape can be observed as a near-side peak of correlations from hard processes is dominating there.

The aim of this analysis was to study correlations originating mostly from soft processes, thus a restriction on transverse momentum was made: $p_T < 1.5$ GeV/c. However, an additional analysis without p_T cut was performed and it showed that no correlations from hard processes are visible or they are indistinguishable from already observed correlation structures.

A semi-inclusive analysis was also done in several multiplicity bins of inelastic p+p collisions at 158 GeV/c. It was observed, that the correlation structures are the most prominent in the lowest multiplicity bin and they are more diluted with increasing multiplicity in the bin.

A primordial analysis was performed also on Pb+Pb collisions at 20A and 158A GeV/c which were recorded by the NA49 experiment at CERN. The results shown structures different than in p+p interactions. Two structures were observed for Pb+Pb in $(\Delta\eta, \Delta\phi) \approx (0, 0)$: an enhancement for unlike-sign and a suppression for positively charged pairs. Due to probable problem with merged tracks, a study of the correlations versus two-track minimal distance was performed. The structures stay for a reasonable range of the cut on two-track minimal distance. This may suggest that Coulomb interactions are responsible for the enhancement for unlike-sign pairs and the suppression for positively charged particles at $(\Delta\eta, \Delta\phi) \approx (0, 0)$ region. However, further investigations (i.e. for higher statistics, for remaining SPS energies, more studies of the visible structures) are required in this analysis.

Bibliography

- [1] S. Weinberg. The making of the Standard Model. *Eur.Phys.J.*, C34:5–13, 2004. [cited on page 4]
- [2] M. Gell-Mann. A schematic model of baryons and mesons. *Phys. Lett.*, 8:214–215, 1964. [cited on page 4]
- [3] G. Zweig. An SU_3 model for strong interaction symmetry and its breaking. Version 1. 1964. [cited on page 4]
- [4] M. Breidenbach et al. Observed Behavior of Highly Inelastic Electron-Proton Scattering. *Phys. Rev. Lett.*, 23:935–939, 1969. [cited on page 4]
- [5] <http://www.kheper.net/cosmos/universe/CosmicTimeline.jpg>. [cited on page 5]
- [6] I. K. Yoo. Bose-Einstein Correlations of Charged Kaons and Pions in Central Pb+Pb Collisions at 158 AGeV. PhD. thesis. 2001. [cited on page 6]
- [7] J. C. Collins and M. J. Perry. Superdense Matter: Neutrons or Asymptotically Free Quarks? *Phys.Rev.Lett.*, 34:1353, 1975. [cited on page 5]
- [8] E. V. Shuryak. Quantum chromodynamics and the theory of superdense matter. *Phys.Rept.*, 61:71–158, 1980. [cited on page 5]
- [9] A. Bazavov et al. Equation of state in $(2 + 1)$ -flavor QCD. *Phys. Rev.*, D90:094503, 2014. [cited on page 6]
- [10] FAIR official information brochure. <http://www.fair-center.eu/public/information-material/publications.html>. [cited on page 7]
- [11] Nuclotron-based Ion Collider fAcility (NICA) website. <http://nica.jinr.ru/physics.php>. [cited on page 7]
- [12] NA61/SHINE pictures library. [cited on page 8]
- [13] Z. Fodor and S. D. Katz. Critical point of QCD at finite T and μ , lattice results for physical quark masses. *JHEP*, 04:050, 2004. [cited on page 8]
- [14] A. Li et al. Lattice calculation of QCD critical point with the canonical ensemble, 2011. talk at the RIKEN-BNL Workshop On Fluctuations, Correlations and RHIC Low Energy Runs, <http://quark.phy.bnl.gov/~htding/fcrworkshop/Liu.pdf> . [cited on page 8]
- [15] S. Datta et al. The QCD Critical Point: marching towards continuum. *Nucl.Phys.*, A904-905:883c–886c, 2013. [cited on page 8]
- [16] G. Endrodi et al. The QCD phase diagram at nonzero quark density. *JHEP*, 1104:001, 2011. [cited on page 8]

- [17] P. de Forcrand and O. Philipsen. The chiral critical line of $N_f = 2+1$ QCD at zero and non-zero baryon density. *JHEP*, 0701:077, 2007. [cited on page 8]
- [18] J. Rafelski and B. Muller. Strangeness Production in the Quark-Gluon Plasma. *Phys.Rev.Lett.*, 48:1066, 1982. [cited on page 9]
- [19] J. Baechler et al. Strangeness enhancement in central S + S collisions at 200 GeV/nucleon. *Nucl. Phys.*, A525:221C–226C, 1991. [cited on page 9]
- [20] M. Gaździcki et al. Neutral strange particle production in S-S collisions at 200 GEV/nucleon. *Nucl. Phys.*, A498:375C–384C, 1989. [,647(1989)]. [cited on page 9]
- [21] E. Andersen et al. Strangeness enhancement at mid-rapidity in Pb-Pb collisions at 158 A GeV/c. *Phys. Lett.*, B449:401–406, 1999. [cited on page 9]
- [22] T. Matsui and H. Satz. J/ψ suppression by quark-gluon plasma formation. *Phys.Lett.*, B178:416, 1986. [cited on page 9]
- [23] M. C. Abreu et al. Anomalous J/ψ suppression in Pb-Pb interactions at 158 GeV/c per nucleon. *Phys.Lett.*, B410:337–343, 1997. [cited on page 9]
- [24] R. Arnaldi et al. Dimuon and charm production in In+In collisions at the CERN SPS. *Nucl.Phys.*, A774:67–76, 2006. [cited on page 9]
- [25] A. Adare et al. J/ψ suppression at forward rapidity in Au + Au collisions at $\sqrt{s_{NN}} = 200$ GeV. *Phys.Rev.*, C84:054912, 2011. [cited on page 9]
- [26] B. B. Abelev et al. Centrality, rapidity and transverse momentum dependence of J/ψ suppression in Pb–Pb collisions at $\sqrt{s_{NN}} = 2.76$ TeV. *Phys. Lett.*, B734:314–327, 2014. [cited on page 9]
- [27] R. Stock. Relativistic Nucleus-Nucleus Collisions and the QCD Matter Phase Diagram. 2008. [cited on page 9]
- [28] A. Adare et al. Centrality dependence of low-momentum direct-photon production in Au + Au collisions at $\sqrt{s_{NN}} = 200$ GeV. *Phys. Rev.*, C91(6):064904, 2015. [cited on page 9]
- [29] J. Adam et al. Direct photon production in Pb-Pb collisions at $\sqrt{s_{NN}} = 2.76$ TeV. *Phys. Lett.*, B754:235–248, 2016. [cited on page 9]
- [30] J. D. Bjorken. Energy Loss of Energetic Partons in Quark-Gluon Plasma: Possible Extinction of High p_T Jets in Hadron-Hadron Collisions. Technical Report FERMILAB-PUB-82-59-THY, FERMILAB, Batavia, IL, Aug 1982. [cited on page 9]
- [31] J. Adams et al. Evidence from $d+Au$ Measurements for Final-State Suppression of High- p_T Hadrons in Au + Au Collisions at RHIC. *Phys.Rev.Lett.*, 91:072304, 2003. [cited on page 9, 10]
- [32] A. Adare et al. Scaling properties of azimuthal anisotropy in Au + Au and Cu + Cu collisions at $\sqrt{s_{NN}} = 200$ GeV. *Phys. Rev. Lett.*, 98:162301, 2007. [cited on page 11]
- [33] M. Gaździcki and M. I. Gorenstein. On the Early Stage of Nucleus–Nucleus Collisions. *Acta Phys. Polon.*, B30:2705, 1999. [cited on page 12]
- [34] K. Grebieszko. News from strong interactions program of the NA61/SHINE experiment. In *10th International Workshop on Critical Point and Onset of Deconfinement (CPOD 2016) Wrocław, Poland, May 30-June 4, 2016*, 2016, arXiv:1608.01538. [cited on page 13, 14]
- [35] S. Puławski. Energy dependence of hadron spectra and multiplicities in p+p interactions. *PoS*, CPOD2014:010, 2015. [cited on page 14]
- [36] The NA49 experiment website. <http://na49info.web.cern.ch/na49info/>. [cited on page 13, 37]

- [37] C. Alt et al. Pion and kaon production in central Pb+Pb collisions at 20A and 30A GeV: Evidence for the onset of deconfinement. *Phys.Rev.*, C77:024903, 2008. [cited on page 13]
- [38] S. V. Afanasiev et al. Energy dependence of pion and kaon production in central Pb + Pb collisions. *Phys. Rev.*, C66:054902, 2002. [cited on page 13]
- [39] M. A. Stephanov, K. Rajagopal, and E. V. Shuryak. Event-by-event fluctuations in heavy ion collisions and the QCD critical point. *Phys.Rev.*, D60:114028, 1999. [cited on page 13]
- [40] T. Anticic et al. Transverse momentum fluctuations in nuclear collisions at 158-A-GeV. *Phys. Rev.*, C70:034902, 2004. [cited on page 13]
- [41] T. Anticic et al. Energy dependence of transverse momentum fluctuations in Pb + Pb collisions at the CERN Super Proton Synchrotron (SPS) at 20A to 158A GeV. *Phys. Rev.*, C79:044904, 2009. [cited on page 13, 92]
- [42] C. Alt et al. Centrality and system size dependence of multiplicity fluctuations in nuclear collisions at 158-A/GeV. *Phys. Rev.*, C75:064904, 2007. [cited on page 13]
- [43] C. Alt et al. Energy Dependence of Multiplicity Fluctuations in Heavy Ion Collisions at the CERN SPS. *Phys. Rev.*, C78:034914, 2008. [cited on page 13]
- [44] K. Grebieszko. Search for the critical point of strongly interacting matter in NA49. *Nucl. Phys.*, A830:547C–550C, 2009. [cited on page 13]
- [45] T. Anticic et al. Measurement of event-by-event transverse momentum and multiplicity fluctuations using strongly intensive measures $\Delta[P_T, N]$ and $\Sigma[P_T, N]$ in nucleus-nucleus collisions at the CERN Super Proton Synchrotron. *Phys. Rev.*, C92(4):044905, 2015. [cited on page 13]
- [46] A. Aduszkiewicz et al. Multiplicity and transverse momentum fluctuations in inelastic proton-proton interactions at the CERN Super Proton Synchrotron. 2015, arXiv:1510.00163. [cited on page 13]
- [47] T. Czopowicz. Transverse momentum and multiplicity fluctuations in Be+Be energy scan from NA61/SHINE. *PoS*, CPOD2014:054, 2015. [cited on page 13]
- [48] Ł. Graczykowski and M. Janik. Angular correlations of identified charged particles measured in pp collisions by ALICE at the LHC. *Nucl. Phys.*, A926:205–212, 2014. [cited on page 17, 33, 35]
- [49] K. G. Wilson. Some Experiments on Multiple Production. 1970. [cited on page 17, 117]
- [50] W. Ko. Rapidity Correlations between the Negative Pions Produced in the K^+p Interaction. *Phys.Rev.Lett.*, 28:935–938, 1972. [cited on page 17, 117]
- [51] R. Singer et al. Two-particle rapidity correlations in 205 GeV/c pp interactions. *Phys.Lett.*, B49:481, 1974. [cited on page 17]
- [52] C. Bromberg et al. Pion production in pp collisions at 102 GeV/c. *Phys.Rev.*, D9:1864–1871, 1974. [cited on page 17]
- [53] W. Ko et al. Like- and Unlike-Charged Pion Correlations in π^+p and pp Interactions at 100 GeV/c. *Phys.Rev.Lett.*, 33:1443, 1974. [cited on page 17, 18]
- [54] G. Bellettini. Large angle acceptance experiment at the ISR. *eConf*, C720906V1:279–285, 1972. [cited on page 17]
- [55] H. Dibon et al. Rapidity correlations in inclusive two-particle production at storage ring energies. *Phys.Lett.*, B44:313–316, 1973. [cited on page 17, 18]

- [56] K. Fiałkowski. A simple explanation of correlation data in inclusive pp interactions at high energy. *Phys.Lett.*, B41:379–382, 1972. [cited on page 18]
- [57] P. Pirila and S. Pokorski. Two-particle correlations at ISR energies with diffraction and pionization. *Phys.Lett.*, B43:502, 1973. [cited on page 18]
- [58] A. Białas, K. Fiałkowski, and K. Zalewski. Two-particle correlation length in fireball models. *Phys.Lett.*, B45:337–339, 1973. [cited on page 18]
- [59] K. Eggert et al. Angular correlations between the charged particles produced in pp collisions at ISR energies. *Nucl.Phys.*, B86:201, 1975. [cited on page 18, 19, 23, 117]
- [60] B. Y. Oh et al. Two Particle Correlations in the Central Region of pp and π^-p Interactions at 100–300 GeV/c. *Phys.Lett.*, B56:400, 1975. [cited on page 18, 19, 20, 118]
- [61] R. J. Porter and T. A. Trainor. Soft and hard components of two-particle distributions on (y_t, η, ϕ) from p-p collisions at $\sqrt{s} = 200$ GeV. In *Ultra-relativistic nucleus-nucleus collisions. Proceedings, 17th International Conference, Quark Matter 2004, Oakland, USA, January 11-17, 2004*, 2004. [cited on page 20, 21, 89, 119]
- [62] J. Adams et al. Minijet deformation and charge-independent angular correlations on momentum subspace (η, ϕ) in Au-Au collisions at $\sqrt{s_{NN}} = 130$ GeV. *Phys.Rev.*, C73:064907, 2006. [cited on page 21]
- [63] G. Agakishiev et al. Anomalous centrality evolution of two-particle angular correlations from Au-Au collisions at $\sqrt{s_{NN}} = 62$ and 200 GeV. *Phys.Rev.*, C86:064902, 2012. [cited on page 22, 119]
- [64] L. Adamczyk et al. Di-hadron correlations with identified leading hadrons in 200 GeV Au + Au and d + Au collisions at STAR. *Phys. Lett.*, B751:233–240, 2015. [cited on page 23]
- [65] L. Song. The ridge and di-hadron correlations from the beam energy scan. Slides from Quark Matter 2015. Kobe, Japan, 2015. [cited on page 23]
- [66] B. Alver et al. Cluster properties from two-particle angular correlations in p + p collisions at $\sqrt{s} = 200$ and 410 GeV. *Phys.Rev.*, C75:054913, 2007. [cited on page 23, 24, 119]
- [67] B. Alver et al. System size dependence of cluster properties from two-particle angular correlations in Cu+Cu and Au+Au collisions at $\sqrt{s_{NN}} = 200$ GeV. *Phys.Rev.*, C81:024904, 2010. [cited on page 23, 24, 90]
- [68] S. Chatrchyan et al. Centrality dependence of dihadron correlations and azimuthal anisotropy harmonics in PbPb collisions at $\sqrt{s_{NN}} = 2.76$ TeV. *Eur. Phys. J.*, C72:2012, 2012. [cited on page 24, 25, 120]
- [69] G. Aad et al. Measurement of the azimuthal anisotropy for charged particle production in $\sqrt{s_{NN}} = 2.76$ TeV Pb+Pb collisions with the ATLAS detector. *Phys. Rev.*, C86:014907, 2012. [cited on page 26, 120]
- [70] J. F. Grosse-Oetringhaus. Hadron Correlations Measured with ALICE. *Nucl. Phys.*, A910:58–64, 2013. [cited on page 27, 121]
- [71] K. Aamodt et al. Harmonic decomposition of two-particle angular correlations in Pb-Pb collisions at $\sqrt{s_{NN}} = 2.76$ TeV. *Phys. Lett.*, B708:249–264, 2012. [cited on page 27]
- [72] S. Chatrchyan et al. Observation of long-range near-side angular correlations in pPb collisions at the LHC. *Phys.Lett.*, B718:795–814, 2013. [cited on page 27, 28, 120]
- [73] M. Aaboud et al. Measurements of long-range azimuthal anisotropies and associated Fourier coefficients for pp collisions at $\sqrt{s} = 5.02$ and 13 TeV and p+Pb collisions at $\sqrt{s_{NN}} = 5.02$ TeV with the ATLAS detector. 2016, arXiv:1609.06213. [cited on page 27, 28, 31, 32]

- [74] G. Aad et al. Observation of Associated Near-Side and Away-Side Long-Range Correlations in $\sqrt{s_{NN}} = 5.02$ TeV Proton-Lead Collisions with the ATLAS Detector. *Phys. Rev. Lett.*, 110(18):182302, 2013. [cited on page 27, 28, 120]
- [75] G. Aad et al. Measurement of long-range pseudorapidity correlations and azimuthal harmonics in $\sqrt{s_{NN}} = 5.02$ TeV proton-lead collisions with the ATLAS detector. *Phys. Rev. C*, 90:044906, Oct 2014. [cited on page 27]
- [76] R. Aaij et al. Measurements of long-range near-side angular correlations in $\sqrt{s_{NN}} = 5$ TeV proton-lead collisions in the forward region. *Phys. Lett.*, B762:473–483, 2016. [cited on page 29]
- [77] B. Abelev et al. Long-range angular correlations on the near and away side in p-Pb collisions at $\sqrt{s_{NN}} = 5.02$ TeV. *Phys. Lett.*, B719:29–41, 2013. [cited on page 29, 121]
- [78] K. Dusling and R. Venugopalan. Evidence for BFKL and saturation dynamics from dihadron spectra at the LHC. *Phys. Rev.*, D87(5):051502, 2013. [cited on page 30]
- [79] K. Dusling and R. Venugopalan. Explanation of systematics of CMS p + Pb high multiplicity di-hadron data at $\sqrt{s_{NN}} = 5.02$ TeV. *Phys. Rev.*, D87(5):054014, 2013. [cited on page 30]
- [80] V. Khachatryan et al. Observation of long-range, near-side angular correlations in proton-proton collisions at the LHC. *JHEP*, 1009:091, 2010. [cited on page 30, 31, 90, 120]
- [81] The CMS Collaboration. Two-Particle Angular Correlations and Cluster Properties in pp Collisions at $\sqrt{s} = 0.9, 2.36$ and 7 TeV. *CMS-PAS-QCD-10-002*, 2010. [cited on page 30, 89]
- [82] V. Khachatryan et al. Measurement of Long-Range Near-Side Two-Particle Angular Correlations in pp Collisions at $\sqrt{s} = 13$ TeV. *Phys. Rev. Lett.*, 116(17):172302, 2016. [cited on page 30, 31, 120]
- [83] A. Dumitru et al. Glasma flux tubes and the near side ridge phenomenon at RHIC. *Nucl. Phys.*, A810:91–108, 2008. [cited on page 30]
- [84] K. Dusling et al. Long range two-particle rapidity correlations in A + A collisions from high energy QCD evolution. *Nucl. Phys.*, A836:159–182, 2010. [cited on page 30]
- [85] P. Bożek and W. Broniowski. Collective dynamics in high-energy proton-nucleus collisions. *Phys. Rev.*, C88(1):014903, 2013. [cited on page 30]
- [86] P. Bożek, A. Bzdak, and V. Skokov. The rapidity dependence of the average transverse momentum in p + Pb collisions at the LHC: The Color Glass Condensate versus hydrodynamics. *Phys. Lett.*, B728:662–665, 2014. [cited on page 30]
- [87] G. Aad et al. Measurement of inclusive two-particle angular correlations in pp collisions with the ATLAS detector at the LHC. *JHEP*, 1205:157, 2012. [cited on page 30, 32, 90, 120]
- [88] G. Aad et al. Observation of Long-Range Elliptic Azimuthal Anisotropies in $\sqrt{s} = 13$ and 2.76 TeV pp Collisions with the ATLAS Detector. *Phys. Rev. Lett.*, 116(17):172301, 2016. [cited on page 31, 32, 89, 120]
- [89] M. Janik. $\Delta\eta\Delta\phi$ angular correlations in pp collisions at the LHC registered by the ALICE experiment. *PoS, WPCF2011:026*, 2011. [cited on page 33, 34, 90, 121]
- [90] M. Janik, private communication. [cited on page 35]
- [91] R. D. Field and R. P. Feynman. A Parametrization of the Properties of Quark Jets. *Nucl. Phys.*, B136:1, 1978. [cited on page 35]
- [92] M. Althoff et al. Evidence for local compensation of baryon number in e^+e^- annihilation. *Phys. Lett.*, B139:126–132, 1984. [cited on page 35]

- [93] H. Aihara et al. Study of baryon correlations in e^+e^- annihilation at 29 GeV. *Phys. Rev. Lett.*, 57:3140, 1986. [cited on page 35]
- [94] N. Abgrall et al. NA61/SHINE facility at the CERN SPS: beams and detector system. *JINST*, 9:P06005, 2014. [cited on page 37, 39, 40, 45]
- [95] F. Becattini, J. Manninen, and M. Gazdzicki. Energy and system size dependence of chemical freeze-out in relativistic nuclear collisions. *Phys. Rev.*, C73:044905, 2006. [cited on page 38]
- [96] NA61/SHINE website. <https://na61.web.cern.ch/na61/>. [cited on page 37]
- [97] S. Johnson. Hadron Production Measurements for Fermilab Neutrino Beams. Technical Report CERN-SPSC-2014-032. SPSC-P-330-ADD-7, CERN, Geneva, Oct 2014. [cited on page 37]
- [98] <http://te-epc-lpc.web.cern.ch/te-epc-lpc/machines/lhc/general.stm>. [cited on page 39]
- [99] SHINE Offline Framework website. <https://twiki.cern.ch/twiki/bin/view/NA61/SHINEOfflineHome>. [cited on page 41]
- [100] N. Abgrall et al. Report No. CERN-SPSC-2008-018. Technical report, NA61/SHINE Collaboration, 2008. [cited on page 41]
- [101] <http://na49info.web.cern.ch/na49info/na49/Software/DSPACK/>. [cited on page 41]
- [102] <https://na61bq.web.cern.ch/na61bq/pages/root61/>. [cited on page 41]
- [103] K. Werner, F.-M. Liu, and T. Pierog. Parton ladder splitting and the rapidity dependence of transverse momentum spectra in deuteron-gold collisions at the BNL Relativistic Heavy Ion Collider. *Phys.Rev.*, C74:044902, 2006. [cited on page 42, 45, 47, 66]
- [104] F. Carminati and R. Brun. GEANT Detector Description and Simulation Tool, CERN Program Library Long Writeup W5013, 1993. <http://wwwasdoc.web.cern.ch/wwwasdoc/geant/geantall.html>. [cited on page 42]
- [105] S. A. Bass et al. Microscopic models for ultrarelativistic heavy ion collisions. *Prog. Part. Nucl. Phys.*, 41:255–369, 1998. [cited on page 45, 48, 66]
- [106] M. Bleicher et al. Relativistic hadron-hadron collisions in the ultrarelativistic quantum molecular dynamics model. *J.Phys.*, G25:1859–1896, 1999. [cited on page 45, 48, 66]
- [107] Pythia website. <http://home.thep.lu.se/~torbjorn/Pythia.html>. [cited on page 66]
- [108] C.-Y. Wong. Signature of the Fragmentation of a Color Flux Tube. *Phys. Rev.*, D92:074007, 2015. [cited on page 75, 76, 89]
- [109] C.-Y. Wong. *Introduction to High-Energy Heavy-Ion Collisions*, chapter 7, pages 107–131. WORLD SCIENTIFIC, 2011. [cited on page 75, 89]
- [110] C.-Y. Wong, private communication. [cited on page 76]
- [111] S. Puławski, private communication. [cited on page 78]
- [112] Particle Population Matrix definitions, <https://edms.cern.ch/document/1700774/1>. [cited on page 123]

Appendices

Appendix A

Correlation measures

In Sec. 2 many two-particle correlation results from various experiments are presented. The analyses differ in correlation measures definitions. In this Appendix all of the measures presented in this thesis are described. They are ordered here by the experiments which use them.

The early analyses of two-particle correlations, which were done firstly in (pseudo)rapidity and azimuthal angle separately, based on the formula proposed by Wilson [49]:

$$g(y_1, y_2) = \frac{d^2\sigma}{dy_1^c dy_2^d} - \frac{1}{\sigma_T} \frac{d\sigma}{dy_1^c} \frac{d\sigma}{dy_2^d}. \quad (\text{A.1})$$

The correlation function $g(y_1, y_2)$ is calculated as the difference between the coincidence of particles c and d with their rapidities y_1 and y_2 (respectively), and the product of their counts at y_1 and y_2 divided by the total cross-section σ_T . This formula was used in Ref. [50].

The experiment at **ISR** [59], from which the results were shown in Fig. 2.3, modified the Wilson's formula for the purpose of the analysis in separate multiplicity bins. The two-particle correlation function in pseudorapidity is defined as:

$$C_n^{II}(\eta_1, \eta_2) = \rho_n^{II}(\eta_1, \eta_2) - \rho_n^I(\eta_1)\rho_n^I(\eta_2), \quad (\text{A.2})$$

where n is the multiplicity of charged particles, ρ_n^I is the charged particle density:

$$\rho_n^I(\eta) = \frac{1}{n\sigma_n} \frac{d\sigma_n}{d\eta}, \quad (\text{A.3})$$

ρ_n^{II} is the charged pair density:

$$\rho_n^{II}(\eta) = \frac{1}{n(n-1)\sigma_n} \frac{d^2\sigma_n}{d\eta_1 d\eta_2}, \quad (\text{A.4})$$

and $d\sigma_n/d\eta$ is the differential cross-section for producing a charged particle at rapidity η when n charged particles are produced within rapidity interval $|\eta| \leq \eta_{\max}$. The quantities should satisfy the normalization relations:

$$\begin{aligned} n\sigma_n &= \int_{-\eta_{\max}}^{+\eta_{\max}} \frac{d\sigma_n}{d\eta}, & \int_{-\eta_{\max}}^{+\eta_{\max}} \rho_n^I(\eta) d\eta &= 1, \\ \iint_{-\eta_{\max}}^{+\eta_{\max}} \rho_n^{II}(\eta_1, \eta_2) d\eta_1 d\eta_2 &= 1, & \iint_{-\eta_{\max}}^{+\eta_{\max}} C_n^{II}(\eta_1, \eta_2) d\eta_1 d\eta_2 &= 0. \end{aligned} \quad (\text{A.5})$$

The correlation function for two-particle correlations in azimuthal angle is constructed analogously to give:

$$C_n^{II}(\phi_1, \phi_2) = \rho_n^{II}(\phi_1, \phi_2) - \rho_n^I(\phi_1)\rho_n^I(\phi_2), \quad (\text{A.6})$$

where the density function in azimuthal angle is normalized in the region $0 \leq \phi_{1,2} \leq 2\pi$. The formulas A.2 and A.6 are used to construct two-dimensional two-particle correlation function in pseudorapidity and azimuthal angle:

$$C_n^{II}(\eta_1, \phi_1, \eta_2, \phi_2) = \rho_n^{II}(\eta_1, \phi_1, \eta_2, \phi_2) - \rho_n^I(\eta_1, \phi_1)\rho_n^I(\eta_2, \phi_2). \quad (\text{A.7})$$

Since the analysis was concentrated only on calculation of $C^{II}(\eta_1 - \eta_2) \equiv C^{II}(\Delta\eta)$ and $C^{II}(\phi_1 - \phi_2) \equiv C^{II}(\Delta\phi)$, the formulas A.2, A.6, and A.7 were transformed respectively to:

$$C^{II}(\Delta\eta) = \langle (n-1) \cdot C_n^{II}(\eta_1, \eta_2) \rangle, \quad C^{II}(\Delta\phi) = \langle (n-1) \cdot C_n^{II}(\phi_1, \phi_2) \rangle, \quad (\text{A.8})$$

and finally:

$$C^{II}(\Delta\eta, \Delta\phi) = \langle (n-1) \cdot C_n^{II}(\eta_1, \phi_1, \eta_2, \phi_2) \rangle. \quad (\text{A.9})$$

The **ACM Collaboration** results [60] presented in Fig. 2.4 were calculated using $\langle J_n \cdot C_n(\Delta y, \Delta\phi) \rangle$. Semi-inclusive rapidity or azimuthal angle correlation function is defined as:

$$C_n(1, 2) = \frac{\rho_n(1, 2)}{n(n-1)} - \frac{\rho_n(1)}{n} \frac{\rho_n(2)}{n}, \quad (\text{A.10})$$

where 1 and 2 are the values of rapidity or azimuthal angle of the first and the second particle (note, that the function above is one-dimensional). Single and two-particle rapidity densities are defined as:

$$\rho_n(y) = \frac{1}{\sigma_n} \frac{d\sigma_n}{dy}, \quad \rho_n(y_1, y_2) = \frac{1}{\sigma_n} \frac{d\sigma_n}{dy_1 dy_2}, \quad (\text{A.11})$$

where σ_n is the cross-section for the production of n charged particles. For the azimuthal angles the formulas are analogical. After choosing accepted particles (within selected rapidity range) the formula A.10 becomes $C_n(1, 2) \equiv C_n(y_1 - y_2) \equiv C_n(\Delta y)$. Since $C_n(\Delta y)$ was found to be symmetric around $y = 0$, the final $C_n(\Delta y)$ was shown as the average of the $\pm\Delta y$ data. Finally, in order to combine $C_n(\Delta y)$ functions for different multiplicities, $J_n \cdot C_n(\Delta y)$ is calculated, where $J_n = (m-1)$ for negative pairs, $J_n = (p-1)$ for positive pairs, and $J_n = (n-1)$ is for charge independent, and unlike-sign pairs. Since the analysis showed no dependence on n , the final correlation function was averaged over n :

$$\langle J_n \cdot C_n(\Delta y) \rangle = \frac{\sum J_n \cdot C_n(\Delta y) \sigma_n}{\sum \sigma_n}. \quad (\text{A.12})$$

The joint correlation function for rapidity and azimuthal angle is then defined as:

$$\langle J_n \cdot C_n(\Delta y, \Delta\phi) \rangle = \frac{\sum J_n \cdot C_n(\Delta y, \Delta\phi) \sigma_n}{\sum \sigma_n}, \quad (\text{A.13})$$

where:

$$C_n(\Delta y, \Delta\phi) = \frac{\rho_n(y_1\phi_1, y_2\phi_2)}{n(n-1)} - \frac{\rho_n(y_1\phi_1)}{n} \frac{\rho_n(y_2\phi_2)}{n}. \quad (\text{A.14})$$

The **STAR** experiment performed an analysis of two-particle correlations in p+p by using $\bar{N}(\hat{r}_{ij} - 1)$ measure [61]. To understand this measure, one needs to know that in this analysis, the single-particle momentum space was represented by (y_t, η, ϕ) space, where $y_t \equiv \ln(m_t + p_t)/m_\pi$ is transverse rapidity with assumption of pion mass for all particles and m_t is transverse mass. Thanks to this way of representation, the two-particle momentum space $\vec{p} \otimes \vec{p}$ can be decomposed into subspaces represented by Cartesian products of $y_t \otimes y_t$, $\eta \otimes \eta$ and $\phi \otimes \phi$. In particular, two-particle space of transverse rapidity $y_t \otimes y_t$ was used to isolate soft and hard components of the two-particle correlations which were separately studied in the analysis. For each of those components $\eta \otimes \eta$ and $\phi \otimes \phi$ subspaces were projected as so-called ‘‘autocorrelations’’: in case of $\eta \otimes \eta$ its ‘‘autocorrelation’’ was calculated as a difference $\eta_\Delta = \eta_1 - \eta_2$, while in case of $\phi \otimes \phi$ it was calculated as $\phi_\Delta = \phi_1 - \phi_2$. Finally, two-particle correlations in pseudorapidity and azimuthal angle were defined as a Cartesian product $\eta_\Delta \otimes \phi_\Delta$ or so-called ‘‘joint autocorrelation’’. The calculation was performed by obtaining bin-by-bin ratio $\hat{r}_{ij} = \hat{n}_{ij,sib}/\hat{n}_{ij,mix}$, where $\hat{n}_{ij,sib}$ and $\hat{n}_{ij,mix}$ are normalized numbers of pairs in a given bin. Coming back to the formula at the beginning, \hat{r}_{ij} is the ratio of normalized number of the sibling pairs (originating from the same event) to the mixed pairs (originating from events randomly filled with particles) and \bar{N} is the ensemble mean total multiplicity within detector acceptance.

The measure $\frac{\Delta\rho}{\sqrt{\rho_{ref}}}$ was used in STAR analysis of two-particle correlations in Au+Au interactions [63]. Before this measure is explained, it is worth to mention another one: $\frac{\Delta\rho}{\rho_{ref}} \equiv \frac{\rho_{sib} - \rho_{ref}}{\rho_{ref}}$ where ρ_{sib} is a density of sibling pairs (from the same event) and ρ_{ref} is a density of reference pairs (from mixed events). Then, $\frac{\Delta\rho}{\rho_{ref}}$ is a ratio relative to unity, which was called ‘‘per-pair’’ measure useful for quantum correlations. However, a measure better for initial-state scattering and hadronization would be ‘‘per-particle’’ measure:

$$\frac{\Delta\rho}{\sqrt{\rho_{ref}}} \equiv \sqrt{\rho'_{ref}} \frac{\Delta\rho}{\rho_{ref}}, \quad (\text{A.15})$$

which is an equivalent to Pearson’s normalized covariance. $\Delta\rho$ is the covariance of fluctuating particle numbers in two single-particle histogram bins, and $\sqrt{\rho'_{ref}}$ is approximately the geometric mean of two single-particle multiplicity variances giving the normalization.

PHOBOS in Ref. [66] used $R(\Delta\eta, \Delta\phi)$ variable:

$$R(\Delta\eta, \Delta\phi) = \left\langle (n-1) \left(\frac{\sigma^{\text{II}}(\Delta\eta, \Delta\phi)}{\sigma^{\text{mixed}}(\Delta\eta, \Delta\phi)} - 1 \right) \right\rangle = \frac{\langle (n-1)\sigma^{\text{II}}(\Delta\eta, \Delta\phi) \rangle}{\sigma^{\text{mixed}}(\Delta\eta, \Delta\phi)} - \langle n-1 \rangle, \quad (\text{A.16})$$

where $\sigma^{\text{II}}(\Delta\eta, \Delta\phi)$ and $\sigma^{\text{mixed}}(\Delta\eta, \Delta\phi)$ are foreground (same-event) pair distribution and mixed-event background distribution, respectively. Both are normalized to unit integral and defined for a given centrality bin. The mixed background is constructed by selecting two particles randomly from two different events with similar vertex position and centrality bin. Both variables are event-by-event evaluated. However, σ^{mixed} appeared to be multiplicity independent, thus the inclusive variable was used in calculations. $(n-1)$ is a weighting factor, where n is the total event multiplicity introduced to compensate dilution effects from uncorrelated particles. The total number of uncorrelated pairs increases quadratically with n while the total number of correlated pairs increases linearly. Hence, if heavy-ion collision is a superposition of separate nucleon-nucleon interactions, the same correlation function will be observed for both A+A and p+p collisions.

CMS in Ref. [80] constructed its correlation function by dividing the whole data sample into 10 bins of track multiplicity (each containing about 10% of all events taken to the analysis) and then the correlation function $R(\Delta\eta, \Delta\phi)$ was calculated as the weighted average. The function was defined as:

$$R(\Delta\eta, \Delta\phi) = \left\langle (\langle N \rangle - 1) \left(\frac{S_N(\Delta\eta, \Delta\phi)}{B_N(\Delta\eta, \Delta\phi)} - 1 \right) \right\rangle_{bins}, \quad (\text{A.17})$$

where S_N and B_N are the distributions of signal (same event pairs) and background (mixed events pairs), $\langle N \rangle$ is the number of tracks per event averaged over all events in a given multiplicity bin. Final $R(\Delta\eta, \Delta\phi)$ function is averaged over all multiplicity bins. The correlation function used by CMS is similar to Eq. A.16 used by PHOBOS with the difference that PHOBOS performed the analysis with averaging over centrality bins.

Later, CMS started to use per-trigger particle associated yield distributions as a correlation function. The analysis was done by combining trigger particles with associated ones, both laying in a particular range of transverse momentum. To construct a mixed background p_{trig} was paired with p_{assoc} particles originating from 10 different random events within the defined p_T range and the same reconstructed vertex range as well as the same track multiplicity class. The variable is defined as:

$$\frac{1}{N_{\text{trig}}} \frac{d^2 N^{\text{pair}}}{d\Delta\eta d\Delta\phi} = B(0, 0) \times \frac{S(\Delta\eta, \Delta\phi)}{B(\Delta\eta, \Delta\phi)}, \quad (\text{A.18})$$

where N^{pair} is the total number of correlated pairs, N_{trig} is the number of trigger particles in the event, and functions $S(\Delta\eta, \Delta\phi)$ and $B(\Delta\eta, \Delta\phi)$ are defined as:

$$S(\Delta\eta, \Delta\phi) = \frac{1}{N_{\text{trig}}} \frac{d^2 N^{\text{same}}}{d\Delta\eta d\Delta\phi}, \quad B(\Delta\eta, \Delta\phi) = \frac{1}{N_{\text{trig}}} \frac{d^2 N^{\text{mix}}}{d\Delta\eta d\Delta\phi}. \quad (\text{A.19})$$

Signal $S(\Delta\eta, \Delta\phi)$ is the per-trigger-particle yield of particle pairs from the same event, $B(\Delta\eta, \Delta\phi)$ is background distribution constructed by pairing trigger particles with associated particles from 10 different random events within the same 2 cm vertex position range. $B(0, 0)$ is the value of background function at $(\Delta\eta, \Delta\phi) = (0, 0)$ and serves as a normalization factor. The measure was used in analyses of two-particle correlations in Pb+Pb [68], p+Pb [72], and p+p collisions at $\sqrt{s} = 13$ TeV [82].

The **ATLAS** experiment, in studies of proton-proton collisions at $\sqrt{s} = 900$ GeV and 7 TeV [87], evaluated foreground $F(n_{ch}, \Delta\eta, \Delta\phi)$ and background $B(n_{ch}, \Delta\eta, \Delta\phi)$ correlation functions in events with a given multiplicity n_{ch} . After trivial calculations (see Ref. [87] for details) the final correlation function is defined as:

$$R(\Delta\eta, \Delta\phi) = \frac{\langle (n_{ch} - 1) F(n_{ch}, \Delta\eta, \Delta\phi) \rangle_{ch}}{B(\Delta\eta, \Delta\phi)} - \langle n_{ch} - 1 \rangle_{ch}, \quad (\text{A.20})$$

where $\langle \dots \rangle_{ch}$ is an average over all multiplicity bins. The formula is similar to that used by CMS (Eq. A.17) and PHOBOS (Eq. A.16).

In ATLAS results from p+p, p+Pb, and Pb+Pb collisions [69, 74, 88] the same $C(\Delta\eta, \Delta\phi)$ function, as in this thesis, was used (see Eq. 2.6). However, the difference is that ATLAS analyzed trigger-associated pairs of particles restricted in p_T . Depending on the analysis, various p_T ranges for trigger and associated particle were used.

ALICE also used $C(\Delta\eta, \Delta\phi)$ correlation function in the analysis of minimum bias p+p collisions¹[89]. The mixed background was constructed by taking particles from ten different events similar regarding to multiplicity and primary vertex location.

In correlations of Pb+Pb and p+Pb (Refs. [70] and [77], respectively) an associated yield per trigger particle distribution was used:

$$\frac{1}{N_{\text{trig}}} \frac{d^2 N^{\text{pair}}}{d\Delta\eta d\Delta\phi} = \frac{S(\Delta\eta, \Delta\phi)}{B(\Delta\eta, \Delta\phi)}, \quad (\text{A.21})$$

which is the definition similar to the one from CMS (Eq. A.18). However, the difference is in calculation of

$$S(\Delta\eta, \Delta\phi) = \frac{1}{N_{\text{trig}}} \frac{d^2 N_{\text{same}}}{d\Delta\eta d\Delta\phi}. \quad (\text{A.22})$$

The sums over the events for N_{trig} and $d^2 N_{\text{same}}$ are calculated separately before calculating ratio, while in CMS the ratio is calculated firstly and then averaged. The background $B(\Delta\eta, \Delta\phi)$ is constructed by correlating trigger-associated pairs of particles in the same event class² and within the same 2 cm interval of the main vertex position.

¹Actually, I took the idea of calculation of NA61 two-particle correlation function from the author of those analyses.

²There are four event classes defined in the ALICE experiment. They depend on centrality determined by total charge deposited in the ALICE VZERO detector: “60-100%”, “40-60%”, “20-40%”, and “0-20%”.

Appendix B

Particle Population Matrix

Particle Population Matrix (PPM) was prepared to apply the NA61 detector acceptance to 4π results produced by Monte Carlo generators. PPM is a three-dimensional matrix of phase-space coordinates (p, p_T, ϕ) . It is populated by the accepted particles produced in real events. The total momentum (p), transverse momentum (p_T), and azimuthal angle (ϕ) of each accepted particle are calculated to define a point in PPM 3D space. Then, when Monte Carlo events are analyzed, the PPM cut is applied on 4π results to reject generated particles which phase-space coordinates are outside of populated space of PPM points.

Such matrix is created for positively and negatively charged particles separately as well as for each analyzed energy. The examples of Particle Population Matrices are presented in Fig. B.1. The definitions of PPM for both charges and all SPS beam momenta are available in the CERN Document Server (see Ref. [112]).

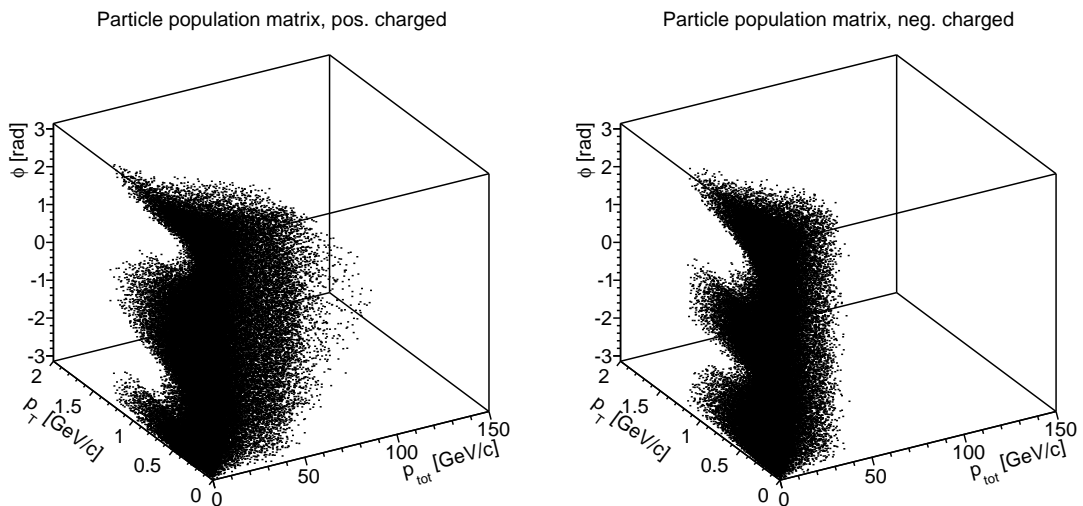


Figure B.1: Particle Population Matrix for inelastic p+p collisions at 158 GeV/c for positively (left panel) and negatively (right panel) charged particles.

Appendix C

Examples of distribution shapes

In this Appendix the examples of signal $S(\Delta\eta, \Delta\phi)$ and background $B(\Delta\eta, \Delta\phi)$ shapes are presented together with their corresponding correlation functions $C(\Delta\eta, \Delta\phi)$. The examples are shown for the EPOS data with two acceptances: almost all charged particles used (full range of pseudorapidity and azimuthal angle but $p_T < 1.5$ GeV/c) and particles within the NA61/SHINE acceptance being a result of application of Particle Population Matrix (see Appendix B for details). The distributions of the number of pairs show specific shapes (best seen for mixed events in Fig. C.1, top middle plot) originating from superpositions of two single-particle distributions (azimuthal angle and pseudorapidity). This trivial effect is eliminated by introducing the definition of the correlation function $C(\Delta\eta, \Delta\phi)$, where the signal distribution is divided by the corresponding background constructed from mixed events.

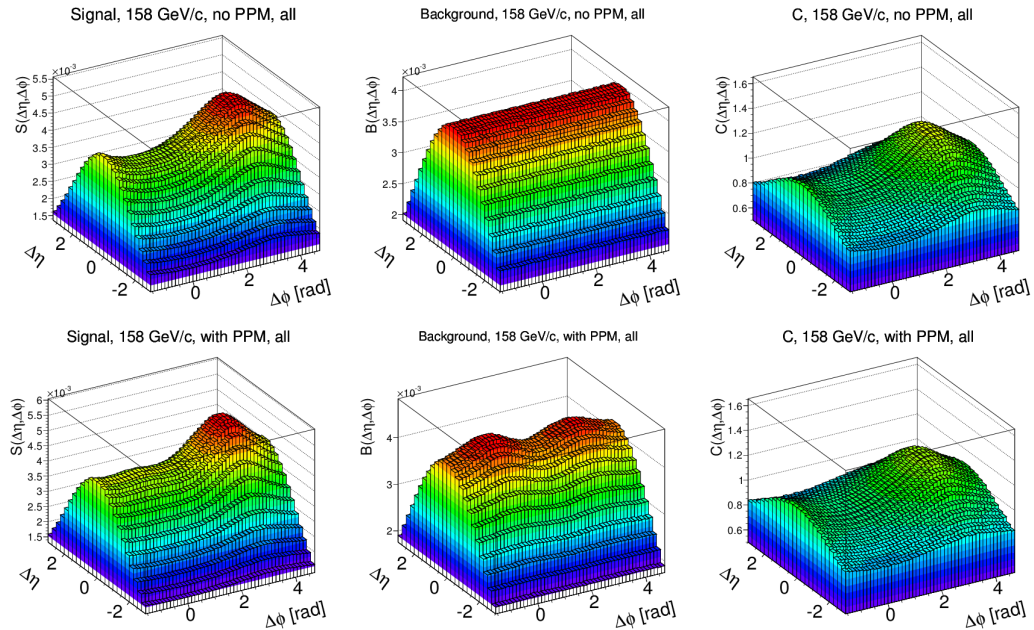


Figure C.1: Signal $S(\Delta\eta, \Delta\phi)$, mixed background $B(\Delta\eta, \Delta\phi)$, and correlation function $C(\Delta\eta, \Delta\phi)$ obtained from EPOS p+p collisions at 158 GeV/c without NA61/SHINE acceptance restrictions but with $p_T < 1.5$ GeV/c (upper panel) and with application of NA61/SHINE Particle Population Matrix (lower panel).

